DOI:10.15774/PPKE.ITK.2020.006

Changes in Ultrasound Signals and Transducer Impedance for Imaging and Characterization

Gergely Csány

Supervisor: Dr. Miklós Gyöngy

Pázmány Péter Catholic University

Faculty of Information Technology and Bionics

Roska Tamás Doctoral School of Sciences and Technology

A thesis submitted for the degree of *Doctor of Philosophy*

Budapest, 2019

DOI:10.15774/PPKE.ITK.2020.006

Abstract

Three main topics are presented in this thesis. A method is proposed for estimating the acoustic power output of ultrasound (US) transducers based on electrical impedance measurements of the transducer loaded by (N=3) various propagation media. The method being based on a two-port network model of the transducer was compared with acoustic measurements for high-intensity focused ultrasound (HIFU) transducers at center frequencies of 1.06, 3.19, 0.50, 1.70 MHz, consistently overestimating measured output with corresponding errors of 17.0, 4.5, 21.8, 7.8%. The results suggested a simple means of ensuring transducer acoustic output falls within specified safety limits.

A decorrelation ultrasound method is proposed for quantitatively characterizing dynamic changes on an ultrasound image sequence, based on the temporal decorrelation of signals coming from certain spatial locations. The method was tested on post-mortem tissue effects of mice. Quantitative results of dynamics characterization were in accordance with qualitative observations of the biological phenomena both in short- ($\sim$100 s) and long-term ($\sim$5000 s).

A real-time data-based scanning method is proposed for position estimation (PE) of ultrasound A-lines obtained via sensorless freehand scanning. Simulations and experiments showed the PE calibration curve to be robust enough for different scatterer concentrations, signal-to-noise ratios, and being predictable from a small number (31) of point scatterers, with $\sim 10^{-3}$ mean absolute errors. Use of a fixed versus an adaptive calibration curve gave similar PE accuracies with optimal performance for 150–350 μm scanning step sizes, and a 350-fold improvement in computation time. Clinical images of skin lesions demonstrated the feasibility of the algorithm for real, non-homogeneous tissue. Application of the scanning method led to the creation of a portable and cost-effective skin examination US device, providing solutions for challenges in screening and treatment planning of skin cancer.

DOI:10.15774/PPKE.ITK.2020.006

Declaration of original work used

Chapters 2–5 present the scientific work of the author published recently in peer-reviewed journals or in conference proceedings as follows. Chapter 2 is based on [1]. Chapter 3 is based on [2]. Chapter 4 is based on [3] and [4]. Chapter 5 is based on [5].

DOI:10.15774/PPKE.ITK.2020.006

Contents

DOI:10.15774/PPKE.ITK.2020.006

DOI:10.15774/PPKE.ITK.2020.006

DOI:10.15774/PPKE.ITK.2020.006

DOI:10.15774/PPKE.ITK.2020.006

List of Figures

DOI:10.15774/PPKE.ITK.2020.006

DOI:10.15774/PPKE.ITK.2020.006

DOI:10.15774/PPKE.ITK.2020.006

List of Tables

DOI:10.15774/PPKE.ITK.2020.006

List of Symbols

A	amplitude
A_T	area (of transducer active element surface)
a	air (material symbol)
α	acceptance criterion (rt-DABAS)
c	speed of sound
D	aperture of ultrasound transducer
d	distance
Δ	difference
Δy	image grid step size
e_b	bias error
e_r	ripple error
ϵ	threshold for acceptance criterion (rt-DABAS)
F	focal length
F_i	incoming data frames (DABAS)
$F[\,]$	Fourier transform
f	frequency
$f(t)$	temporal function
$f'(t)$	time derivative of f(t)
G_{focal}	focal gain
g	glycerine (material symbol)
H_r	focal plane beam pattern (hydrophone measurement)
h	hydrophone spatiotemporal response

DOI:10.15774/PPKE.ITK.2020.006

I	electric current
I_k	image frame (DABAS)
J	window size (rt-DABAS)
λ	wavelength
M_h	hydrophone sensitivity
m	material (general material symbol)
N	number of samples
N_d	near-field distance
n	number of samples (data points) in a signal or number of frames in an image
P	power
P_a	acoustic output power
P_{deg}	power required to raise the temperature of tissue by 1 °C
P_t	total power consumption
p	pressure
p_r	peak rarefaction pressure
ρ_0	density of a medium
$\rho(d)$	calibration curve
ρ_{xy}	Pearson correlation coefficient
σ	signal-to-noise ratio
T_{surf}	transducer surface temperature
t	time
τ	time constant (of an exponential function)
V	voltage
V_{rms}	root mean squared voltage
v	velocity (scanning speed)
w	water (material symbol)
$w(j)$	weights (rt-DABAS)
$\mathbf{x}$	vector of impedance parameters used in linear system of equations for two-port model parameter estimation

DOI:10.15774/PPKE.ITK.2020.006

$\overline{y}$	positions
$\overline{y}_d$	desired positions
$\overline{y}_t$	true positions
Z	electrical impedance
Z_0	characteristic acoustic impedance of a medium
Z_L	characteristic acoustic impedance of a load medium
z	axial distance from ultrasound transducer surface

DOI:10.15774/PPKE.ITK.2020.006

List of Abbreviations

1-D: One-dimensional

2-D: Two-dimensional

3-D: Three-dimensional

A-line: Amplitude-line

A/D: Analogue-to-digital

ABCD: Asymmetry, Border irregularity, Color variegation, Diameter $>$ 6 mm

ABCDE: ABCD, Evolving

ATP: Adenosine triphosphate

B-mode: Brightness-mode

BCC: Basal cell carcinoma

CLSM: Confocal laser scanning microscopy

CMUT: Capacitive micromachined ultrasonic transducers

DABAS: Data-based scanning

DECUS: Decorrelation ultrasound

DOF: Depth of field

ESWL: Extracorporeal shock wave lithotripsy

FDS: Fully developed speckle

FNAC: Fine needle aspiration cytology

FWHM: Full width at half maximum

HIFU: High-intensity focused ultrasound

IEC: International Electrotechnical Commission

KLM model: Krimholtz-Leedom-Matthaei model

MI: Mechanical index

MRI: Magnetic resonance imaging

DOI:10.15774/PPKE.ITK.2020.006

mRNA: Messenger ribonucleic acid

NDT: Non-destructive testing

OCT: Optical coherence tomography

PLA: polylactic acid

PRF: Pulse repetition frequency

RF: Radiofrequency (RF signal: raw ultrasound signal)

RFB: Radiation force balance

RMS: root mean square

RMSE: root-mean-square-error

rt-DABAS: Real-time data-based scanning

SCC: Spinal cell carcinoma

SLNB: Sentinel lymph node biopsy

SNR: Signal to noise ratio

TGC: Time-gain compensation

TI: Thermal index

US: Ultrasound

USD: United States dollar

USI: Ultrasound imaging

UV: Ultraviolet

DOI:10.15774/PPKE.ITK.2020.006

Chapter 1

Introduction

1.1 Motivation and overview

It is impressive to realize the diversity of ultrasound waves themselves and of the application potentials of ultrasound technology, from imaging (lifeless materials [6] as well as living tissues [7]) to therapy [8], from simple distance measurements to velocimetry and elastography [9], from conventional ultrasound signal generation and recording to optoacoustic imaging [10], from low energy data transfer [11] to security applications [12], etc. It is also exciting to realize the trends towards making the ultrasound devices more and more portable (due to technological advances and creative ideas) [13] and user-friendly (with the aid of artificial intelligence and other increasingly sophisticated methods) [14]. Finally, it is interesting how simple ideas can lead to significantly beneficial results in this field if the necessary technological background is provided.

The work presented in this thesis focuses on small but forward slices of this exciting, diverse world. The focus is basically on changes in ultrasound signals. Changes are investigated in various ways, as described in Section 1.1.1 below. The motivation of this work was not only the beauty an excitement of research but also taking advantage of the findings for wide-spread point-of-care and cost-effective use and calibration of ultrasound devices.

DOI:10.15774/PPKE.ITK.2020.006

1.1.1 Summary

The thesis focuses on three topics related to ultrasound technology. Regarding ultrasound imaging, novel correlation methods – exploiting signal changes – are presented and discussed: one taking advantage of temporal (Chapter 3) and another of spatial information (Chapter 4), in sequences of ultrasound signals. Both methods lead to applications in diagnostic ultrasound imaging, primarily. In particular, a portable and cost-effective diagnostic ultrasound device specified for skin imaging is presented in Chapter 5, taking advantage of the spatial correlation method presented in Chapter 4.

An additional topic is the presentation and discussion of an impedance-measurements-based method – exploiting impedance changes – for ultrasound transducer characterization (Chapter 2), as a novel approach in this field. Since this topic is related to the technical background of the application of ultrasound, the topic precedes the thesis chapters discussing the novel correlation methods in imaging. Characterizing the acoustic output of ultrasound transducers in a fast, practicable and cost-effective manner can be of great advantage in several fields including diagnostic, therapeutic and non-medical applications of ultrasound technology. In particular, it is applicable for determining safety of the skin-diagnostic device presented in Chapter 5.

1.1.2 Overview of current thesis

Following this overview, Chapter 1 introduces both the physical background of ultrasound imaging and the diagnostic area of application – in particular dermatological ultrasound for skin cancer imaging – which is the practical motivation of the most prominent part of this work. Ultrasound imaging background is discussed in terms of ultrasound imaging physics and of systems for ultrasound imaging (see Section 1.2).

A separate section (Section 1.3) briefly introduces the bioeffects of ultrasound. This topic is of particular relevance to the results presented in Chapter 2. It is followed by another brief section presenting the mathematical basics of correlation calculation (Section 1.4) which will be used in Chapters 3 and 4.

As mentioned above, the primary motivation for the application of the proposed

DOI:10.15774/PPKE.ITK.2020.006

methods is skin cancer diagnosis. The introduction of skin cancer and remarks on the importance of its early detection is followed by a short review of approaches for skin cancer diagnosis (see Section 1.5). The relevance of ultrasound imaging is highlighted among the approaches.

In Chapter 2, acoustic output characterization of ultrasound transducers is discussed, presenting the theory and validation of a novel method based on impedance measurements.

As shown in the subsequent chapters, data correlation was investigated in two aspects: temporal correlation and spatial correlation, leading to two novel methods with different applications.

In the method discussed in Chapter 3, temporal correlation is used for detecting the extent of dynamic changes at certain spatial points (pixels) in a series of ultrasound images acquired at the same spatial location. The method is validated on the application of showing the dynamics of post-mortem tissue effects.

Spatial correlation was also used for distance estimation of 1-D ultrasound data leading to the application of freehand manual scan conversion (without using position sensors) in 2-D imaging. In Chapter 4, the theory behind the proposed real-time data-based scan conversion method is presented, followed by validation of the algorithm. The validation was performed on simulations and experiments using homogeneous agar-graphite phantoms. Application and clinical validation of the proposed data-based scan conversion method is presented in Chapter 5. Clinical experiments were performed using a custom device, which was built for cost-effective *in-vivo* human skin imaging for skin cancer diagnosis, utilizing the presented imaging method.

Chapter 6 summarizes the thesis points concluded from the work presented in the previous chapters (Chapters 2–5).

DOI:10.15774/PPKE.ITK.2020.006

1.2 Introduction to ultrasound imaging

1.2.1 Ultrasound imaging physics

Ultrasound

Ultrasound is widely used in clinical investigations nowadays (being used in around 20–25% of clinical imaging examinations [7]). It has several and diverse application fields including therapeutic applications, industrial ones (like non-destructive testing) and navigation. Hereinafter, the topics of this thesis focus on applications in imaging with clinical motivation, therefore the introductory sections are written accordingly.

Ultrasound imaging uses high frequency mechanical waves for localizing and characterizing objects or edges of objects from which these waves reflect, inside media in which the waves are able to propagate. By definition, ultrasound can be any mechanical wave with a frequency above 20 kHz [15]. However, for imaging, significantly higher frequencies are tipically used ($\sim$MHz range for acceptable resolution in medical imaging) [16, 9].

There are several types of sound waves (propagating mechanical vibrations) being suitable for different applications (eg. shear waves, longitudinal waves, surface waves, Lamb waves) [17]. In the methods discussed in this thesis, hereinafter, the sound waves being applied are *longitudinal* ultrasound waves.

Ultrasound transducers

Mechanical waves can be generated and measured by using some type of *transducer*: a device that converts variations in a physical quantity (such as pressure in the case of longitudinal ultrasound waves) into an electrical signal, or vice versa [17]. An ultrasound transducer can convert an electrical signal into a pressure wave generated via mechanical vibrations. The same transducer is capable of measuring pressure variations induced by incoming ultrasound waves, via mechanical vibrations, and converting them into electrical signals.

DOI:10.15774/PPKE.ITK.2020.006

Pulse-echo method

Ultrasound technology is widely used for a variety of applications utilizing different properties and features of these mechanical waves. For ultrasound imaging, the most commonly used technique is the *pulse-echo* method.

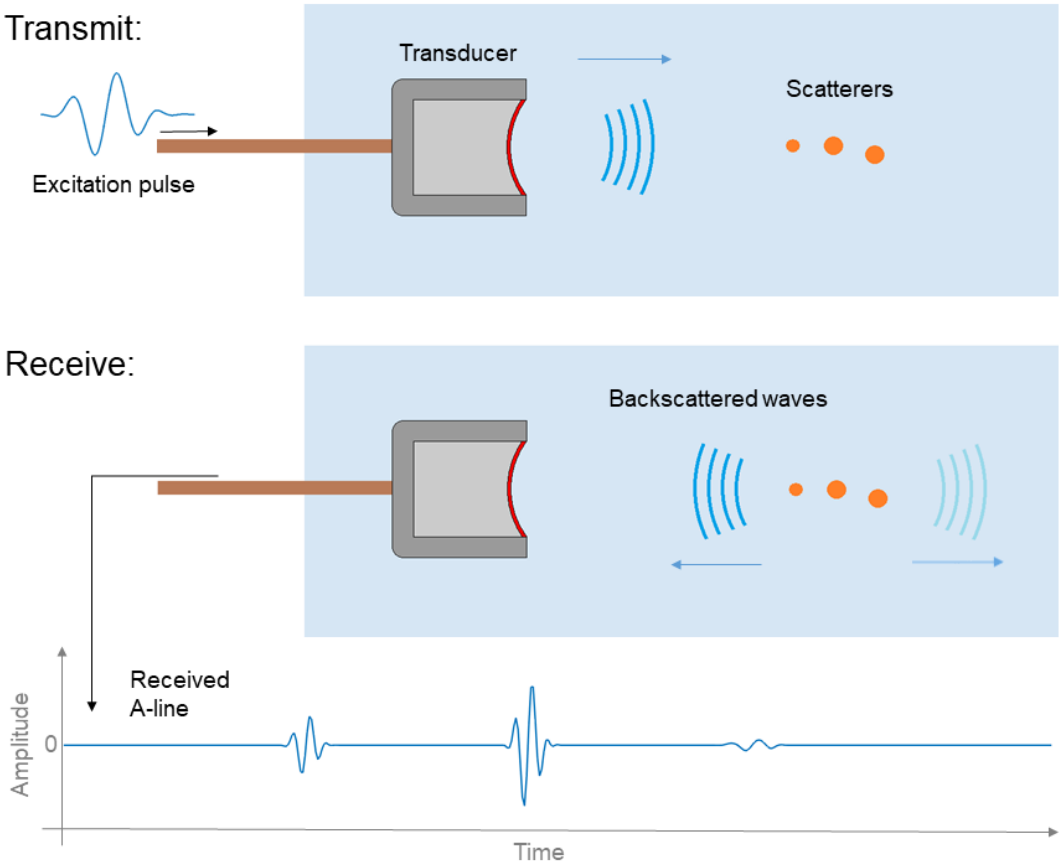

Figure 1.1: Schematic of the pulse-echo method. In transmit, the transducer converts the excitation pulse into mechanical wave packet which propagates in the direction designated by the transducer. The wave packet gets scattered on inhomogeneities of the propagation media. The backscattered waves are converted into a temporal electrical signal ('A-line') by the receiving transducer.

In *pulse-echo* mode, a longitudinal ultrasound pressure wave packet (pulse) is sent from a transducer (this step is called the *transmit*). As the wave packet propagates through the media of examination, it gets scattered on inhomogeneities of the media (Fig. 1.1). Ultrasound *scatterers* – the above-mentioned inhomogeneities

DOI:10.15774/PPKE.ITK.2020.006

– present as variations in density and compressibility [7, 9, 15]. The term *backscattered wave* stands for scattered wave packets that propagate towards the receiving transducer (being equal to the transmit transducer, in the case where the term "backscattering" is used) [7, 16]. During the step of *receive*, backscattered wave packets (echoes, in response to the transmitted pulse) are received by the receiving transducer (being usually identical to the transmitting transducer) which converts the pressure variations of the incoming wave packets into a temporal electrical signal (as noticed above) [17]. Basically, two quantities are being measured together in pulse-echo receive: amplitude of the received signal and time of signal arrival in reference to the time of transmit. In this way, the receiving transducer collects information about scatterers with different scattering strength (occurring in amplitude measurements of scattered waves) in a certain direction – along a 1-D line (Fig. 1.1). Such information of temporal amplitude changes (in a 1-D electrical signal, referring to pressure amplitude changes induced by 3-D backscattered wave packets reaching the receiving transducer surface) is called an *A-line* (or A-scan) [9].

Assuming that the propagation speed of ultrasound is known in the media of examination, a temporal signal (in t) can be converted into a spatial signal (in z), using the equation:

$$z = ct/2, \tag{1.1}$$

where c is the assumed propagation speed of sound in the medium of examination. The division by 2 takes into account that the wave packet traveled forth and back during the time measured between transmit and receive [9].

Pulse-echo data processing

Applying the technique of envelope detection on the biphasic raw A-line signals results in a monophasic 1-D signal which represents scatterers (with their scattering strength) and their spatial positions, along the line. Scattering strength can be deduced from the relevant peak amplitude (of a backscattered wave packet) occurring in the A-line, while taking into account the attenuation of the media in which the sound waves propagated forth and back, the acoustical shading effect (coming from the fact that scattering commutatively degrades the amplitude of the wave passing

DOI:10.15774/PPKE.ITK.2020.006

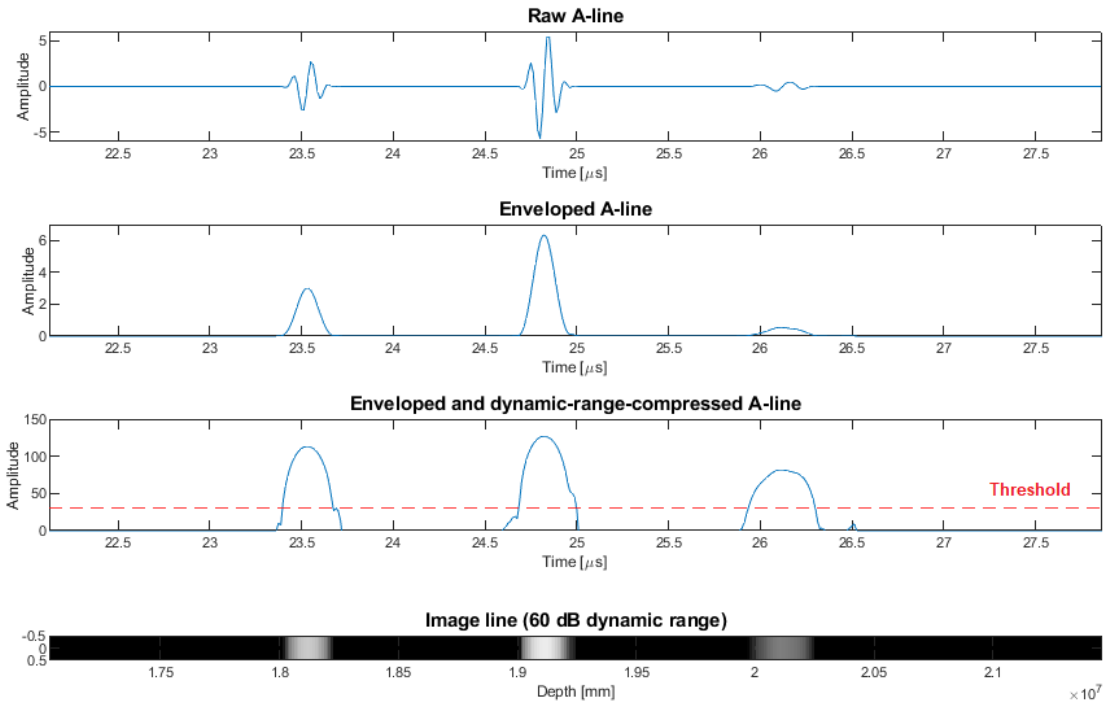

Figure 1.2: Basic steps of signal processing for ultrasound A-lines (presented for the example shown in Fig. 1.1). Raw biphasic A-line signal; Enveloped A-line; dynamic-range-compressed A-line with threshold for noise rejection in display; B-mode display of A-line.

on) and some interference of the backscattered waves and their harmonics [18].

The enveloped A-line signals can easily be represented and displayed as a 1-D series of image pixels in which color (or intensity in the case of a gray-scale representation) of a pixel corresponds to the enveloped amplitude of the backscattered signal (and thus to the strength of scattering in that certain point in space, which point is calculated from time and sound speed due to Eq. (1.1)). Such representation is the basis of the so-called *B-mode* (or brightness-mode) ultrasound images (Fig. 1.2).

For better interpretability of the received signals of varying amplitude peaks – for displaying a wider range of information – A-lines are usually displayed after applying *dynamic range compression* (usually done via logarithmic amplification) [9]. A *threshold* for data display is also usually applied for rejecting noise (Fig. 1.2).

DOI:10.15774/PPKE.ITK.2020.006

Scanning

In order to get a 2-D image, several A-line envelopes (in pixel series representation) should be put beside each other considering their relative spatial dispositions. 3-D images are usually created in a similar way from 2-D images (in this case, 2-D images are the blocks being put side by side with proper spatial positioning) [19].

As discussed above, ultrasound images generated using the pulse-echo technique are generally obtained from 1-D lines of ultrasonic signals. 2-D or 3-D ultrasound imaging requires a sequence of lower dimensional data with known relative positions to be geometrically placed alongside each other. This process is termed *scan conversion* [9]. Scan conversion is performed on data acquired in multiple spatial directions (one being the direction of the pulse-echo measurement and at least one distinct spatial direction), during the process of *scanning*.

Regarding ultrasound scanning, three directions are discerned: axial, lateral and elevational. *Axial* direction is the term for the primary direction in which the pulse and echoes propagate. *Lateral* direction is perpendicular to the axial direction and is usually the direction in which scanning is performed for obtaining a 2-D image. *Elevational* direction is perpendicular to both of the former ones, usually indicating the dimension pointing out from a 2-D image plane.

Physical characteristics of an ultrasound beam for imaging

Following a short introduction of the concept of ultrasound beams, the most important parameters and phenomena are shortly discussed here in relation to ultrasound imaging, such as resolution (in different directions), causes of attenuation, sound speed, acoustic impedance and pulse repetition frequency.

Spatial resolution of an ultrasound image as well as *penetration* for imaging is defined by the characteristics of the ultrasound beams formed and measured in the pulse-echo method. Theoretically two *beams* – transmit beam and receive beam – can be considered [9]. The transmit beam implies the changes introduced by the transmitted pulse into the pressure field in front of the transducer. The receive beam is (not a physical beam, but) a concept describing the parts of the pressure field which contribute to the signals being able to be received by the receiving

DOI:10.15774/PPKE.ITK.2020.006

transducer. For a single-element transducer (or for an array transducer not using dynamic focusing, nor dynamic apodization) that is being applied for both transmit and receive, the two beams can be treated as being identical. (The above-mentioned *dynamic focusing* and *dynamic apodization* are methods being used for changing the receive beam characteristics dynamically. Since these methods are applicable for multi-element – array – transducers only, these topics are out from the scope of this thesis.)

Spatial resolution of ultrasound images is specified by the length of the transmitted wave packet (axial resolution), by the focusing characteristics of the beam (lateral and elevational resolution) and by attenuation characteristics of the media of examination (since attenuation modifies the frequency band of the propagating wave, and in this way, it also modifies the resolution in all three directions [9]). *Wave packet length* is a function of the *frequency band* of the transmitted pulse and of the *sound propagation speed* inside the media of examination. For a certain sound speed, the greater the central frequency or the narrower the frequency band is, the better the resolution. However, ***penetration depth*** follows the opposite trend, due to the nature of *Rayleigh scattering* (higher frequency waves – with shorter wavelengths (close to the order of scatterer dimensions) – are being strongly scattered, thus the lower the frequency, waves – having a longer wavelength – penetrate deeper) [17]. In this way, acoustic attenuation acts like a low-pass filter on the sound waves.

Attenuation of ultrasound waves can be caused by different physical phenomena: *scattering* (as described above), *diffraction* and *absorption* (kinetic energy of the wave transforming into thermal energy of the propagation media) [18]. *Reflection* is a special case of scattering: causing scattered waves propagating back in the direction which they came from.

Propagation speed of sound (or sound velocity) is determined by the *density* and the *elastic modulus* (related to compressibility) of the medium. Although, to be accurate, *group speed* and *phase speed* of sound waves should be treated separately, it is commonly adopted in medical ultrasonic applications to describe sound speed with a single, amplitude-independent value that can be measured for any specific medium, since velocity dispersion does not appear to be significant in the frequency ranges and

DOI:10.15774/PPKE.ITK.2020.006

precision of these applications [7]. As already mentioned, sound speed is material-specific (tissue-specific, accordingly), and it is also affected by temperature, state (solid/liquid/gas) and pressure of the material [7]. These conditions of the media of interest therefore have to be taken into account when performing the conversion from time to distance on pulse-echo image data.

It is important to introduce the concept of the ***acoustic impedance***, as a useful descriptive of media with different acoustical properties. The acoustic impedance relates *pressure* and *particle velocity*. For locally plane waves (in inviscid medium), the *characteristic acoustic impedance* Z_0 is specified by the *density* of the medium (ρ_0) and the *sound speed* in it (c_0): $Z = Z_0 = \rho_0 c_0$ [17, 7]. The characteristic acoustic impedance of different media are very useful descriptors when considering propagation of sound waves in different media. The higher the difference in this impedance value is for two media, the stronger the reflection is from the boundary between them. It also follows that wave propagation in media with equal characteristic acoustic impedance suffers no reflection at all. It is easy to see that knowledge of characteristic acoustic impedances is very useful when describing or predicting wave propagation through different media. (These values and their differences should be considered in particular when imaging biological tissue.) Acoustic impedance is usually expressed in units of Rayleighs (Rayl; $1 Rayl = 1 Pa \cdot s/m$) [17]. Regarding fluids and solids used in ultrasound technology or examined in biological samples, typical values are in the range of $MRayl$ ($10^6 Rayl$). It is important to note here that soft tissues have similar characteristic acoustic impedances due to their high water content [9].

Focusing of ultrasound beams has already been mentioned above when discussing spatial resolution of ultrasound images. A *natural focus* arises for every ultrasound transducer, due to their finite aperture. The natural focus is determined by the *near-field distance* N_d of the transducer with a certain aperture D, transmitting or receiving waves of frequency f in a medium with sound speed c [18]:

$$N_d = \frac{D^2 f}{4c} = \frac{D^2}{4\lambda} \,. \tag{1.2}$$

There is a simple geometrical reason behind this, namely that spherical wavelets

DOI:10.15774/PPKE.ITK.2020.006

originating from different points of the aperture (and forming the wavefront) form an interference pattern of constructive and destructive interferences within the near-field distance [9]. However, there exists a distance from which the interference can only be constructive: this boundary is called the near-field distance, the value of which geometrically comes from the size of the transducer aperture (D) and from the wavelength (λ) as shown above. Since in the far field (in distances larger than the near-field distance) the pressure amplitude of the spreading wave degrades gradually, a natural focus occurs at the near-field distance of the transducer, being specific for the frequency of its waves.

There are further techniques for focusing an ultrasound beam, in a more plannable manner. Focusing can be achieved using specific *transducer geometry*, using *acoustic lenses* or by applying *relative phasing* in the case of array transducers [7, 9]. Transducers can be manufactured in a way to have a geometry which focuses the ultrasound beam emitted (and also focuses at the same region for receiving beams). In the cases of concave, spherically curved transducer geometries, focal length is defined by their radius of curvature. Acoustic lenses can be put in front of the transducer using a material in which sound speed differs from that of the loading medium (medium examined). Here, focusing characteristics can be designed by the shape of the lens and the ratio of lens and loading medium sound speed [7]. In the cases of array transducers, with the ability of beamforming by relative phasing of elements of the array, focusing can be achieved electronically, in a programmable way, with the great advantage of being able to change the focus between transmission and receive and even to change the focus dynamically (e.g. during receive).

Important measures of the focusing characteristics are the *focal gain* factor, *full width at half maximum*, *depth of field* and *focal length* of the sound beam [9]. *Focal length* (F) is defined by the distance of the focus from the surface of the transducer. *Focal gain* quantifies the pressure gain achieved at the focus in relation to the pressure amplitude at the transducer surface. In general, focal gain is defined by the aperture (D), area (A_T), focal length (F) of the transducer and by the wavelength (λ) of its wave [9]:

$$G_{focal} = \frac{DA_T}{\lambda F} \ . \tag{1.3}$$

DOI:10.15774/PPKE.ITK.2020.006

In the cases of unfocused transducers, $G_{focal} = 2$ gives a good estimate of the natural focus.

In order to characterize the focal region of the beam, beam diameter of at least -6 dB intensity of that of the peak is given by the *full width at half maximum (FWHM)* value. On the other hand, the focal zone in the axial direction is given by the *depth of field (DOF)* value which, in general, is also calculated for -6 dB of the peak intensity [9, 18].

In pulse-echo imaging, subsequent pulses are sent repetitively in order to acquire multiple data frames in time. This can be used either for acquiring data of temporal changes (at a constant spatial location) or for performing scanning (by physically moving the transducer and acquiring data in multiple dimensions). The parameter defining how often pulses are sent in an ultrasound transmit transducer is called the ***pulse repetition frequency (PRF)*** [9]. The frame rate of an ultrasound imaging system using a single-element transducer is equal to the PRF. For multi-element transducers, the frame rate is determined also by the number of image lines and – in some applications using multiple focal zones for each line – by the number of transmissions required for each line, together with the number of image lines [17]. In contemporary ultrasound imaging systems, a PRF in the order of hundreds of Hz or several kHz is applied usually.

1.2.2 Ultrasound imaging systems

The basic components of ultrasound imaging systems are shortly discussed hereinafter. An electrical signal is generated in the *waveform generator*, which signal drives the transmit transducer. The *transducer* converts the drive signal into mechanical vibrations due to the desired waveform. If the same transducer is used for transmit and receive, a *transmit / receive switch* (built into the path between the waveform generator and the transducer) accomplishes the task to switch for receiving and forwarding signals from the transducer to the signal processing network and to switch back for driving the transducer for a new pulse transmission – after a certain period of time determined by the PRF. The received signals – acoustic waves picked up and converted into an analogous electrical signal by the transducer – are digitized

DOI:10.15774/PPKE.ITK.2020.006

by an *analogue-to-digital (A/D) converter* for further signal processing. The basic steps of signal processing are *envelope detection*, *dynamic range compression* and *scan conversion (image formation)*, as described previously.

Regarding physical realization of systems for ultrasound imaging, hereinafter two topics – ultrasound transducers and scanning – are discussed as being important for the scope of the current thesis.

Ultrasound transducers

There are several physical phenomena which can be used for conversion between electrical and mechanical vibrations. Electromagnetic (cf. dynamic microphones), electrostatic (cf. condenser microphone, CMUT – capacitive micromachined ultrasonic transducers), magnetostrictive, electric spark (cf. ESWL – extracorporeal shock wave lithotripsy – transducers), radiant energy (cf. opto-acoustics) and piezoelectric effects are all transduction mechanisms which are proven to being applicable in ultrasound transducer technology [17]. Nevertheless, the most commonly used transduction mechanism of the above, currently, is the piezoelectric effect, being used for both transmission and receive [17].

The piezoelectric effect can manifest in crystals having crystal structure without central symmetry [17]. Mechanical strain applied on these crystals results in electrical polarization (due to the electrically asymmetric crystal structure) – this phenomenon is termed the *direct piezoelectric effect*. On the other hand, *inverse piezoelectric effect* also manifests in these crystals, meaning that applying voltage on (opposite) sides results in mechanical deformation of the crystal. The inverse piezoelectric effect is applied in transmit and the direct effect is applied in receive mode of piezoelectric ultrasound transducers.

In physical realization, a typical piezoelectric ultrasound transducer consists of the (relatively flat) piezoelectric crystal (also called the *active element*) with electrodes on both (front and back) sides connected to a connector (of some electrical connector standard), put inside an external housing encasing the *backing* material on one side (the back side) of the crystal [18] (Fig. 1.3). The material used as backing

DOI:10.15774/PPKE.ITK.2020.006

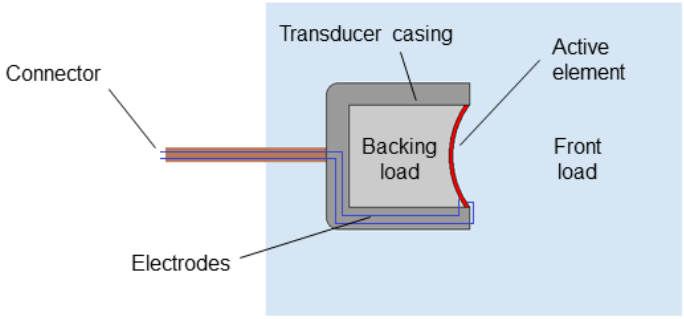

Figure 1.3: Schematic showing the main components of a piezoelectric (focused) transducer.

load is usually highly attenuative in order to absorb energy going into the backing direction and is chosen with respect of the intended use of the transducer. Pulse characteristics such as waveform duration and signal amplitude can be tuned via selection of the backing material regarding its characteristic acoustic impedance in relation to that of the crystal itself. With larger mismatch in characteristic acoustic impedances of the two materials, longer waveform is generated with higher signal amplitude (due to the stronger reflections from the crystal-backing interface) [18]. Choosing a backing load with a better match in acoustic impedance results in lower amplitude but more damped waves emitted into the material of interest, providing a better resolution for pulse-echo imaging. Choice of the former case (larger mismatch in acoustic impedance) is usually more appropriate when fabricating transducers for therapeutic applications while the latter case is beneficial for diagnostic ultrasound transducers. Central – resonance – frequency of the transducer is defined by the thickness of the piezoelectric crystal, while bandwidth of its pulse is defined by the backing material as described above. In order to reduce reflections from boundaries between the crystal and a medium with mismatching characteristic acoustic impedance, one or more *matching layer(s)* can be applied on the relevant surface of the crystal, consisting of a material with characteristic acoustic impedance value being in between those of the crystal and the medium. A commonly used arrangement is having a matching layer of thickness $\lambda/4$ on the front surface of the active element crystal (of length $\lambda/2$), in order to achieve a larger amplitude (and coherent) signal transmission into the front medium [18].

DOI:10.15774/PPKE.ITK.2020.006

Several *equivalent electric circuit models* exist for piezoelectric ultrasound transducers. A widely used and commonly accepted model is the so-called "KLM model" [20]. Electrical and mechanical parts of the circuit are being distinguished in this model. An *acoustic transmission line* with two ports accounts for the transducer converting electrical into mechanical energy on both front and back surfaces. A network of frequency-dependent components connects the acoustic transmission line to a third port accounting for connection with the electrodes. Equivalent circuit models are very useful for predicting or simulating the performance of transducers. Performance criteria – such as efficiency, dynamic range and pulse characteristics (bandwidth, pulse duration) – can be optimized by using these models. In the KLM model, the above characteristics can be simulated (and optimized) for physical properties of the transducer material (physical dimensions, acoustic impedance, sound velocity and coupling factor of the piezoelectric ceramic), of the possible matching layer(s) (physical dimensions, acoustic impedance), of the backing load and front load (acoustic impedance) and of the electrical tuning of the transducer [21]. Models like the KLM model have played an important role in designing piezoelectric ultrasound transducers and have also been further developed in order to become able to account for various real-life phenomena such as mechanical, dielectric and piezoelectric losses of energy [22].

Scanning

As introduced in Section 1.2, pulse-echo ultrasound images are technically built up from 1-D data lines. The process used for dimension incrementation is generally termed scanning. Currently used physical realizations of scanning can be summarized in the following groups [19]:

1) Electronic scanning,
2) Mechanical scanning,
3) Free-hand scanning with position sensors,
4) Free-hand scanning without position sensors.

Given the importance of this topic regarding the current thesis, the above approaches of scanning are discussed in a separate subsection, as follows.

DOI:10.15774/PPKE.ITK.2020.006

1.2.3 Scanning methods for ultrasound imaging

The following is a review of different, currently available scanning methods for ultrasound imaging. For further information, the reader is referred to [19, 4].

Electronic scanning

Image dimension can be incremented without any physical movement when using a multi-element transducer. In the case of a 'linear array transducer', multiple transducer elements are arranged along a line (Fig. 1.4). The beam of these multi-element transducers can be focused in several directions along a plane. In a similar way, the focus of the transducer can be varied by using different delay profiles (delay being a function of transducer element position) before signal summation in the receive mode. In this way, multiple axial scans (A-lines) can be collected in the lateral direction.

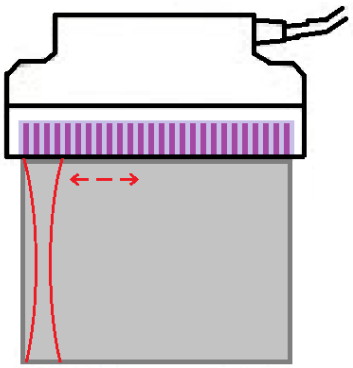

Figure 1.4: Schematic illustrating the concept of electronic scanning using a (multi-element) linear array transducer.

Considering the case of transducer elements being placed on a 2-D plane, 3-D images can be scanned electronically in a similar way (by varying the delay profile on the 2-D array of elements).

The great advantage of electronic scanning is that it is a real-time method for multidimensional scanning with precisely known information of the spacing of scans and without any physical movement needed. However, array transducers require

DOI:10.15774/PPKE.ITK.2020.006

complex electronics and multiple transducer elements, hence they are not cost-effective [19].

Mechanical scanning

A widely used approach for incrementing image dimension is to move the transducer physically in a direction in which dimension incrementation is desired. However, in order to avoid distortion, it is necessary to know the relative location and orientation of the single (lower-dimensional) scans. Mechanical scanning techniques use a motorized mechanical apparatus to physically move a transducer with precisely known location and orientation [19].

Linear mechanical scanners move the transducer along a line in order to acquire a series of parallel images. Besides its spatial precision, this method has the advantage of collecting images with equal spacing, thus a smooth resolution can be obtained. As a disadvantage, a mechanical scanner apparatus is a bulky device, hence it is not very convenient to use [19].

Another commonly used approach is to tilt the transducer (Fig. 1.5), obtaining fan-like images with equal angular spacing [19]. Tilt scanners are convenient to use and not bulky (as compared to the linear scanner devices), but have the disadvantage of uneven resolution in different depths [19].

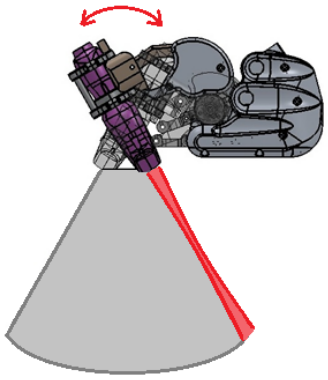

Figure 1.5: Schematic illustrating the concept of mechanical scanning using tilting motion of a single-element transducer.

A third possible technique is rotational scanning in the case of 3-D imaging.

DOI:10.15774/PPKE.ITK.2020.006

In this method, rotation is performed along the axial axis. Rotational scanning has similar advantages and disadvantages to tilt scanning, having the additional disadvantages of an even more complex resolution distribution and the risk of having artifacts based on possible physical displacement of the axis of rotation [19].

In summary, mechanical scanning has the advantage of precise position determination and fast reconstruction time [19], but also has the general disadvantages of potential failure of the motorized system and of physical limitations of the area (or volume) in which scanning can be performed.

Free-hand scanning with position sensors

In order to get rid of the above disadvantages and limitations, free-hand scanning can be used, providing more convenience and freedom. Determination of the relative locations and orientations of single scans is achieved in most of the cases by the usage of position sensors (Fig. 1.6). There are several types of sensors successfully combined with ultrasound transducers.

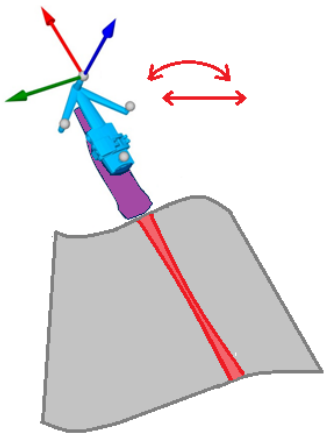

Figure 1.6: Schematic illustrating the concept of freehand scanning using a single-element transducer combined with some type of 3-D position sensor.

In the case of using acoustic sensors, (low-frequency ultra)sound is emitted from three separate locations on the transducer casing surface and measured by three microphones (located somewhere near the object of examination). One of the main limitations of this technique is that the line between the transducer and the micro-

DOI:10.15774/PPKE.ITK.2020.006

phones should be left free. The other disadvantage is that sound speed varies with humidity in the air [19].

Another approach uses articulated arms (conjoining the transducer with a fixed location). In this case, relative movements are measured by potentiometers located in the joints of the arms. As a limitation, larger flexibility of the arms leads to worse resolution of position sensing. However, by decreasing the length of the arms (in order to reduce flexibility) leads to another disadvantage: a reduced maximum size of scanning area or volume [19].

Probably the most successful position sensors for free-hand scanning are the magnetic sensors. These little sensors provide convenience and freedom. However, the magnetic field distortion of ferrous metals can cause artifacts when using these systems [19].

Free-hand scanning without position sensors

There is an interesting potential for position estimation even without additional sensors or external devices, taking advantage of the "speckle pattern" of ultrasound images (Fig. 1.7). *Speckles* are common features of ultrasound images. The speckle pattern evolves from interference caused by interaction of the ultrasound field and the scatterers [19]. Although they are commonly treated as artifact, speckle patterns may contain important information about the imaging system and the examined medium [23]. Data-based scan conversion makes use of the speckle pattern of ultrasound images. The idea is based on the correlation between two parallel images. If the images are close enough to each other, the speckle pattern causes a high correlation between them. When moving away from a certain line, the calculated correlation value is decreasing even in homogeneous media, again, due to the presence of the speckle pattern. There is a specific dependence between distance and correlation, which can be described by the so-called decorrelation function (in terms of distance).

A great advantage of these methods is that they can be applied on transducers without any hardware modifications [7]. Another important advantage is the lack

DOI:10.15774/PPKE.ITK.2020.006

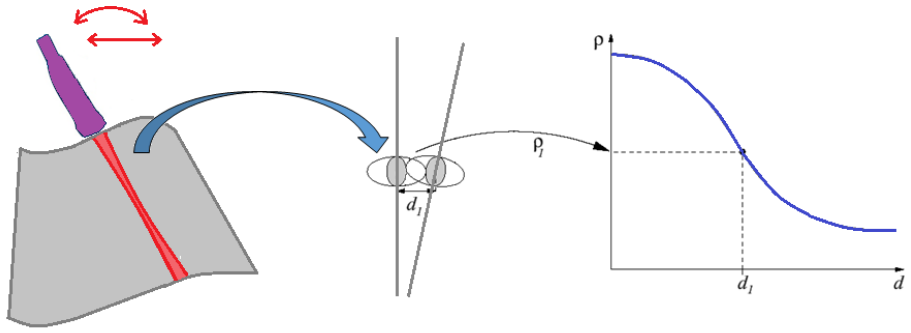

Figure 1.7: Schematic illustrating the concept of freehand scanning without position sensors. In data-based scanning approaches, the relative positions of the A-lines are estimated from speckle correlation ***(middle)****, knowing the distance-correlation dependency* ***(right)****.*

of spatial limitations for the area scanned, achieved without the disadvantages, cost and complexity of the above position sensors. On the other hand, calibration is necessary and reliability is usually not enough for distance-based measurements (in the scanning direction) on these images [19, 7].

1.2.4 Data-based scan conversion approaches

In order to perform scan conversion based on correlation, an accurate calibration curve should be obtained. The term *calibration curve* refers to a function, that describes a one-to-one relation between distance and correlation. Much research focuses on the proper determination of this function. Conventional methods use a nominal decorrelation curve obtained from an (ideal) fully developed speckle (FDS) [24]. The nominal decorrelation curve is stable for a certain transducer [25]. Furthermore, several adaptive algorithms exist [26] that use an ideal phantom for obtaining the nominal decorrelation curve and then use adaptive models to get dynamic decorrelation curves [27]. There are techniques for speckle tracking without FDS using modeling of the raw ultrasound signals generated by speckles [23]. Several studies perform statistics on the image data in order to get a more suitable calibration curve (based on some statistical features of the examined object and of the signals generated by the imaging system). It has been shown that estima-

DOI:10.15774/PPKE.ITK.2020.006

tion of the envelope statistics allows characterization of tissue regularity and thus estimation of the calibration curve [25].

1.3 Biological effects of ultrasound

As the main scope of this thesis is in medical ultrasound diagnostics and furthermore, since one of the novel methods presented and discussed here (in Chapter 2) points towards the application of determining safety parameters of ultrasound equipment in a new way with several advantages, biological effects of ultrasound and their measures are briefly introduced here.

Ultrasound imaging and therapy forms a type of radiation of mechanical wave beam into the media of examination, ie. tissue in the case of biological samples. Regarding safety, an outstanding biomedical advantage of ultrasound is the lack of ionizing effect of its radiation. For safe use of ultrasound, nevertheless, two aspects – namely the mechanical and thermal effects – should be kept within limits.

Mechanical effects arise from ultrasound waves introducing pressure variations in the tissue in which they propagate. *Thermal effects* arise from tissue absorbing some of the mechanical energy of the sound waves and also from the heat of transducer propagating from the transducer surface in tissue regions being near to it [28].

Standards of the International Electrotechnical Commission (IEC) define the *mechanical index (MI)* and *thermal index (TI)* values which should be verified for biomedical ultrasound systems to be within certain limits regarding the application. As mentioned above, an additional safety measure of transducer temperature rise should also be proved for claiming safety, especially for the cases of having temperature sensitive tissue within about 5 mm from the transducer surface [28].

1.3.1 Mechanical index

Ultrasound, as a pressure wave propagating through tissue, causes compression and rarefaction in successive cycles at specific locations of the tissue. If the peak rarefaction pressure is large enough, bubbles may come to be in the tissue (fluid) [7]. This effect is called *cavitation* and is very useful in several therapeutic applications of ul-

DOI:10.15774/PPKE.ITK.2020.006

trasound [29] but is to be avoided in numerous fields of the body including arteries (in which arising microbubbles would lead to serious consequences). Therefore, the MI of diagnostic ultrasound machines should be kept within safety limits in which cavitation is theoretically not possible to occur.

MI is defined by the peak rarefaction pressure (p_r) and the frequency (f) of the ultrasound wave as follows:

$$MI = \frac{p_{r,0.3}}{\sqrt{f}} \ . \tag{1.4}$$

The peak rarefaction pressure becomes the greatest in the focal region of the ultrasound beam. Due to the attenuation of tissue, pressure values "derated" from those measured in pure water are used for the calculations. Attenuation in soft tissue is usually in the range of 0.5–1 dB/MHz/cm. In safety standards, the absorption value of 0.3 dB/MHz/cm is commonly used (for derated pressure $p_{r,0.3}$) leading to a worst-case estimation for MI [28].

1.3.2 Thermal index

By calculating TI, the likely maximum temperature rise due to absorption can be estimated in the tissue [28]. TI is defined as the ratio of the acoustic output power (P_a) of the transducer and the power (P_{deg}) required to raise the temperature of the tissue by 1 °C [28]:

$$TI = \frac{P_a}{P_{deg}} \ . \tag{1.5}$$

Since the presence of bone has a significant influence on the ultrasound-based temperature rise of tissue, different formulae are defined in standards for calculating TI regarding the presence and relative position of bone in the ultrasound beam [28].

1.3.3 Transducer surface temperature

In addition to the thermal effect due to absorption of the sound waves, temperature rise of the transducer should also be considered in superficial tissue being close enough (within about 5 mm) to the transducer surface. Transducer temperature

DOI:10.15774/PPKE.ITK.2020.006

rise comes from electrical energy dissipation (of the transducer and of the processing electronics behind) [28]. Limits for transducer surface temperature T_{surf} are also defined in safety standards (for different load media).

The above safety indices used for quantifying the biological effects of ultrasound can be calculated based on pressure, power or intensity and temperature measurements. Pressure measurements are usually performed by using a hydrophone measurement system. Intensity can be calculated from pressure. Power measurements are usually done using a radiation force balance (RFB) or calculated from hydrophone measurements. Temperature can be measured using an infrared camera (in air) or thermocouples (placed in tissue) [28]. MI and TI values should be indicated to the user of any ultrasound device for which each of these values may exceed the value of 1. Limits for T_{surf} are 50 °C in air and 43 °C in tissue, according to international standards, which means that a 33 °C human skin is permitted to be heated up by about 10 °C [28].

1.4 The correlation coefficient

In a significant part of this thesis, novel methods utilizing (temporal or spatial) correlation of ultrasound imaging data are presented (as already introduced in Section 1.1.2). Therefore, a brief introduction of the mathematical basics of correlation calculation is presented here.

The *correlation coefficient* quantitatively describes a statistical relationship between two variables with a single number. The most commonly used measure of correlation is the *Pearson correlation coefficient* which measures the linear relationship between two variables regarding strength and direction of the relationship. The Pearson correlation coefficient is calculated for a pair of variables via dividing the covariance of the two variables by the product of their individual standard deviations. For paired data of samples x and y (of equal sample size n): $(x_1, y_1), (x_2, y_2), ..., (x_n, y_n)$, the Pearson correlation coefficient ρ_{xy} can be calculated

DOI:10.15774/PPKE.ITK.2020.006

from the formula:

$$\rho_{xy} = \frac{\sum_{i=1}^{n}(x_i - \overline{x})(y_i - \overline{y})}{\sqrt{\sum_{i=1}^{n}(x_i - \overline{x})^2}\sqrt{\sum_{i=1}^{n}(y_i - \overline{y})^2}} , \tag{1.6}$$

where $\overline{x}$ and $\overline{y}$ denote the mean of samples x and y, respectively, calculated as $\overline{x} = 1/n \sum_{i=1}^{n} x_i$.

1.5 A review of skin cancer diagnostics

1.5.1 Introduction

The motivation behind some of the research that have lead to the results presented in this thesis is an important disease to be treated, of a significant organ of the human body [30]. Skin cancer is one of the most frequent types of cancer in the developed world [31, 32, 33, 34]. *Melanoma malignum*, a type of skin cancer is responsible for the vast majority of all skin cancer deaths [35]. Fortunately, this type of lesion can be treated safely via surgical excision, but only in its early stage. Therefore, early and accurate melanoma diagnosis is a crucial problem to be solved in this area [35, 36]. Following an introduction to skin cancer facts, to the structure of the human skin and to some relevant skin cancer types, a review is presented here of relevant invasive and non-invasive diagnostic methods currently used or being under investigation. Potentials in ultrasound-based skin cancer diagnosis are presented in a separate section, showing the versatility of this non-invasive approach for examination purposes.

1.5.2 Background

Skin cancer is reported to be the most common type of cancer in the United Sates [31] and the third most frequent cancer in Hungary [32]. It is very frequent in many other countries as well (being especially frequent in the Scandinavian countries within Europe) and is extremely frequent in the population of Australia [33]. The lifetime risk for developing skin cancer is around 20% for an average American person [34]. These facts along with other statistical data represent the importance of dealing with these types of cancer.

DOI:10.15774/PPKE.ITK.2020.006

The most common skin cancer type is basal cell carcinoma (basalioma), which is a relatively benign cancer as it rarely metastasizes [37]. Melanoma malignum (a type of skin cancer) – the proportion of which is about 1% among all skin cancers [38] – accounts for the majority, 65% of all skin cancer related deaths [35]. As with malignant tumors in general, early detection and treatment of melanoma plays a crucial role in the prognosis and survival of the disease [35, 36]. Earlier detection and treatment (the primary treatment being surgical excision) leads to less morbidity and mortality and even to a decreased cost of therapy [35].

In summary, prevention, early detection (via appropriate diagnosis), adequate treatment and sufficient follow-up of skin cancer diseases is an important healthcare problem to be developed. As melanoma is extremely dangerous compared to most other skin cancer types of less morbidity and far less risk, differential diagnosis (aiming to recognize skin cancer type and to distinguish it from other types) plays a crucial role in skin cancer examination and treatment.

The following review gives insight into the skin diseases to differentiate in between and into the currently used methods for skin cancer diagnosis – as already mentioned above – highlighting the role of ultrasound-based diagnostics as a promising non-invasive approach to assist early detection of melanoma and other types of skin cancer.

1.5.3 Skin cancer

Structure of the human skin

The skin is the largest organ of the human body (weighting 15–20% of the full body mass) [39]. This organ separates and at the same time connects the body and its environment. One of the primary functions of the skin is protection of the body, including physical protection (against mechanical effects and UV radiation), chemical protection (against acids) and biological protection (contra viruses and bacteria). Further functions include homeostasis (thermoregulation, dehydration prevention), sensory role as a touch probe, secretion (of certain chemicals), nutrient storage and insulation (subcutaneous fat tissue) [39]. The skin is composed of three

DOI:10.15774/PPKE.ITK.2020.006

primary layers: *epidermis*, *dermis* and *subcutis*.

The *epidermis* is the uppermost layer of the skin, generally being less than 1 mm thick (75–600 μm, at most 1.4 mm [39]). This layer is composed of 5 sublayers. Cells created at the innermost layers move towards the outermost layer, going through processes of changing shape and composition (keratinization). It is important to note that there are no blood vessels in the epidermis. Several cell types (with different roles) are present in this layer – like keratinocytes, melanocytes, Langerhans cells, Merkel cells, and even lymphocytes.

Among the above cell types, melanocytes are specifically interesting regarding the motivation of melanoma detection. Melanocytes are pigment cells, producing melanosomes that contain melanin – a dye that can absorb UV (ultraviolet) light – and allocating them into neighbouring cells. The number of melanocytes (being around 1% of the total number of skin cells) is almost equal in people regardless of their skin color [40]. However, the amount of melanin (that is responsible for skin, hair and eye color) is greater for people being exposed to stronger UV radiation. UV radiation causes inflammation in skin being poor in melanin [30].

The (1–2 mm thick) *dermis* contains blood vessels, nerves, sweet glands and sebaceous glands. The dermis is rich in collagen fibers which provide elasticity to the skin [40].

The innermost skin layer is the *subcutis*. It is a loose, connective tissue containing fat storing lipocytes – fat tissue thickness depends on body region (ranging from 0 to 3 cm) [39, 40].

Skin lesions

There are many types of skin cancer and skin lesion. Here, only some of these types are presented below, namely those considered to be the most relevant to the current work.

Nevus *(or naevus)* is a benign skin lesion containing closely located damaged melanocytes which store melanin (up against healthy melanocytes which produce and then distribute melanin to other cells, and which are distributed relatively homogeneously and far away from each other) [30].

DOI:10.15774/PPKE.ITK.2020.006

Nevi can be congenital (presented since birth) or "collected" (which means that they have been developed after birth, at a certain moment in life). Nevi can be located in the junction between the epidermis and dermis (junctional nevus), inside the epidermis and dermis (compound nevus), or deeper in the skin (intradermal nevus).

A nevus may become malignant most probably due to excessive exposure to sunlight (UV radiation), or to physical injury of the nevus. If the nevus becomes changing (its shape, color or size), it can be suspicious of becoming malignant.

Melanoma *maligna* is the primary malignant skin cancer. Melanoma forms from melanocytes (that is why in many cases it transforms from a nevus – containing spacially concentrated melanocytes). Reasons behind the appearance of this skin disease can be genetical [41], hormonal, virus-induced [42], but in most of the cases it is caused by radiation (primarily UV light). UV radiation, in normal circumstances, is absorbed by melanocytes and enhances vitamin D production, however, excessive exposure to sunlight (or other forms of UV irradiation) damages DNA of the melanocytes themselves that can lead to the emergence of melanoma maligna that mainly occurs on the trunk and on extremities (being most exposed to sunlight) [30].

Melanoma typically grows in two phases. In the beginning, it grows (usually slowly and) horizontally. Then, in the second phase, it starts growing rapidly vertically [43]. Malignity means that it can form metastases in this vertical growing phase, when reaching blood vessels. The growing nature of melanoma clearly points out the importance of its early (first phase) diagnosis.

The primary treatment of melanoma is surgical excision currently (with minimal risk of recrudescence and maximal surveillance). Radiation therapy may also be applied in order to exterminate potential metastases.

Basalioma *(also called basal cell carcinoma, BCC)* is the most frequent, but less malignant skin cancer with a good prognosis and very low risk of forming metastases [37]. Its environmental causes are similar to those of melanoma, however, basalioma is formed from basal cells (in the basal layer of the skin), appears most often on the face and grows mostly horizontally (that is why metastases are very rare for this type of cancer). It is also primarily treated by surgical excision, with a

DOI:10.15774/PPKE.ITK.2020.006

very rare recrudescence.

Spinalioma *(squamous cell carcinoma, SCC)* occurs from keratinizing squamous cells, mostly in areas being injured or exposed to sunlight. This cancer type can form metastases more often than basalioma, however, it grows very slowly. Spinalioma is also treated surgically.

1.5.4 Skin cancer diagnosis

Prior to the 1980s, melanoma was recognized usually at advanced stages. Recognition was based on macroscopic features – like ulceration, fungation or nodular presentation [35]. These features are associated with rather advanced stage melanomas, thus, mortality of patients with these lesions was very high.

In 1985, some researchers devised and published a simple algorithm helping early recognition of signs of changing nevi being suspicious of becoming malignant [44]. The algorithm was named "*ABCD diagnosis*" being a well-recognizable, simple acronym of features to be monitored when performing examination of nevi. The aim was to educate both physicians and the public, assisting early recognition of malignant skin lesions. The acronym (masterly suggesting "as easy as the ABC") stands for **A**symmetry, **B**order irregularity, **C**olor variegation, **D**iameter greater than 6 mm. The "ABCD diagnosis" became widespread (even in laic self-examination) and its effectiveness and diagnostic accuracy have been verified by multiple studies [35]. The diagnostic criteria were applied with 57–90% sensitivity [45] and 59–90% specificity [46] ranges and with moderate but statistically significant interobserver concordance [47, 44]. Accounting for the important feature of lesion change for potential malignant lesions, "ABCD" was complemented by "E" standing for "**E**volving" [48]. Other early diagnosis criteria were also devised, like the "*Glasgow 7-point Checklist*" [49], however, these did not get as widely adopted as "ABCDE" – perhaps because of their greater complexity [35].

The appearance and spread of the above-mentioned diagnostic criteria significantly enhanced early melanoma detection, however, they did not fully solve the problem of making an accurate early diagnosis. In current clinical practice, the "final word" is given by histological examination of lesions – being the "gold stan-

DOI:10.15774/PPKE.ITK.2020.006

dard" for skin cancer diagnosis (reaching 100% sensitivity and specificity). Whereas histopathology is an invasive and time-consuming method, non-invasive, cost- and time-efficient examination methods also appeared in the field of skin cancer diagnostics to assist diagnosis and to make it more widely accessible.

Invasive methods for skin examination

Histology. As already mentioned, histology is the gold standard diagnostic method currently. With this method, samples from the lesion, got via biopsy, are examined on the cellular level. Results of the histological examination ascertain the diagnosis and specify the prognosis of the disease. Histology can be performed on small *ex-vivo* samples before decision of therapy. Histological examination is also performed on lesions excised after surgical treatment.

The great advantages of histology are its diagnostic accuracy and its ability to predict prognosis.

Disadvantages include that it is rather time-consuming (from days to weeks), requires professional competence, furthermore, it is invasive (and thus, involves the risk of infections) and the sampling method (biopsy) also requires competence.

Sentinel Lymph Node Biopsy (SLNB). SLNB is a useful method when looking for metastases. Lymph nodes to be examined can be found and easily excised after injection of radioactive substance or a dye into the body area of interest. The result of SLNB is an independent prognostic factor [50]. However, this method has the disadvantages of invasiveness and potential risk of complications of dye injection.

Fine Needle Aspiration Cytology (FNAC). FNAC is a rather safe, minor surgical procedure of tissue sampling for histological examination. However, it is still invasive and has the disadvantages of histological examinations.

Non-invasive methods for skin examination

As seen above, biopsy followed by histology is rather time-consuming and needs dedicated staff to perform it, furthermore, biopsy is an invasive intervention, bearing the risk of infections and complications. Non-invasive skin examination methods have the common goal of reducing the number of unnecessary biopsies, thus release

DOI:10.15774/PPKE.ITK.2020.006

capacity of histology labs while making patient treatment less noisome. Some of the non-invasive skin examination methods are also very useful for assigning the margin for excision, thus helping the planning of surgical treatment of lesions to be removed.

Dermoscopy. Visual, light-based non-invasive technologies were utilized in early diagnosis of melanoma since the 1990s [35]. A dermoscope (or dermatoscope) basically is a hand-held, lighted magnifier for skin examination. Dermoscopes typically provide a 6×–10× magnification [51]. Using an oil (or alcohol) interface, reflection, refraction and diffraction of light can be minimized, and the epidermis becomes essentially translucent through the device, thus giving an insight into subsurface structures, *in vivo* [52]. However, the need for these interfaces is already eliminated in newer devices using polarizing light filters that reject surface reflected light (having unchanged polarization) and give insight to even deeper (60–100 μm) structures [53], nevertheless, in the expense of poorer resolution and contrast [52]. Another advanced approach is spectrophotometric (multispectral) dermoscopy – utilizing the fact that larger wavelengths can penetrate deeper – by using lights with different wavelengths in the visible–infrared domain [54]. This method also provides a possibility for quantifying the amount of melanin and several other molecules in skin tissue [55].

Usage of dermoscopy improved the sensitivity and specificity of clinical melanoma diagnosis from 71% to 90% (by almost 20%) [56]. However, it has been shown that experience of the clinician plays an important role in the diagnostic performance of dermoscopy. A comparative study reported that dermatologists with 5 years of experience diagnosed melanoma with 92% sensitivity and 99% specificity rates via dermoscopy, while inexperienced clinicians only reached 69% sensitivity and 94% specificity values [57].

Sequential digital dermoscopy gives the possibility for detecting dynamic changes by comparing images of periodical, follow-up examinations (which is very useful since evolution is a characteristic feature in relation with malignancy, as described above) [58].

The great advantages of dermoscopy are its non-invasiveness, cost- and time-

DOI:10.15774/PPKE.ITK.2020.006

effectiveness (examination time of a lesion takes less than 3 minutes [54]). Drawbacks include the great dependence on the experience of the clinician in diagnostic performance (up to about 20% difference in sensitivity amongst clinicians with different experience). Further drawbacks are its lower accuracy compared to histology and the lack of depth information (eg. vertical extension of a lesion) or of information about the inner structure of the lesion.

Confocal Laser Scanning Microscopy (CLSM). CLSM technology uses a pinhole to exclude light reflected from out of the focus. In this way, a very high spatial resolution (in the order of μm) can be achieved when scanning a 3-D region. On the other hand, a 800–850 nm laser is able to reach 200–400 μm penetration depth. Sensitivity rates of 80–83% and specificity of 96% were achieved when using CLSM for diagnosis of several skin cancer types [58]. As compared to dermoscopy, a 10% higher specificity (97% vs. 87%) was achieved for melanocytic lesions.

The greatest advantage of CLSM-based diagnosis is its high spatial resolution (and thus, good observability of morphological features and microanatomical structures [35]). Some drawbacks are, however, its limited (small) penetration depth, hazard of artifacts (caused by hair strands or movement) and a relatively long examination time (up to 10 minutes) [54].

Optical Coherence Tomography (OCT). In OCT images, contrast is provided based on the differences in light reflectivity of different tissue components and in this way, these images correlate well with pathology [35]. OCT provides a high spatial resolution (in the order of a few μm-s) and a penetration depth of 1–1.5 mm [52]. However, it is very sensitive to artifacts and to attenuation that have a relatively high inter-patient variability [54]. Visualization of non-melanoma skin tumors is better with OCT than that of melanoma (due to the high reflectivity of melanin) [58].

Magnetic Resonance Imaging. MRI is yet only used experimentally for examination of skin diseases. These systems provide high-quality images of the diseases, being useful in education and also in determining precise lesion location for surgical planning. However, diagnostic application is still under future development [59]. Significant drawbacks of using MRI systems are their expensiveness, spacial

DOI:10.15774/PPKE.ITK.2020.006

fixation and requirement of a dedicated staff.

Tape Stripping mRNA. Using an adhesive tape, mRNA sample can be collected from a lesion. Having this sample, genetic information can be acquired from the lesion. A classifier examining a set of 20 genes distincted melanoma from atypical nevi with 100% sensitivity and 90.6% specificity [35]. This technique is therefore promising but not yet applicable in wide-spread use.

Electrical Bioimpedance. Bioimpedence level is dependent on the shape and structure of cells, cell membranes and on water-content of cells. As cancer cells tipically differ from benign cells in their shape, size and orientation, measurement of electrical impedance offers a useful method for differentiating between these cells [35]. Measurements (taking approximately 7 minutes) with the portable and cost-effective impedance-measuring device showed promising results in sensitivity (92–100%) and specificity (67–80%), however, standardization of the results is still required (since electrical impedance of the human skin significantly varies by factors like age, gender, season and location) [35].

Ultrasound (US). US imaging (USI) is a safe, noninvasive and cost-effective, real-time method for examining living tissue [35]. Higher-resolution images can be obtained using US transducers with higher frequency in compromise with a lower penetration depth. For skin imaging, frequencies around (or above) 20 MHz are suitable for use (20 MHz frequency providing a $\sim$80 μm resolution and $\sim$1 cm penetration).

Large field of view, large penetration depth, easy handling, cost-effectiveness and low biological risk are important advantages of US systems for skin examination [60]. Drawbacks are its limited, relatively low resolution and dependence on the experience of the examiner [58].

Since ultrasound imaging is of particular interest for innovation in skin examination (having the above advantages) and is a main topic of the current thesis, it is discussed in more detail in the following section.

DOI:10.15774/PPKE.ITK.2020.006

1.5.5 Ultrasound in skin cancer diagnostics

One of the current roles of US in skin cancer diagnostics is to confirm or exclude the primary diagnosis (before surgical intervention: before the final diagnosis is given by histology). Another role is to measure the vertical (in depth) extension of lesions before surgical treatment to assist planning of excision.

However, there is ongoing investigation for using US systems as a differential diagnostic tool for skin cancer. In a study performed on 4338 lesions, US corrected the diagnoses from 73% to 97% accuracy. The same study presented 99% sensitivity and 100% specificity rates for US-based skin cancer diagnosis [61].

Imaging. US imaging systems can be used to acquire important information from the specimen (such as extension, morphology and structure of a lesion in depth). For imaging of the skin, transducers of 20–50 MHz frequencies are suitable.

US imaging realizes the potential for examining vertical penetration of lesions, measuring extension of lesions, examining the acoustic structure of lesions and detecting possible recurrences.

Some of the problems to face with are that lesions are typically echo-poor, and that resolution is well below histological details [60]. However, differences in echogenicity can be utilized in differential diagnosis (eg. between basalioma and melanoma [62] or between seborrheic keratosis and melanoma [63]).

Contrast enhanced US (with microbubbles added to the bloodstream) highlight the blood vessels of the tumors, providing a new possibility for better distinction between benign and malignant lesions (since tumor vasculature is usually in context with prognosis [64, 65]) [66, 58].

Color Doppler. Another approach to visualize tumor vasculature is the use of Doppler-mode US that is capable of visualizing the presence of vessels as well as velocity and direction of blood flow in the vessels by measuring the frequency-shift of the transmitted signal caused by the moving parts in the sample.

Elastography. Measuring elasticity of a lesion provides a third useful modality in US skin examination. US elastography is a useful assisting tool in differential diagnostics, exploiting the fact of malignant lesions generally being less compressible

DOI:10.15774/PPKE.ITK.2020.006

than healthy tissue. Elastography is capable of enhancing the diagnostic accuracy by 20–25% [67].

1.5.6 Conclusions

As presented above, a wide variety of tools and methods provide possibilities for early stage skin cancer diagnostics. Results of histology are still treated as the "gold standard", however, several more approaches exist to assist diagnostics, having the great advantages of being time- and cost-effective and non-invasive. These methods also help selection of lesions getting into the phase of histological examination.

Usage of ultrasound has a particularly promising and developing field in assisting skin cancer diagnostics with a variety of approaches in itself.

DOI:10.15774/PPKE.ITK.2020.006

Chapter 2

Estimation of Acoustic Power Output from Electrical Impedance Measurements

2.1 Introduction

The measurement of transducer acoustic output – as introduced in Section 1.3 – is necessary for deriving safety indices for diagnostic ultrasound transducers [28]. Acoustic power measurements are also critical for therapeutic treatment scenarios, especially those involving targeted hyperthermia [68].

In the current practice, parameters defining safety (peak rarefaction pressure, spatial-peak temporal-average intensity, temporal-average acoustic power) are measured usually by using either a hydrophone measurement system (for pressure and intensity measurement and sometimes also for acoustic power calculations) or a radiation force balance (for acoustic power measurement) [69, 28]. However, there are several drawbacks for using hydrophone systems, such as the difficulty in measuring high pressures (they generally do not withstand high pressures and/or long pulses) and the time for the setup of field scans required for power calculation. Measurements using a radiation force balance are much more time efficient; however, the specific-purpose devices are relatively expensive (7–24k USD) and therefore unobtainable by many laboratories and institutes with a limited budget. A method of

DOI:10.15774/PPKE.ITK.2020.006

rapidly testing transducers in a cost-effective manner, using otherwise multi-purpose standard laboratory equipment, may be useful in several use cases. Custom-designed transducers may be quickly tested during production without requiring a full characterization. Moreover, during manufacturing, all manufactured items may be tested without the need for random sampling. Lastly, a clinician may test the performance of a transducer over time without requiring access to expensive equipment.

2.1.1 Equivalent circuit models for transducers with reference to the current work

The total power dissipation of a transducer is partially due to electrical losses. Calculating the total power dissipation from electrical impedance measurements may provide an upper limit to the acoustic power output, under the assumption that all electrical power going into the transducer is converted to acoustic power. Since such an assumption is too idealistic and leads to a significant overestimation of the acoustic power output of a transducer, more sophisticated methods are needed for a closer estimation of the electrical losses and acoustic output. There exist methods using equivalent circuit models of transducers for a full description of their electrical and acoustical behaviour [70, 71], the most popular transducer model being the KLM model [20]. However, these methods require extensive knowledge of transducer parameters (such as physical dimensions, acoustic impedance, sound velocity, and the coupling factor of the piezoelectric ceramic) [21] that are not necessarily available when testing. There also exists work, broadly termed the electromechanical impedance technique, that seeks to characterize a material placed on a piezoelectric transducer by measuring the electrical impedance of the two; for a review, see [72]. However, the aim of such work is not to characterize the power output of the transducer itself, but to characterize the loading placed in front of it.

Here, a method for acoustic output power estimation based on ultrasound transducer electrical impedance measurements only is proposed. The transducer is modelled as a two-port network loaded by the acoustic propagation medium, a generalization of the KLM model that retains the linearity and reciprocity assumptions of

DOI:10.15774/PPKE.ITK.2020.006

the latter [21]. Such a lumped two-port model has been used in the literature for electrical matching [73]. Here, the two-port network model parameters are derived by measuring the electrical impedance of the transducer as it is placed in different propagation media (similarly to [74], where the model parameters are used to characterize the properties of a material placed onto the front of the piezoelectric transducer). In the present case, the model parameters are used to estimate the acoustic power dissipation and subsequently compare with acoustic measurements for validation. To the knowledge of the author, this is the first time that changing the exterior loading of a piezoelectric transducer has been used to estimate its output power.

2.2 Theory

In accordance with the KLM model, a piezoelectric transducer is interpreted as a system with three ports. One electrical port connects the transducer to the electrical pulser and signal receiver system. Two acoustic ports represent the connection to the mechanical fields in the front and back acoustic loads (see Figure 2.1). In such a model, V_2 and I_2 stand for the acoustic pressure and particle velocity of the front load, as electrical circuit equivalents. Treating the transducer as a system including the backing load, as well as optional electrical matching circuit as inner parts of the system, the model can be generalized to a two-port network (see Fig. 2.2).

2.2.1 Two-port transducer model

Defining an electrical port as a pair of terminals with equal currents flowing in and out, an electrical circuit with two ports may be treated as a two-port network (Fig. 2.2) defined fully by 4 impedance parameters $Z_{11}, Z_{12}, Z_{21}, Z_{22}$ [75, 76], with state equations:

$$V_1 = Z_{11}I_1 + Z_{12}I_2 \,, \tag{2.1}$$

$$V_2 = Z_{21}I_1 + Z_{22}I_2 \,, \tag{2.2}$$

DOI:10.15774/PPKE.ITK.2020.006

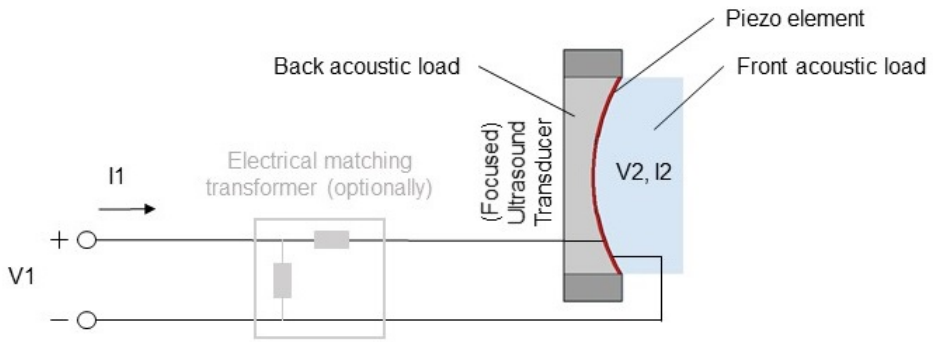

Figure 2.1: Schematic of a single transducer element system, showing electrical connections, back and front acoustic loading, and electrical matching as an optional part of the network. V_1 and I_1 stand for the voltage and current at the electrical port of the transducer, while V_2 and I_2 represent the acoustic pressure and particle velocity of the front acoustic load, seen as a voltage and current, respectively, in the equivalent circuit model.

where V_n, I_n are the voltage at and current going into ports $n \in 1, 2$, respectively (with Z_{mn} $(m, n \in 1, 2)$ impedance parameters describing their interconnections). Placing an acoustic load Z_L at port 2, the input impedance $Z_{in} = V_1/I_1$ "seen" from port 1 is [77]:

$$Z_{in} = Z_{11} - \frac{Z_{12}Z_{21}}{Z_{22} + Z_L} \, . \tag{2.3}$$

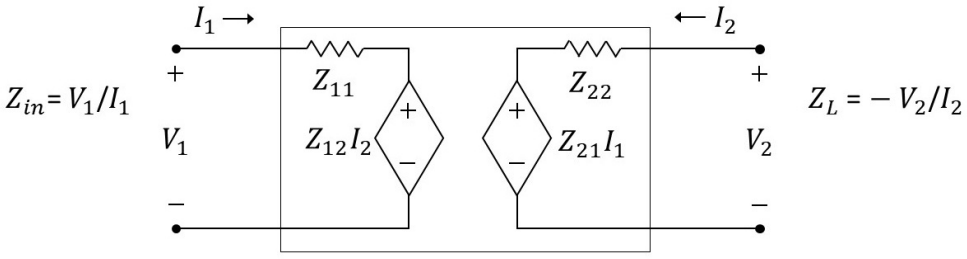

Figure 2.2: Schematic of the two-port network model with impedance parameters $Z_{11}, Z_{12}, Z_{21}, Z_{22}$. Z_L is the load impedance at port 2. The impedance measured at port 1 is Z_{in}.

DOI:10.15774/PPKE.ITK.2020.006

2.2.2 Estimation of two-port model parameters

Rewriting Eq. (2.3) as a linear combination of parameters,

$$[Z_L, -Z_{in}, 1]\mathbf{x} = Z_{in}Z_L \ , \tag{2.4}$$

$$\mathbf{x} = [Z_{11}, Z_{22}, Z_{11}Z_{22} - Z_{12}Z_{21}]' \ . \tag{2.5}$$

The system of equations in Eq. (2.4) is currently not unique for the four impedance parameters of $\mathbf{x}$ (Eq. (2.5)). However, using the assumption of reciprocity, generally true for circuits containing passive elements only and shown to be true for the KLM model [21],

$$Z_{12} = Z_{21} \ . \tag{2.6}$$

During the calculation of the impedance parameters, the square root of $Z_{12}Z_{21}$ is taken, which gives a positive real impedance value for both Z_{12} and Z_{21}.

Since there are three unknown terms remaining in $\mathbf{x}$, at any given frequency, measurements of the input impedance Z_{in} using at least three different acoustic loads Z_L allows an estimate of the parameter vector $\mathbf{x}$ to be obtained using matrix inversion. The equation system will have a unique solution as long as the impedance properties of the three loads are different.

2.2.3 Derivation of power from two-port model parameters

The total power consumption P_t of the transducer can be calculated from the root mean squared drive voltage $V_{1,rms}$ and from the input impedance $Z_{in_{medium}}$ measured for the system with a specific load medium (as observed from port 1 of the network model) using the following expression:

$$P_t = \frac{|V_{1,rms}|^2}{Z_{in_{medium}}} \ . \tag{2.7}$$

In a similar way, the acoustic power P_a transmitted into the medium can be calculated from the root mean squared output voltage $V_{2,rms}$ of the two-port network model and from the impedance of the load medium $Z_{L_{medium}}$:

$$P_a = \frac{|V_{2,rms}|^2}{Z_{L_{medium}}} \ . \tag{2.8}$$

DOI:10.15774/PPKE.ITK.2020.006

It is noted here that for biomedical applications, water will be used as the reference medium for power consumption and transmission (total power and acoustic output power) calculations.

To give an expression for P_a in terms of impedance parameters and the drive voltage $V_{1,rms}$ only, V_2 (and thus, $V_{2,rms}$) are to be expressed in terms of voltage V_1 and impedance parameters $Z_{11}, Z_{12}, Z_{21}, Z_{22}$ of the two-port network. Rearrangements of Eqs. (2.1) and (2.2) and use of the equation describing the relationship between the physical quantities at port 2 of the model (see Figure 2.2):

$$V_2 = -Z_L I_2 \tag{2.9}$$

lead to such expression in the following way.

For a first step, currents I_1 and I_2 are to be eliminated from the expressions. Rearrangement of Eq. (2.1) yields:

$$I_2 = \frac{V_1 - Z_{11} I_1}{Z_{12}} \,, \tag{2.10}$$

while a similar rearrangement of Eq. (2.2) yields:

$$I_1 = \frac{V_2 - Z_{22} I_2}{Z_{21}} \,. \tag{2.11}$$

Using Eq. (2.11), Eq. (2.10) becomes:

$$I_2 = \frac{V_1 - Z_{11} \frac{V_2 - Z_{22} I_2}{Z_{21}}}{Z_{12}} \,. \tag{2.12}$$

Rearrangement of Eq. (2.12) leads to:

$$I_2 = \frac{Z_{11} V_2 - Z_{21} V_1}{Z_{11} Z_{22} - Z_{21} Z_{12}} \,. \tag{2.13}$$

Using this expression for I_2 (Eq. (2.13)), Eq. (2.9) becomes:

$$V_2 = -Z_L I_2 = \frac{Z_L Z_{21} V_1 - Z_L Z_{11} V_2}{Z_{11} Z_{22} - Z_{21} Z_{12}} \,. \tag{2.14}$$

Rearrangement of Eq. (2.14) leads to:

$$V_1 = \frac{Z_L Z_{11} + Z_{11} Z_{22} - Z_{12} Z_{21}}{Z_L Z_{21}} V_2 = \left[\frac{Z_{11}}{Z_{21}} \left(1 + \frac{Z_{22}}{Z_L} \right) - \frac{Z_{12}}{Z_L} \right] V_2 \,, \tag{2.15}$$

which gives:

$$V_2 = \left[\frac{Z_{11}}{Z_{21}} \left(1 + \frac{Z_{22}}{Z_L} \right) - \frac{Z_{12}}{Z_L} \right]^{-1} V_1 \,. \tag{2.16}$$

DOI:10.15774/PPKE.ITK.2020.006

Expressing all voltages in terms of their root mean squared (rms) value, the average power dissipated on the acoustic load is:

$$P_a = \frac{|V_{2,rms}|^2}{Z_L} = V_{1,rms}^2 \frac{Z_L}{\left|\frac{Z_{11}}{Z_{21}}(Z_L + Z_{22}) - Z_{12}\right|^2} \,. \tag{2.17}$$

Please note that the acoustic load Z_L in the electrical circuit encapsulates all the acoustic dissipation into the acoustic medium, while the purely electrical dissipation is contained in the two-port network. Please also note that Z_L can be defined as any multiple of the acoustic impedance, with the two-port network ensuring the appropriate conversion between electrical and acoustic impedance. For simplicity, the acoustic load used is simply the acoustic impedance. The above considerations are analogous to the ones made in the KLM model [21], although the proposed model has a more general and therefore simplified form.

2.3 Materials and methods

In this section, a description is provided of the experiments conducted to assess the validity of the proposed method. First, electrical impedance measurements were made with two high-intensity focused ultrasound (HIFU) transducers loaded in turn with three distinct fluid media. Data collected from these measurements were processed according to Section 2.2.2 to yield estimates of radiated power. Acoustic field measurements were then made in the focal planes of the HIFU transducers in order to gain independent estimates of radiated power. Finally, the pressure range of applicability was assessed through a series of additional acoustic and electrical measurements performed with drive levels producing pressures up to approximately 20 MPa. Details are provided in the following subsections.

2.3.1 Transducers Used for the Measurements

Two spherically-focused HIFU transducers (Sonic Concepts, Bothell, WA, USA) were used for measurements at both their fundamental and 3$^{\text{rd}}$ harmonic frequencies: H-102, SN: B-022 (1.060/3.190 MHz) and H-107, SN: 031 (0.5/1.7 MHz). The fundamental and 3$^{\text{rd}}$ harmonic bandwidths, as defined by the manufacturer, down to

DOI:10.15774/PPKE.ITK.2020.006

-3dB normalized to a perfect 50 Ω match, were 640/700 kHz (H-102) and 340/80 kHz (H-107). The H-102 and H-107 transducers had a rectangular and circular cutout, respectively, modifying their surface areas from 32.2 to 26.5 cm^2 and 32.2 to 30.8 cm^2, respectively (Figs. 2.4 and 2.5).

For experimental validation of the theory presented in Section 2.2, the acoustic power dissipation was estimated from electrical impedance ("Z") measurements and compared with the corresponding acoustic measurements (acoustic power dissipation calculated from measurements of pressure "p") as a reference (Fig. 2.3), as described in the following subsections. These measurements were performed for both transducers with both of their driving frequencies.

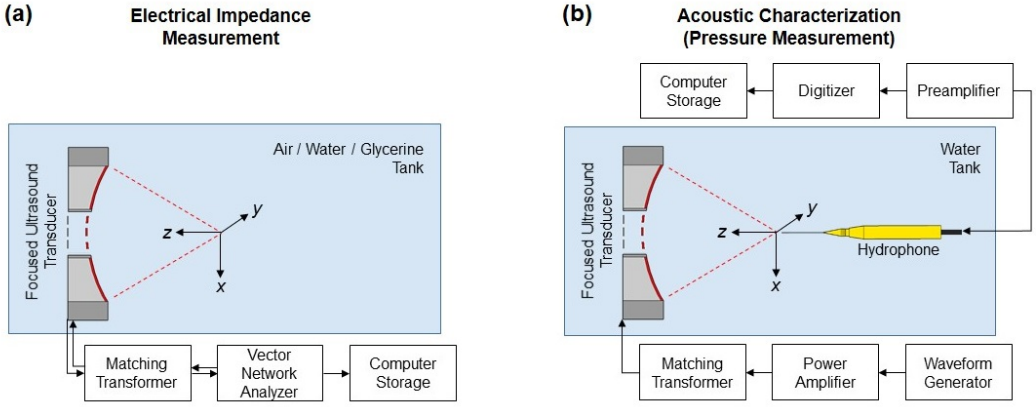

Figure 2.3: Setup of the ***(a)*** *electrical impedance measurements (Section 2.3.2) and of the* ***(b)*** *acoustic characterization (pressure measurements from which acoustic power was calculated; see Section 2.3.3).*

2.3.2 Electrical impedance measurements

Electrical impedance measurements were performed using a Bode 100 vector network analyzer (Omicron Lab, Klaus, Austria), in the frequency range of 100 Hz–4 MHz. The input signal source for the impedance measurements was a continuous wave sinusoid, and a 1 kHz receiver bandwidth was used. Each HIFU transducer had a matching transformer; all electrical measurements were made at the transformer input (Figure 2.3a). During the measurements, the transducer was placed into three

DOI:10.15774/PPKE.ITK.2020.006

easily obtainable and safe media with known acoustic impedances: air, water, and 87.5% glycerine, with characteristic acoustic impedances of 0.4×10^{-3}, 1.50, and 2.06 MRayl (10^6 Rayleigh) assuming linear mixing for glycerine [78]. Since inadvertent physical movement of the transducer cable could potentially change its impedance, care was taken to not move it while the propagation media was being changed.

The acoustic power output was estimated from the impedance measurements with MATLAB (Mathworks, Natick, MA) using the proposed method (Section 2.2). Since the two-port model automatically adapts to the conversion factor used, for simplicity, a conversion factor of 1 Ω/Rayl was used when defining the load impedances Z_{L_m}.

The two-port network parameters $Z_{11}, Z_{12}, Z_{21}, Z_{22}$ were calculated by solving the set of linear equations Eq. (2.4) for $\mathbf{x}$ (defined in Eq. (2.5)).

As mentioned in Section 2.2.2, impedance measurements using three different materials (a, w, g) for load provide an equation system of 3 equations as follows (according to Eq. (2.4)):

$$\begin{bmatrix} Z_{L_a} & -Z_{in_a} & 1 \\ Z_{L_w} & -Z_{in_w} & 1 \\ Z_{L_g} & -Z_{in_g} & 1 \end{bmatrix} \begin{bmatrix} Z_{11} \\ Z_{22} \\ Z_{11}Z_{22} - Z_{12}Z_{21} \end{bmatrix} = \begin{bmatrix} Z_{in_a}Z_{L_a} \\ Z_{in_w}Z_{L_w} \\ Z_{in_g}Z_{L_g} \end{bmatrix}, \tag{2.18}$$

where Z_{in_m} are impedances measured using the load material m and Z_{L_m} are the characteristic acoustic impedances of the material m ($m \in a, w, g$).

From the equation set (of 3 equations for 3 materials), the parameter vector $\mathbf{x}$ was calculated using matrix inversion. Parameters $Z_{11}, Z_{12}, Z_{21}, Z_{22}$ of the two-port network model were then calculated from the parameter vector $\mathbf{x}$ defined by Eq. (2.5) and by using the assumption of reciprocity of Eq. (2.6).

The estimated impedance coefficients were used to derive acoustic power consumption as well as total power consumption for unit peak drive voltage ($V_1 = 1$ V) with water as the acoustic load. Total power consumption P_t was calculated using Eq. (2.7) for the root mean square drive voltage $V_{1,rms}$ and for the impedance of the whole system with water load (as observed from port 1 of the network model) $Z_{in_{water}}$. In a similar way, transmitted acoustic power P_a was calculated using

DOI:10.15774/PPKE.ITK.2020.006

Eq. (2.17) with the acoustic impedance of water as the load material ($Z_{L_{water}}$). The efficiency of the transducer at a given frequency was calculated as the ratio of the transmitted acoustic power (P_a) and the total power (P_t), in %.

2.3.3 Acoustic characterization

Direct measurements of radiated acoustic pressure were carried out with the transducers submerged in a tank filled with filtered and degassed water. For each transducer/frequency combination, a drive signal was provided by a waveform generator (Agilent 33225A, Santa Clara, CA, USA) connected to a power amplifier (Model 1140LA, E&I limited, Rochester, NY, USA) as shown in Fig. 2.3. The drive signal consisted of two-cycle bursts having a center frequency defined by the manufacturer at the fundamental or third harmonic resonance of the transducer, with the short burst typically providing at least 300 kHz of usable processing bandwidth. The focal plane pressure fields were measured with a calibrated needle hydrophone (HNC0400, [Onda Corp, Sunnyvale, CA, USA] for 500 kHz, or PA0200 [Precision Acoustics, Dorset, UK] for higher frequencies). Hydrophone positioning and data acquisition was coordinated by software control (UMS, Precision Acoustics). Spatial measurement ranges were chosen to capture at least three sidelobes, as verified by preliminary line scans. Additional measurements were made on the H-107 transducer at higher amplitudes and varying pulse lengths in order to assess the validity of the proposed power estimation method with respect to drive scaling and system linearity.

For estimates of radiated power, the point-by-point field measurements $h(t)$ were first Fourier transformed $F[\,]$ and normalized by the transform of the drive voltage $V_d(t)$ and the hydrophone calibration $M_h(t)$ to yield pressure spectra per unit drive voltage:

$$p(f) = \frac{F\left[h(t)\right]}{F\left[V_d(t)\right] M_h(f)}. \tag{2.19}$$

Radiated power was then found by numerically integrating the pressures under the assumption of locally planar propagation:

$$P(f) = \frac{1}{2\rho c} \iint_A |p(f)|^2 \, dA, \tag{2.20}$$

DOI:10.15774/PPKE.ITK.2020.006

where the integration area dA is taken from the scan step size (0.1 mm) and the ambient sound speed c was found from a temperature-speed relationship [79] and a thermocouple measurement made during the scan.

Initial measurements of acoustic pressure did not all have sufficiently broad spatial and frequency coverage to accurately calculate radiated power. Upon determining this, the measurements were repeated with a broader spatial and frequency span. However, it was found upon this repeat that the H-107 matching transformer for the 3rd harmonic frequency band had been damaged in the interim. Since the beam patterns (where they overlapped) had not changed, but the response spectrum did, the H-107 power was estimated using a pressure defined by: $p(f,x,y) = p_o(f,0,0) * H_r(f,x,y)$, where p_o is the original pressure measurement made in the center of the focal plane, and H_r is the focal plane beam pattern made during the repeat measurements. Power was then estimated using Eq. (2.20).

As a consistency check, this process was also done for the fundamental frequency. Comparison of the modified calculation and one made entirely based on the repeat measurements of both pressure and beam pattern showed agreement within 16.73% for the fundamental frequency.

2.3.4 Measurements Validating the Range of Linearity for the Model

The estimate of acoustic power output from a given voltage input relied on a linear model. The electrical impedance measurements were done using a small current injection so their linear extrapolation should work as long as the acoustic output was in the linear range. To demonstrate the validity of linearity in terms of drive voltage, measurements were performed as follows.

The H-107 transducer was driven in its 3$^{\text{rd}}$ harmonic band over a range of amplitudes so that the final peak to peak pressure was just over 20 MPa. Fields were measured with a membrane hydrophone (D1602, Precision Acoustics, Dorset, U.K.) whose frequency response was flat within 1%–2% over the 1–20 MHz range allowing determination of calibrated pressure as harmonics appeared in the received wave-

DOI:10.15774/PPKE.ITK.2020.006

forms. The hydrophone was scanned through a radial line spanning ±6 mm about the focus for each drive level, and the scan data were processed to yield acoustic power estimates as described above (Eq. (2.20)). Electrical impedance was also measured, using a current probe (4100, Pearson Electronics, Palo Alto, CA, USA) and a voltage probe (PP017, LeCroy, Geneva, Switzerland) connected to the amplifier output.

2.4 Results

2.4.1 Comparison of estimated and measured acoustic powers

Results are shown here in terms of power and efficiency. As an example, in the top row of Fig. 2.4 (b,c), the estimated (from impedance "Z") and measured (from pressure "p") acoustic powers are compared in relation to the total (electric and acoustic) power calculated from impedance measurements (Section 2.3.2). The lower plots (d,e) show efficiency calculated for both estimation and measurement of acoustic power, using the data of the plots at the top (b,c).

The results for four cases of transducer and driving frequency combinations (see Figs. 2.4–2.5) indicated that the method presented in this paper gave an estimation in between the total power and the measured acoustic power values. A good agreement was found in the frequency dependency of these three values, with estimations being closer to the measured acoustic power for frequencies near the third harmonic, coupled with a lower efficiency. At the nominal transducer resonance frequencies, the estimated/measured powers were 6.7/5.0 mW (H102, 1.06 MHz) 4.3/3.6 mW (H102, 3.19 MHz), 8.1/6.2 mW (H107, 0.5 MHz) and 5.2/4.4 mW (H107, 1.7 MHz). The mean absolute difference between estimated and measured power, in % of the average measured power, was 17.0% and 4.5% for H102 fundamental and third harmonic; 21.8% and 7.8% for H107 fundamental and third harmonic. The impedance-based power predictions were consistently above the acoustic measurements, at most ex-

DOI:10.15774/PPKE.ITK.2020.006

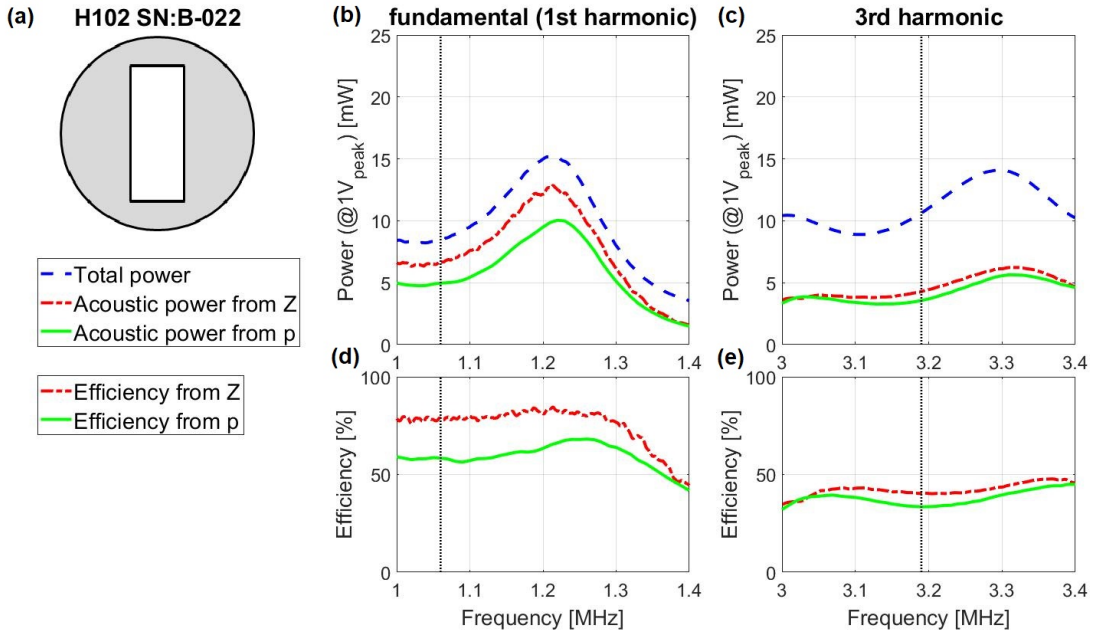

Figure 2.4: Comparison of electrically estimated (from impedance "Z" measurements) and acoustically measured (estimated from acoustic pressure "p" field measurements) power outputs (1 V peak drive voltage) of the H-102 (SN: B-022) transducer. ***(a)****: Transducer surface schematic with the cutout.* ***(b,c)****: Total (electric and acoustic) power and estimated and measured acoustic power.* ***(d,e)****: Estimated and measured efficiency. The dotted vertical lines indicate the centre frequency defined by the manufacturer at the fundamental and third harmonic resonances of the transducer.*

ceeding it by 34%. The acoustic measurements themselves had an uncertainty of around 32% (in accordance with 15% hydrophone calibration uncertainty for pressure). The uncertainty of the impedance-based method was estimated to be between 0.7 and 7.1% depending on the device and its drive band.

Explaining the above, the uncertainty of the impedance measurement-based method was estimated based on the uncertainty of the impedance measurements. Multiple (3–8) measurements were performed for each transducer placed in each material (air, water, glycerine). Impedance measurements showed significant accordance. Variability analysis showed the worst-case (biggest) standard variation being 2.91 Ω (0.86% of the highest impedance measured), while the mean standard varia-

DOI:10.15774/PPKE.ITK.2020.006

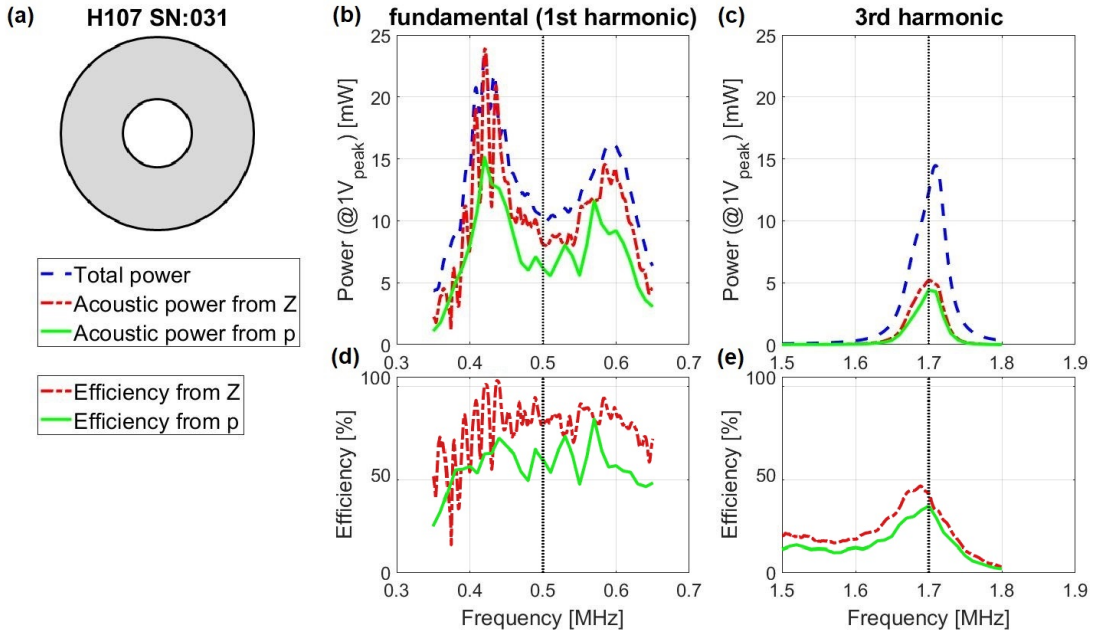

Figure 2.5: Comparison of electrically estimated (from impedance "Z" measurements) and acoustically measured (estimated from acoustic pressure "p" field measurements) power outputs (1 V peak drive voltage) of the H-107 (SN: 031) transducer. ***(a)****: Transducer surface schematic with the cutout.* ***(b,c)****: Total (electric and acoustic) power and estimated and measured acoustic power.* ***(d,e)****: Estimated and measured efficiency. The dotted vertical lines indicate the centre frequency defined by the manufacturer at the fundamental and third harmonic resonances of the transducer.*

tion for all frequencies of all measurements for both transducers was 0.18 Ω (0.05% of the highest impedance measured and 2.12% of the average of all impedances measured).

From the impedance measurements, the highest difference from the average was calculated for each frequency of interest, for all four cases of transducer and driving frequency combinations, for all three materials, and for the real and imaginary parts of the measured impedance, separately. The calculated values were used as the standard deviation of the Gaussian random noise added to the relevant impedance measurements (of the measurements presented in this thesis, in Section 2.4). Power estimates were calculated, and the uncertainty of the method was estimated as

DOI:10.15774/PPKE.ITK.2020.006

the mean absolute difference of the power estimate using noisy measurement data compared to the power estimate calculated from the noiseless measurement data presented in this thesis and normalized by the average total power of the latter.

Repeating the above calculation for 1000 different Gaussian random noises, for each transducer and driving frequency combinations, gave the following results. The maximal mean absolute differences of the power estimate from noisy and noiseless measurement data were 1.1%, 0.7%, 7.1% and 1.7% for transducers and driving frequencies of the H-102 fundamental, H-102 third harmonic, H-107 fundamental, and H-107 third harmonic, respectively.

2.4.2 Linearity of the Model

The linearity of the transducer response, in terms of pressure-voltage correlation, was assumed when suggesting that the small-signal impedance measurements used to estimate the power output of the transducer were valid over a higher voltage range, as well as for a broad frequency range.

A wide range of linearity was verified for the proposed model by measurements performed as described in Section 2.3.4. Results are shown in Fig. 2.6.

Fig. 2.6a shows the peak positive and negative pressures measured at the focus of the H-107 transducer and includes all frequency content up to 20 MHz. From the asymmetry of the values, the waveform clearly exhibited nonlinear behaviour even at low drive levels ("drive amplitude" is the amplifier output).

Fig. 2.6b shows the values of electrical impedance Z_e at 1.7 MHz as determined from voltage and current probes at the amplifier output terminal. The datasets had standard deviations of $< 2\%$ over the drive range. At the higher drive levels, small nonlinearities did show up in the drive spectrum (not shown on the figure), but they were no larger than 1/20th of the 1.7 MHz amplitude. All this suggested that the nonlinearities were primarily in the water, not in the drive chain (as expected). Because the electrical impedance was essentially invariant with driving amplitude, this further validated the use of the proposed model for higher driving voltages.

In Fig. 2.6c, the computed radiated powers are shown in two forms: using the full

DOI:10.15774/PPKE.ITK.2020.006

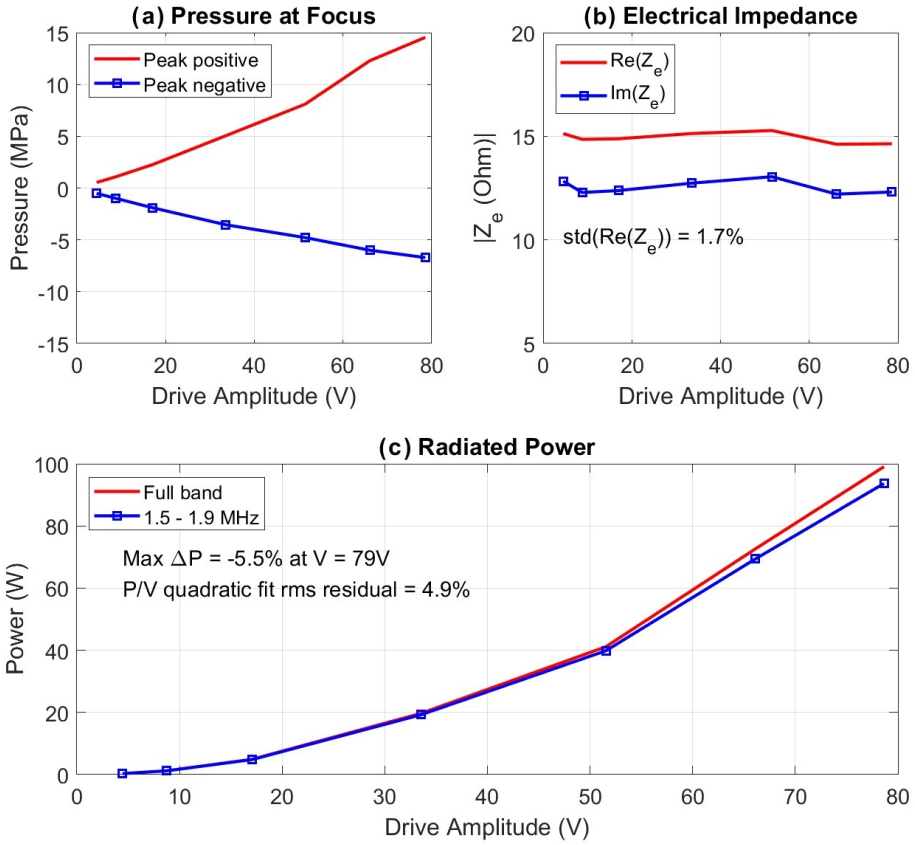

Figure 2.6: Validation of the small-signal electrical impedance measurement results to higher driver voltages (resulting in higher pressures and powers). ***(a)*** *Focal pressure,* ***(b)*** *electrical impedance, and* ***(c)*** *radiated power measurements as a function of drive voltage in the range of 4–80 V showing the linearity of the pressure-voltage correlation, in the case of the third harmonic band (∼1.7 MHz) of the H-107 (SN: 031) transducer.*

bandwidth of the data and only keeping the part that was in the 1.5–1.9 MHz band. The latter presumably was what would come from the electrical impedance-based predictions. At the highest drive level, the band-limited power estimate was only 5.5% lower than the full band. This was largely as expected when the nonlinearity was occurring locally in the focus due to elevated pressures. The main lobe peak had a minimal contribution to the total power because there was very little corresponding area through which energy flowed at the peak intensity. For pressures in the range reported here, similar observations were made regarding heating of tissues with

DOI:10.15774/PPKE.ITK.2020.006

focused beams: nonlinearity may produce a waveform distortion, but it did not necessarily impact spatially cumulative outputs that were quadratic in pressure (e.g., power, heat deposition). Finally, the power–voltage curves followed the expected quadratic dependence, with a residual difference of about 5%.

In summary, the proposed method did not appear to be limited by deviations from linearity (or voltage scaling as presented above) for this transducer for up to 20 MPa peak-peak pressure. This pressure range is relevant to many therapeutic scenarios, and therefore, the association with "HIFU" is appropriate based on these findings.

2.5 Discussion

2.5.1 Interpretation of transducer-specific phenomena affecting measurements

As shown in Figs. 2.4–2.5, efficiency values at the fundamental frequency were significantly lower for measured acoustic power than for electrical impedance-based estimations, in all four cases. The efficiency estimates were also lower than the values reported by the manufacturer for a representative transducer (with different SN), being 87% and 80% at fundamental and third harmonic frequencies. However, the representative transducer did not have a cutout, and having cutouts of any shape (and the resulting boundary conditions and vibration shapes) could impact the power estimates via the input energy going into subsonic vibrations (such as bending or surface wave motion) near the edges of the ceramic, rather than deformation that produces volume change and efficient radiation. In this way, some energy may be dissipated in ceramic losses and kinetic energy of the loading fluid (water), near the edges. Assuming that the edge "losses" scale with the wavelength may explain the larger difference between estimated and measured acoustic power for the fundamental frequency than that for the third harmonic.

Conceivably, a larger transducer with greater surface area to edge length would be less susceptible to the proposed loss mechanism. To the author's knowledge, all

DOI:10.15774/PPKE.ITK.2020.006

clinical HIFU transducers (unless array-based) would fit this description. Another potential loss mechanism at lower frequencies would be coupling into the transducer body (side walls). In a transducer without a cutout, an even closer correspondence of the presented impedance-based estimates of the acoustic power dissipation with the real dissipation shown by reference acoustic measurements would be expected.

The acoustic resonance frequencies, as measured using electrical impedance and acoustic measurements, are seen to be in close agreement in Figs. 2.4–2.5. However, there were discrepancies with the values provided by the manufacturer. This could be due to several factors, including changes of transducer properties with time and handling.

2.5.2 Scaling of the results

The results presented in this work were measured and calculated for unit voltage amplitude. Projections to a given drive voltage amplitude should consider both the electrical and acoustic linearity of a specific transducer for a drive voltage and frequency range. Note that, with the assumption of linearity, the power output increased as the square of voltage (meaning that a 32 V drive would scale the plots of Figs. 2.4–2.5 from mW to W), and for HIFU applications, even higher voltages (e.g., 50 V and higher) were typically used. As long as the model was applied in its linear range, the relative (%) errors (Section 2.4.1) remained valid.

The effect of drive level on the scaling of model results was evaluated with the H-107 transducer, with measurements made of the drive voltage, drive current, and focal plane acoustic pressure (Subsection 2.4.2). For drive amplitudes between 4 and 79 V, the electrical impedance in the "drive band" (1.6–1.8 MHz) exhibited negligible variation (1.7% standard deviation). At the highest drive amplitude, the focal pressure waveform was highly nonlinear, with a peak-to-peak value of approximately 20 MPa. Still, the estimated radiated power followed a simple quadratic relationship with drive voltage over the range tested. This presumably was because the amplifier-transducer system behaved linearly, and the nonlinear response of the medium (water) was not strong enough to cause meaningful thermo-viscous losses that would appear as a loss of beam power. Further study would be required to

DOI:10.15774/PPKE.ITK.2020.006

evaluate other transducer systems and drive conditions. However, the data in this study confirmed that the proposed method was valid even when the response of the medium yielded strongly nonlinear waveforms.

2.5.3 Potential advantages of the proposed method

The primary advantage of the proposed method is its cost-effectiveness. The liquids used for the presented measurements are commonly available lab supplies, and the electrical impedance measurement could be done with probes or simple circuits if an impedance analyzer was not available. Another advantage is its simplicity. It only requires changing the media in which the transducer is placed and performing quick impedance measurements in each. There is no need for precise setting of the orientation of the transducer if the tank is large enough. A further advantage is time-effectiveness. An electrical impedance measurement only takes about a few seconds for a frequency range of tens of MHz. Including the changes of propagation media, the three measurements can be done within 15 minutes, approximately.

Future work could investigate the use of media with an even higher acoustic impedance than glycerine to ensure a higher contrast in electrical impedance values, the expected effect being to reduce sensitivity to measurement errors.

2.6 Conclusions

A method for acoustic power output estimation of ultrasound transducers was proposed in this chapter, based on simple electrical impedance measurements in three different propagation media and requiring knowledge only of the relative characteristic acoustic impedances of these media. Results showed agreement of estimated acoustic power outputs (based on electrical measurements) with relevant reference acoustic measurements, for four cases of transducer and driving frequency combinations. Since the estimates were consistently above the measured acoustic values, but never more than 34% above the acoustically measured power, they may potentially be useful for providing an upper bound for ultrasound exposure safety analyses. Quantitatively, a 21.8% overestimate as seen with the H-107 fundamental would

DOI:10.15774/PPKE.ITK.2020.006

translate to a 10.4% overestimate in pressure, which is similar to the maximum uncertainty in a direct measurement with a hydrophone. Drive scaling analyses indicated that the proposed method could yield valid power estimates even when the output waveform was highly nonlinear, making it suitable for many HIFU calibration scenarios.

Although estimates of acoustic power dissipation may be used to estimate acoustic intensity and pressure output, this was left out of the scope of this thesis as the calculations involve considerable deliberation [68]. However, with future work, the proposed time-, complexity-, and cost-effective method may be elaborated to give predictions on the mechanical index (MI) and thermal index (TI) used to characterize ultrasound transducer safety for diagnostic and therapeutic applications (see Section 1.3). Such a method would be of great benefit for making quick and simple independent measurements both in industrial and clinical environments, filling a gap for laboratories and institutes with a limited budget.

DOI:10.15774/PPKE.ITK.2020.006

Chapter 3

Decorrelation Ultrasound for Observation of Dynamic Biological Changes

3.1 Introduction

Decorrelation ultrasound (here after DECUS) is being increasingly used to investigate long-term biological phenomena such as response to therapy or slow blood perfusion in the capillaries [80, 81, 82]. DECUS is useful for obtaining information from dynamic changes (eg. characterizing changes in a time-domain sequence of some data). For a temporal sequence of ultrasound signals, it can provide important and quantitative information about scatterer dynamics. As shown by Abbey et al. [80], static, dynamic scatterers as well as noise can be quantitatively separated via decorrelation.

A potential application of DECUS is the investigation of postmortem effects in tissue. To the best knowledge of the author, the results of such experiments have not yet been published in the literature. Post-mortem tissue effects – such as post-mortem blood movements, *rigor mortis*, or decomposition) occur over the time-courses of several minutes to hours (or even days, months), thereby making conventional ultrasound Doppler techniques unusable. The investigation of these effects is of potential interest in forensics, such as in understanding the post-mortem

DOI:10.15774/PPKE.ITK.2020.006

redistribution of various drugs [83].

In the presented work, ultrasound image sequences of mice who did not survive anesthesia (in a separate investigation) were analyzed and post-mortem tissue effects were observed via decorrelation calculation. A method was developed to obtain a quantitative parameter characterizing the rate of decorrelation. The results showed that ultrasound decorrelation imaging is an effective and promising method of observing post-mortem tissue effects and pointed to further studies elucidating the mechanism behind these effects.

3.2 Background

As described by Abbey et al. [80], comparing images generated in the same spatial frame – but at different moments in time – makes it possible to differentiate between components of the imaged object, based on signal statistics.

Three basic components can be identified in the cumulative signal correlation data (Fig. 3.1). The correlation contribution of static scatterers is constant. However, contribution of dynamic scatterers to the overall signal correlation is decaying in time: it is assumed to show an exponential decay. The third component is noise (arising from the way of data acquisition), which is assumed to be totally uncorrelated in time, so that its decorrelation component has the form of a Dirac delta function.

Measuring and examining the overall correlation of images (a series of images in time) as a function of time gives important information about the components of the (image) signal. (The term 'overall correlation' is used here for the Pearson correlation value of a pair of entire images.) The drop in the beginning of the cumulative correlation function (the drop between the autocorrelation value (1.0) of the first image and the correlation value measured for – the first – two different images) accounts mostly for the effect of noise. The limiting value of the decaying function (ideally) represents the total contribution of static scatterers to the overall (cumulative) signal (image) correlation. The interval between the correlation contribution level of static scatterers and the highest value of the cumulative correlation signal,

DOI:10.15774/PPKE.ITK.2020.006

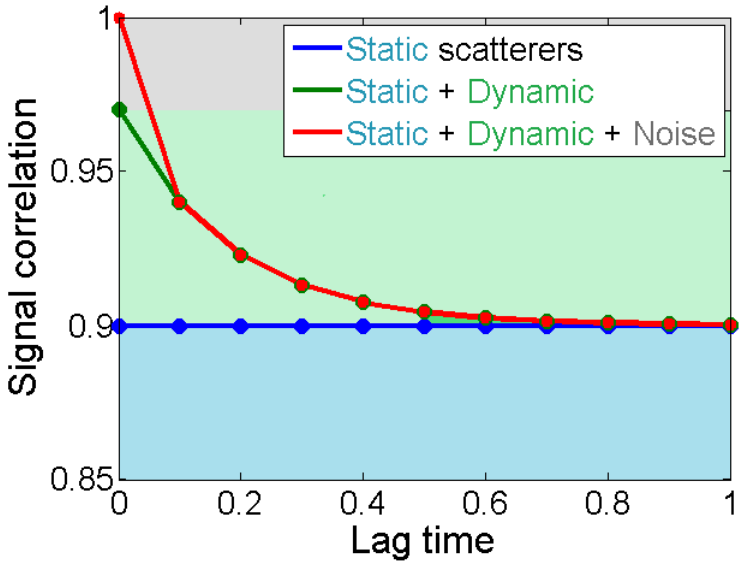

Figure 3.1: Components of the cumulative correlation signal. Modified from [80, p. 2254].

right after the drop referring to noise, shows the contribution of dynamic scatterers. (To be accurate, the joint ratio of dynamic and static scatterers up against noise can be determined by estimating the initial point of the decaying function: in this way, the contribution of dynamic scatterers and noise can be distinguished in the initial drop.) This interval makes it possible to calculate the proportion of dynamic scatterers versus static scatterers in the imaged region. By examining the decaying function, temporal changes in the imaged object can be characterized quantitatively by calculating a time constant for the decay – as it will be presented in the following sections.

As has been shown above, using statistical signal analysis, dynamic processes can be analyzed quantitatively and important information can be collected about static, dynamic and noise components of signals to be analyzed via correlation measurement.

DOI:10.15774/PPKE.ITK.2020.006

3.3 Materials and methods

The proposed DECUS method quantifying image dynamics by calculating time constants for the decaying decorrelation functions has been applied to the investigation of post-mortem tissue effects being a potential application as mentioned in the Introduction (Section 3.1).

3.3.1 Data acquisition

Ultrasound (US) images of nude mice were collected under anesthesia as part of a separate investigation into cancer growth of xenografts implanted into their hind legs. Two of the mice did not survive the anesthesia procedure and ultrasound images were obtained post-mortem. To investigate post-mortem changes to tissue, a sequence of ultrasound images were collected at regular time intervals. The linear array transducer was kept in a fixed location observing the hind legs of the animal. An Analogic US research system (BK Medical, Denmark) was connected to the 5–12 MHz linear array providing an image resolution of $\sim 800\ \mu m^2$ in terms of pixel area.

Hereinafter, results are presented using two separate sequences of ultrasound images, one from each of the mice. One was a 53 minutes long sequence with 10.6 s time intervals. The other sequence of images was collected in 36 hours using a time interval of 5 minutes. Based on these two image sequences, long-term tissue effects could be observed as well as short-term changes (the latter with a higher temporal resolution).

3.3.2 Decorrelation analysis

In order to get an insight into the dynamics of the imaged tissues, decorrelation analysis was done separately for each spatial location – for every image pixel in the ultrasound image frame (see Fig. 3.2.a). For each pixel, the normalized autocorrelation function of the temporal RF (radiofrequency) signal amplitude changes was calculated for positive time lags (see Fig. 3.2.b). The initial parts of the autocorrelation functions fitted well to an exponential decay. Therefore, to estimate the rate of decorrelation, a time constant was calculated for each pixel via exponential curve

DOI:10.15774/PPKE.ITK.2020.006

fitting (see Fig. 3.2.c).

The method used for exponential curve fitting was based on the mathematics of the gradient of exponential functions. Namely, for an exponentially decaying function f (with amplitude A and time constant τ):

$$f(t) = Ae^{-t/\tau}, \tag{3.1}$$

the gradient of the function is:

$$f'(t) = -\frac{1}{\tau}Ae^{-t/\tau} = -\frac{1}{\tau}f(t). \tag{3.2}$$

Thus, the time constant of the function can be determined using the following equation:

$$\tau = -\frac{f(t)}{f'(t)}. \tag{3.3}$$

Given the estimated time constants τ for each spatial location in the image frame, dynamic behavior of scatterers in different spatial locations was visualized by creating a map of τ (using the same image frame as for the acquisition of data – see Fig. 3.2.c).

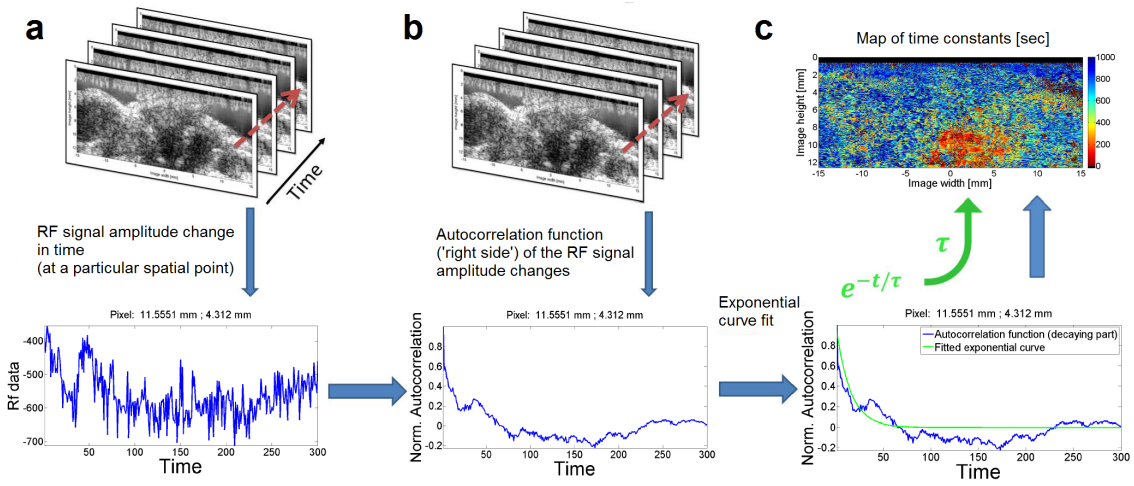

Figure 3.2: Method for calculating the map of time constants via exponential curve fitting to autocorrelation functions of pixelwise temporal RF signal changes. ***(a)*** *Observed RF signal amplitude change in time (for a given pixel);* ***(b)*** *Calculation of autocorrelation functions (for positive time lags);* ***(c)*** *Spatial map of time constants calculated from fitted exponential curves.*

DOI:10.15774/PPKE.ITK.2020.006

3.4 Results

3.4.1 Tissue changes on small time-scale (seconds – 1 hour)

In the case of the 53-minute-long acquisition (10.6 s temporal resolution), relatively "short-term" post-mortem tissue effects were observed. One of these effects is post-mortem blood movement which phenomenon is discussed in [83].

The map of time constants – calculated via exponential curve fitting to the pixelwise temporal autocorrelation functions (see Fig. 3.2) – is shown in Fig. 3.3. The regions with smaller time constants correspond to the more dynamically changing regions observed in the original B-mode US image flow (see Fig. 3.4 as an illustration and reference for Fig. 3.3).

In some well-defined regions – like the central ventral region of the animal (region between −1–4 mm axially, 8–12 mm laterally) – periodic changes were observed qualitatively in the B-mode image sequence. Autocorrelation sequences showed a relatively fast decay rate for these regions (characterized by time constant values of around 100 seconds) and also showed an oscillatory component with a periodicity in the range of 10–15 minutes (see Fig. 3.5). Since the abdominal aorta of the mouse was located in the area mentioned above, the occurrence of this oscillatory behavior (in the scale of ∼10 minutes) is presumed to be related with post-mortem blood movements and/or with gathering and releasing of gases in the abdomen.

3.4.2 Tissue changes on long time-scale (hours – days)

To investigate relatively long-term tissue effects, a 36-hours-long post-mortem ultrasound image sequence was analyzed with a temporal resolution of 5 minutes. Different phases of post-mortem effects were observed in the temporal evolution of raw ultrasound signals and time constants were calculated for each (see Fig. 3.6).

The ultrasound images did not show significant variation for the first 13–19 hours following death. This predominantly static period is in accordance with *rigor mortis* (being an important *post-mortem* effect describing long-term, static muscle contrac-

DOI:10.15774/PPKE.ITK.2020.006

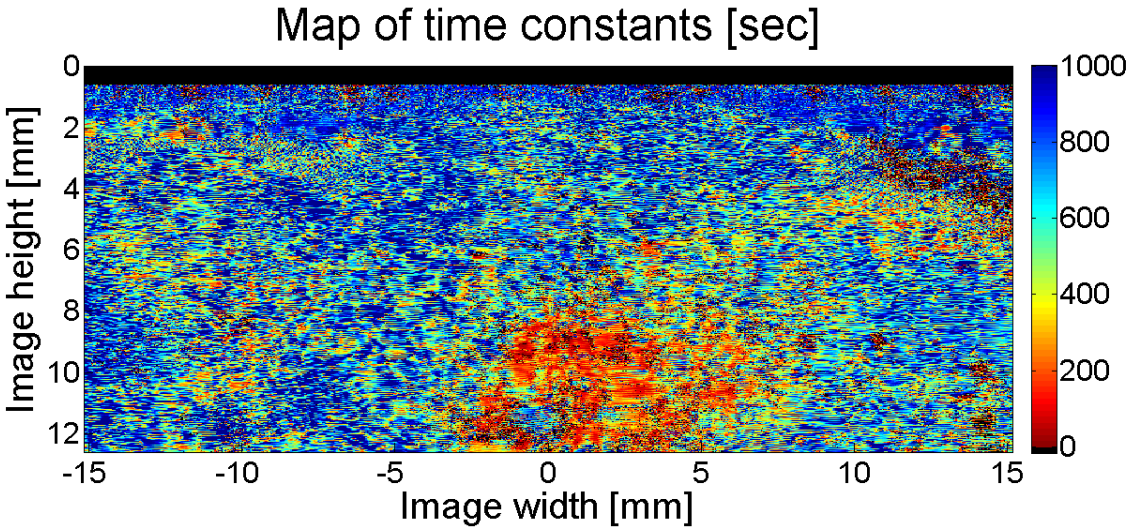

Figure 3.3: Spatial map of time constants calculated from fitted exponential curves. Warmer colors indicate smaller time constants – thus, a faster decay in correlation. On the other hand, colder colors refer to slower decay (with larger time constants) and indicate the places of (more) static scatterers. In order to achieve a better resolution for smaller time constant values, a limit of 1000 s was set for differences to be visualized.

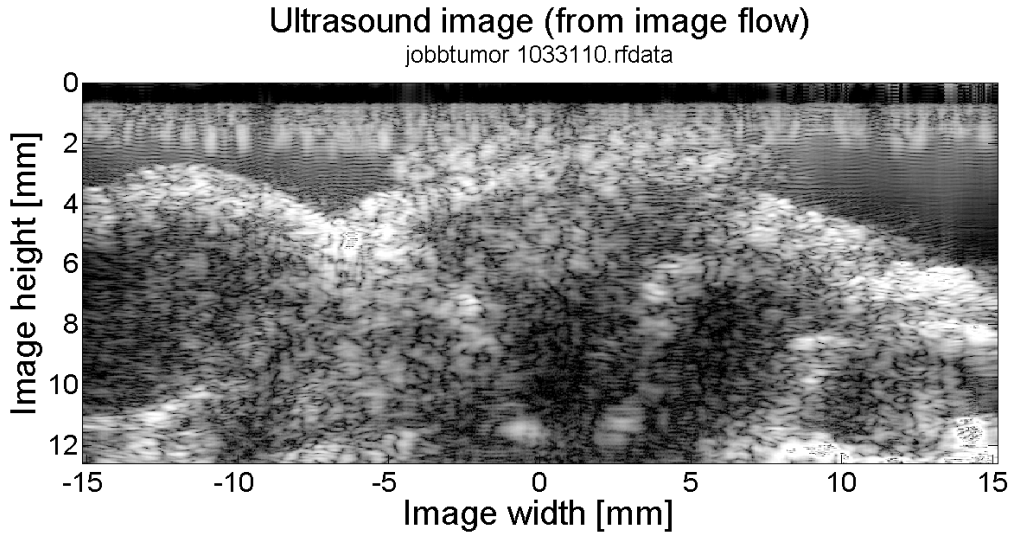

Figure 3.4: A (typical) B-mode (brightness-mode) US image from the image sequence (as reference for Fig. 3.3).

DOI:10.15774/PPKE.ITK.2020.006

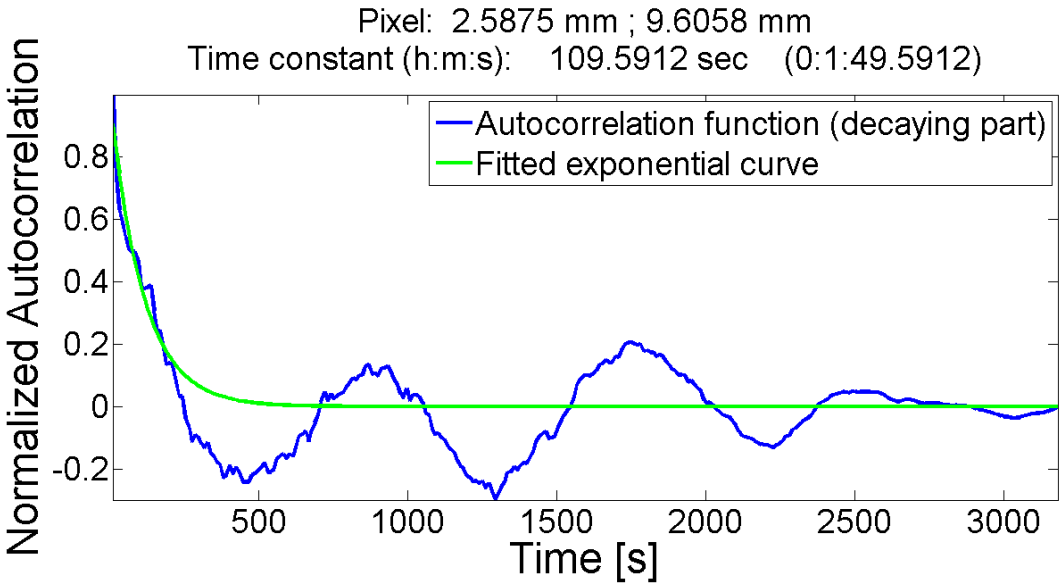

Figure 3.5: Example of the results of decorrelation analysis for pixels imaged in the central ventral region of the mouse. Initially, a nearly exponential decay with a time constant of ∼100 seconds can be observed here, followed by oscillatory behavior with a periodicity in the range of 10–15 minutes.

tion following death, in the absence of ATP (adenosine triphosphate) molecules which would allow actin–myosin complexes to disintegrate [84]).

The generally static phase was followed by a period of dynamical changes hypothesized to be related to decomposition. Here, two phases could be clearly separated. Firstly, relaxation of the corpse (after *rigor mortis* was ended) resulted in relatively quick changes in RF signal amplitudes coming from a given spatial point. A time constant of approximately 250 seconds was calculated for this phase, observed between 19 and 26 hours following death. From observation of the B-mode image sequence, the rapid oscillatory changes in the RF signal in this phase are assumed to arise from large-scale global movement of the mouse as it relaxed following *rigor mortis*, rather than any real oscillatory motion.

In the third phase, slower changes with a time constant of ∼4000 seconds were observed. These changes are hypothesized to be due to advanced decomposition.

DOI:10.15774/PPKE.ITK.2020.006

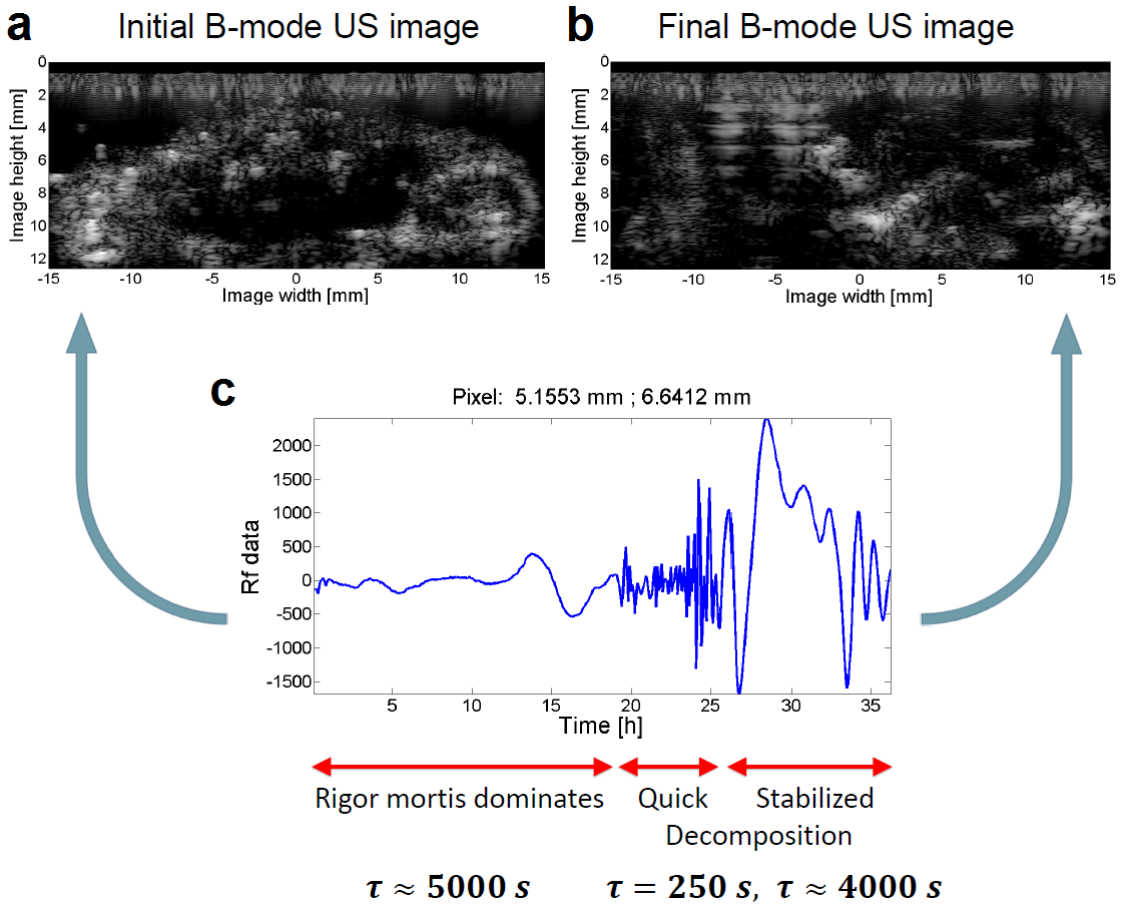

Figure 3.6: Long-term tissue effects.

(a) *First B-mode image from the image sequence (made at the time of death);* ***(b)*** *Final B-mode image from the image sequence (made 36 hours after death);* ***(c)*** *A sequence of temporal RF signal amplitude changes showing typical phases observed, together with calculated time constants for each phase, separately.*

DOI:10.15774/PPKE.ITK.2020.006

3.5 Conclusions

The results showed that dynamic behavior of temporal changes in tissue can be quantitatively characterized by decorrelation analysis on US image sequence. Post-mortem image sequences (exempt from artifacts caused by voluntary motion of the animal) were used to show that DECUS can serve as an effective method of observing changes such as post-mortem tissue effects. Decorrelation analysis method was developed providing a quantitative parameter (time constant of the exponential curve fitted to the initial decaying part of the autocorrelation sequence) for a given spatial location (image pixel). Based on this method, creating a map of the above quantitative parameters has been shown to be a useful tool for visualizing relative dynamicity at several spatial locations in the frame of a temporal image sequence.

Short-term and long-term tissue effects were observed post-mortem (using the proposed method). Nevertheless, further studies are needed elucidating the mechanisms behind these effects as well as further improvements of the methodology. On the one hand, the curve fitting algorithm could be further improved. An interesting question arises discussing whether pixel-wise or global analysis should be performed to give better and more interpretable results (the answer for this question may depend on the given application). A third important direction of improvement points at possibilities for scatterer-tracking. By solving this problem, results of dynamics quantification would be improved by monitoring the dynamics of real parts of the imaged object (or tissue) rather than the dynamic changes of what is seen at certain spatial points on the images.

It is a great advantage of the proposed method that – in contrast with conventional Doppler methods in ultrasound imaging – the proposed DECUS method is independent of the time-course of the changes to be observed (when applying a high enough PRF being higher than the changes to be observed). In this way, potential future applications taking advantage of this feature may be primarily those looking for changes on a long (above seconds) time scale. In the field of biomedical applications, these include the monitoring of long-term biological phenomena such as response to therapy or slow blood perfusion in the capillaries or even the

DOI:10.15774/PPKE.ITK.2020.006

understanding of the post-mortem redistribution of various drugs as mentioned in Section 3.1. Moving towards further applications, a method may be developed in the future for classifying tissue changes based on decorrelation analysis of an ultrasonic image sequence. With resolution improvements of ultrasound imaging, it may also be used in a future application of long-term monitoring of cancer growth or decay as a response to therapy. In the field of echo decorrelation imaging of tumor ablation (see for e.g. [85, 81]), the author is unaware of any calculation of time constants. The use of the current methodology for monitoring tumor ablation may be able to provide a more quantitative evaluation of the decorrelation effect.

Regarding non-medical applications, the presented method is potentially also suitable for measurements of material fatigue via the detection of the appearance of cracks, in the field of non-destructive testing (NDT). This potential industrial application would require a specific framework ensuring that the ultrasound images to be compared are taken of exactly the same area or section of the material, from time to time. The limitations of the method are the followings. The materials to be examined should be transparent for the ultrasound waves. Spatial resolution of the method as well as penetration depth are determined by parameters – primarily by the the center frequency – of the ultrasound imaging system. Finally, objects to be examined should be spatially stable, being exempt from spatial deformations in between time frames of the recordings. With these considerations, the method has a potential in still a wide variety of both biomedical, biological and industrial applications.

DOI:10.15774/PPKE.ITK.2020.006

Chapter 4

Real-Time Data-Based Scanning (rt-DABAS) Using Decorrelation Ultrasound

4.1 Introduction

In ultrasound as in other medical diagnostics, there is a trend towards making portable and cost-effective devices that offer better access to healthcare [13, 86, 87]. A remarkable approach serving the purpose of creating cost-effective and portable ultrasound imaging devices is looking at possibilities and alternatives in scanning. A novel real-time scanning method (rt-DABAS) is proposed here which uses the scanned data itself for scan conversion (putting the relevant data into an image frame). Cost-effectiveness and portability is attained in consequence of the proposed method realizing dimension incrementation of US image signals (obtained with a lower-dimensional – thus, lower-cost – US imager) without the addition of mechanical motion systems or position sensors.

In this chapter, theory of the proposed DABAS method is presented first. This is followed by the presentation of experimental validation of the method. While the present chapter aims to discuss a generalized investigation of different aspects of the method, a specific application has been developed and realized in practice. This is presented in more detail in a separate chapter: Chapter 5.

DOI:10.15774/PPKE.ITK.2020.006

4.1.1 Background

As noticed above, one method of reducing cost in ultrasound imaging is to substitute electronic scanning of the A-lines with physical scanning, either using mechanical scanning with a stepper motor [88] or freehand scanning [89]. Typically, only one transducer element is required for physical scanning, which is especially advantageous for higher frequencies (> 20 MHz), where transducer array manufacture is still relatively complex [90]. Since single-element transducers have poor lateral resolution outside their focal region, an annular array may also be used [60]; this achieves a more uniform lateral focusing with depth while requiring lower transducer and hardware complexity than widely used linear arrays [91].

Regarding mechanical scanning, the presence of the motor and driving circuity increase cost, complexity, and power consumption while reducing reliability [92]. Alternatively, freehand scanning may be used, where estimates of the scan position are necessary. One option is to use some type of location or motion sensor, which could be acoustic [19], magnetic [93, 94], electromagnetic [95, 96], tilt [97, 92, 98, 99, 100], optical, or infrared [101]. However, these sensors usually suffer from some combination of issues including limited position accuracy, latencies in either position sensing or ultrasound data recording, or limitations on the scanning path that can be covered [102]. One commercially successful application, the Signos system [92] relies on an angularly scanned transducer with a tilt sensor. However, for applications involving areas of interest relatively close to the transducer and containing angle-dependent surface reflectors, linear scanning may be more appropriate. One such application is the examination of skin surface lesions [103].

Another potential method of estimating position during freehand scanning involves use of the data to estimate position [19], which is termed here data-based scanning, or DABAS. In the current practice, a calibration curve describing the degree of similarity between two 2-D ultrasound images as a function of their distance allows an estimate of their relative positions. Such estimates from a set of 2-D images are combined to generate a scan-converted 3-D volume. The research team from the SOUND Laboratory, at Pázmány Péter Catholic University, Faculty of Information Technology and Bionics was generalizing this idea to the scan conversion of a set of

DOI:10.15774/PPKE.ITK.2020.006

A-lines into a 2-D image. In such a situation, it becomes a user need to visualize the image in real-time. Therefore, a real-time DABAS algorithm (rt-DABAS) has been developed [4] that accepts A-lines into a predefined image grid as soon as they arrive rather than the classical method of performing offline processing on all the data.

Hereinafter, an overview of classical DABAS methods is followed by a presentation of the proposed rt-DABAS method, including the derivation of the calibration curve, the scan conversion method, and measures of position estimation errors.

4.2 Theory

4.2.1 Overview of existing DABAS methods

As previously mentioned, a method of estimating transducer motion during freehand scanning relies on quantifying the change of the incoming ultrasound data as it is moved and relating this change to transducer displacement using a calibration curve. For generality between the classical problem of converting 2-D images into a 3-D image and the problem of converting 1-D A-lines into a 2-D image, the term data frame will be used to refer to individual A-lines or 2-D images, sets of which need to be aligned in space to perform scan conversion. Before considering the theory and implementation of the proposed method, existing methods of calibration curve estimation and transducer position estimation for scan conversion are briefly considered.

The calibration curve $\rho(d)$ is a function expressing the level of similarity ρ between two data frames whose recording location is a distance d apart. The measure of similarity is usually the Pearson correlation coefficient, so that if fully developed speckle (FDS) can be assumed, then the calibration curve is the lateral autocorrelation of the imaging system point spread function. If the FDS assumption does not hold, more advanced estimation methods may need to be employed, including statistical modeling of speckle formation [104, 23], tissue characterization [25], adaptive models [27, 26], or machine learning [105]. It is unclear, however, how general these methods are to different tissues or transducer types, or indeed how large errors are

DOI:10.15774/PPKE.ITK.2020.006

incurred when assuming FDS for single element transducers. It would be desirable, therefore, to investigate the potential limitations of assuming FDS for single element transducers.

Another issue to consider is the method of scan conversion. Due to the presence of noise, an estimate of the distance between two subsequent data frames based on the estimated calibration curve $\widetilde{\rho}(d)$ is sometimes considered too erroneous. Therefore, current methods combine distance estimates between many pairs of data frames using weighted averages [106, 107, 108, 109]. Again, it is unclear how accurate position estimation is for noisy data from single element transducers, whereas the retrospective combination of distance estimates compromises real-time scan conversion. Therefore, a novel, real-time DABAS algorithm (rt-DABAS) [4] is proposed that displays a data frame in the relevant place as soon as it is recorded.

4.2.2 Calibration curve

Let the calibration curve $\rho(d)$ be defined as the expected correlation coefficient between a reference data frame and a data frame recorded at a distance d from the reference. When FDS is assumed without the presence of imaging noise, $\rho(d)$ is independent of the reference recording location and its extrema are:

$$\rho(0) = 1, \tag{4.1}$$

$$\lim_{d\to\infty} \rho(d) = 0, \tag{4.2}$$

where $\rho(0)$ concerns the correlation coefficient between two data frames recorded at different times but at the same location. This distinction becomes important when additive noise is present, whereupon the first extremum is modified as follows:

$$\rho(0) = \sqrt{\frac{10^{\sigma/20}}{1+10^{\sigma/20}}}, \tag{4.3}$$

where σ is the signal-to-noise ratio (SNR) in dB.

With the addition of noise, the estimation of the calibration curve will be subject to sampling error. Moreover, due to statistical fluctuations, the correlation coefficient ρ between two data frames at distance d will differ from $\rho(d)$ even without the

DOI:10.15774/PPKE.ITK.2020.006

presence of noise. Lastly, when FDS cannot be assumed (conventionally defined as less than 10 scatterers per resolution cell [110]), the autocorrelation of the scattering function will modify $\rho(d)$. The extent of all these phenomena should be assessed using simulations. In addition, two hypotheses concerning $\rho(d)$ should be tested. First, $\rho(d)$ should be closely related to the lateral autocorrelation of the imaging response to a combination of points at several depths. Second, when the calibration curve under noise is normalized to a maximum of 1, the curve should return to its original shape that it had without the addition of noise.

4.2.3 rt-DABAS algorithm

Once an estimate of the calibration curve $\rho(d)$ has been obtained, a scan conversion algorithm may be employed on the incoming data frames $F_1, F_2, ..., F_I$. In conventional DABAS methods [106, 107, 108, 109], the correlation coefficients between all or a subset of the data frames are first calculated; these coefficients are then combined offline to measure the relative positions between subsequent data frames; lastly, the data frames are interpolated onto image frames $I_1, I_2, ..., I_K$ with a regular spacing of Δy between them (Fig. 4.1).

In contrast, the proposed algorithm (described in even more detail in [4]), relies on a high enough frame rate of data frame acquisition to yield the assumption that for each image column, there will be a data frame recorded sufficiently close to the desired location (Fig. 4.2). The real-time algorithm employs an acceptance criterion $\alpha_{i,k}$ that determines whether the current data frame i can be loaded into the current image column k:

$$\alpha_{i,k} = \sum_{j=1}^{J} w(j, J) \left| \rho_{I_{k-j},F_i} - \rho(j\Delta y) \right| < \epsilon, \tag{4.4}$$

where $w(j)$ are a set of weights for a window size J, used for combining the absolute differences between a measured correlation coefficient ρ_{I_{k-j},F_i} and an expected correlation coefficient $\rho(j\Delta y)$. The measured correlation coefficient ρ_{I_{k-j},F_i} is calculated between the current data frame F_i and J past image frames. If the data frame was recorded at the expected location, then the expected correlation coefficient should be $\rho(j\Delta y)$. When the weighted sum of absolute differences is below some predefined

DOI:10.15774/PPKE.ITK.2020.006

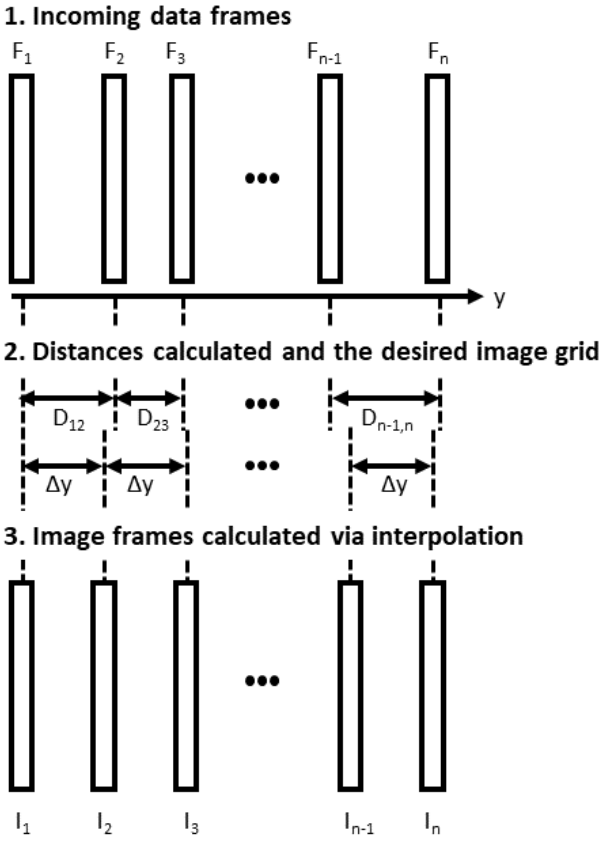

Figure 4.1: Schematic illustrating the concept of conventional DABAS methods. The relative positions between subsequent data frames are calculated offline when having all of the frames and frames of the desired image grid are calculated using interpolation [4].

threshold ϵ, the acceptance criterion is met, the current data frame is loaded into image frame I_k, and k is incremented by 1 in order to search for the data frame that can load the next image frame (see Algorithm 1).

DOI:10.15774/PPKE.ITK.2020.006

Algorithm 1 rt-DABAS

procedure ScanConversion($F, \rho(d), \Delta y, w, \epsilon$)

$I_1 \leftarrow F_1$ ▷ *The first data frame is automatically accepted*

$k \leftarrow 2$ ▷ *Index of the actual image grid to be loaded with incoming data*

$i \leftarrow 2$ ▷ *Index of the actual incoming frame of F*

$N \leftarrow lengthOf(F_1)$ ▷ *Number of axial samples in image frames*

$J \leftarrow lengthOf(w)$ ▷ *Window size (calculated from length of weights)*

while *I is not fully filled* **do**

for $j \leftarrow 1, minimumOf(J, k-1)$ **do**

$\rho_{I_{k-j},F_i} \leftarrow \frac{\sum_{n=1}^{N}(I_{k-j_n}-\overline{I_{k-j}})(F_{i_n}-\overline{F_i})}{\sqrt{\sum_{n=1}^{N}(I_{k-j_n}-\overline{I_{k-j}})^2}\sqrt{\sum_{n=1}^{N}(F_{i_n}-\overline{F_i})^2}}$ ▷ (*Section* 1.4)

$\alpha_{i,k} \leftarrow \sum_{j=1}^{J} w(j,J)\left|\rho_{I_{k-j},F_i} - \rho(j\Delta y)\right|$ ▷ *Acceptance metric*

if $\alpha_{i,k} < \epsilon$ **then**

$I_k \leftarrow F_i$ ▷ *Accepted frame is loaded into the image grid*

$k \leftarrow k+1$ ▷ *Index of the next empty grid in the image*

$i \leftarrow i+1$ ▷ *Index of the next incoming frame*

return I

DOI:10.15774/PPKE.ITK.2020.006

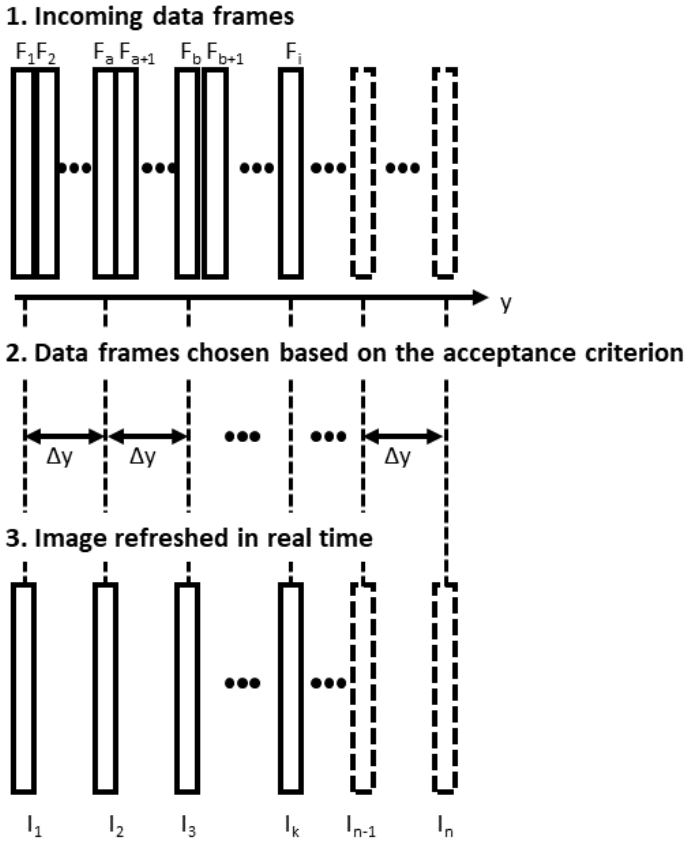

Figure 4.2: Schematic illustrating the concept of the proposed rt-DABAS method. The desired image grid is filled with data frames chosen based on an acceptance criterion, in real time [4].

4.2.4 Position estimation errors

For quantitatively characterizing the performance of the position estimation of the proposed rt-DABAS method, the concepts of *bias error* and *ripple error* are defined as follows.

When loading the data frames recorded at true positions $\overline{y}_t$ into image columns at desired positions $\overline{y}_d$, the difference between the two vectors gives rise to position estimation errors and thus image degradation. A simple scalar measure of error is the root-mean-square error (RMSE) $\|\overline{y}_t - \overline{y}_d\|_2$. However, the error encapsulates two different phenomena that should be differentiated from each other. The first, termed *bias error*, describes the linear increase in error between the true and desired positions as a function of the desired position. This systematic error of position

DOI:10.15774/PPKE.ITK.2020.006

estimation can be quantified by fitting a line to the relationship between $\overline{y}_t$ and $\overline{y}_d$ and is measured in %:

$$e_b = \arg\min_e \|\overline{y}_t - e\overline{y}_d\|_2 \,. \tag{4.5}$$

After removing the overall bias from the estimation, the average position error will be zero. However, from one image column to the next, the A-line may still be selected too early or too late. This fluctuating error is termed the *ripple error* and is defined as the root mean square position error after correcting for bias:

$$e_r = \|\overline{y}_t/e_b - \overline{y}_d\|_2 \,. \tag{4.6}$$

For a clearer understanding of the concepts of *bias* and *ripple* errors, an example for position estimation algorithm output together with desired positions, fitted line

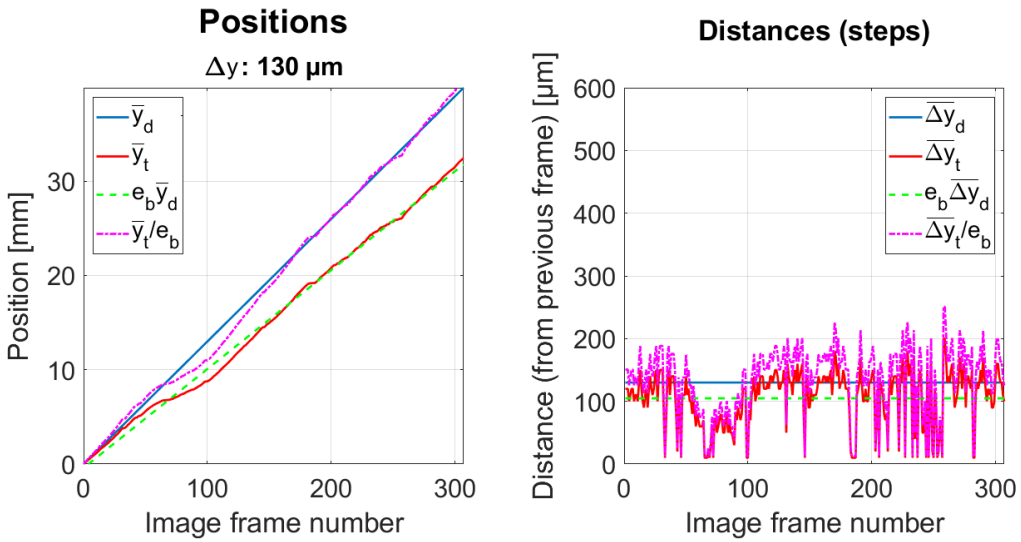

Figure 4.3: Example of position estimation output for showing the concepts of bias *and* ripple *errors. Position estimation output is presented in two forms.* ***Left:*** *Vectors of positions (origo: the first accepted data frame of the image grid).* ***Right:*** *Vectors of step-by-step distances between subsequently accepted data frames of the image grid. True positions $\overline{y}_t$ (and distances) of the accepted data frames are represented in red. The desired positions $\overline{y}_d$ for the image grid step size Δy (input of the algorithm) are displayed in blue. The line $e_b\overline{y}_d$ fitted to the true positions (see Eq.* (4.5)*) is displayed in green. The curves in magenta correspond to the bias-corrected positions $\overline{y}_t/e_b$ (and distances) that were used in Eq.* (4.6)*.*

DOI:10.15774/PPKE.ITK.2020.006

and bias-corrected positions is shown in Fig. 4.3.

4.2.5 Translation speed requirements

One aspect of the algorithm that has not yet received attention is the issue of how fast the transducer can be translated for the algorithm to still function properly. For an image grid step size (Δy), the PRF (pulse repetition frequency) of the ultrasound imaging system should be fast enough that several (n) frames be recorded over a distance Δy to provide adequate sampling (with a lower limit v):

$$v \leq \Delta y/n \cdot PRF. \tag{4.7}$$

As will be seen later (in Section 4.6.3), the choice of Δy will itself depend on the calibration curve.

4.2.6 Axial correction

In real-life practice, freehand scanning is hardly strictly lateral. Axial and tilting vibrations may occur. In order to perform a reliable distance estimation laterally, correction for these vibrations should be performed in advance.

An automated method for axial correction of incoming data frames is presented here, aiming to adjust adjacent data frames axially, prior to scan conversion, in real time. The method is based on correlation calculation and can be performed in two steps, as follows. Step 1: Calculate the cross-correlation function of the last accepted data frame and the actual incoming data frame. Step 2: shift the incoming frame axially due to the shift of the global maximum of the cross-correlation curve from its center.

There are possibilities for the correction for tilting vibrations, also being based on correlation calculation. The differences in correlations of corresponding parts of two adjacent frames imply the differences in the distances of these parts, and from this information, the angle of displacement can be estimated.

DOI:10.15774/PPKE.ITK.2020.006

4.3 Questions arising from rt-DABAS theory

Performance of the proposed rt-DABAS algorithm was evaluated on both simulations, phantom experiments and *in vivo* clinical experiments, as presented hereinafter. The proposed real-time scan conversion algorithm was developed for generating a 2-D ultrasound image from data of a laterally scanned single-element ultrasound transducer. The algorithm employs a fixed calibration curve to update a predefined image grid in real time.

Data of simulations and experiments were used to investigate two basic questions: the accuracy of the calibration curve estimate and the performance of the rt-DABAS algorithm (in terms of position estimation accuracy).

As introduced in Section 4.2.2, it is unclear how general calibration curves are to different tissues or transducer types. Simulational and experimental validation of the method was therefore aimed to investigate particularly if there is a significant dependence of the calibration curve on the FDS assumption of the tissue examined, in the case of a single-element transducer. Stability of the calibration curve for noisy data was also addressed.

Performance of the rt-DABAS method also raises several questions. What estimation errors does the algorithm produce? Is there an optimum image column spacing Δy that minimizes position estimation errors? It is important to note here that, in order to make the investigation of these questions manageable, the presented work restricted itself to a window size of $J = 1$ (see Eq. (4.4)). It should also be noted that, when investigating the feasibility of using the proposed rt-DABAS algorithm for single element transducer imaging, error quantification was done by measuring the bias and ripple errors of the algorithm (as introduced in Section 4.2.4). In this way, performance of the rt-DABAS method was tested using a fixed calibration curve as well as an adaptive calibration curve (as taken from Gee at al. [26]) to see whether the fixed calibration curve can provide a comparable accuracy while ensuring real-time operation.

DOI:10.15774/PPKE.ITK.2020.006

4.4 Structure of the following sections

The following two sections (Section 4.5: "Materials and methods" and Section 4.6: "Results and discussion") follow a structure that may appear as being relatively complicated for a first time reader. The aim was to present the multiple but interconnected threads in parallel and in regularity, while this short section is aiming to prepare the reader for this structure.

The first topic of the structure is about the data used (see Sections 4.5.1 and 4.6.1). This is divided into three categories: simulations, phantom experiment, and *in vivo* human skin experiment (clinical experiment).

The next section in both Section 4.5 and Section 4.6 discusses the calibration curve estimation. Subsections of both Sections 4.5.2 and 4.6.2 follow the investigations of four topics: the relation of the calibration curve to scatterer density, its relation to signal to noise ratio, simplification of the estimation method, and comparison between calibration curves estimated from simulations with those from experiments, consequently.

The third main topic is the position estimation algorithm itself and its performance. Here, there is a slight difference between subsection divisions of Sections 4.5 and 4.6. Section 4.5.3 describes the rt-DABAS position estimation algorithm implementation first. Then, a comparison with a reference method using adaptive calibration curve estimation is introduced in terms of methods. Finally, a separate subsection describes the method for the evaluation of the clinical data. Section 4.6 presents the results of the rt-DABAS position estimation algorithm evaluation together with those of the above comparison of methods described in Section 4.6.3. A separate section – Section 4.6.4 – presents the results on clinical data. There is an additional section – Section 4.6.5 – that discusses further remarks on the feasibility of the rt-DABAS algorithm.

The above structure requires further explanation regarding the presentation of the clinical results. On the one hand, there is less control over clinical data than that over simulations and phantom experiments, therefore this topic should be treated somewhat separately. Meanwhile, on the other hand, the clinical data are used

DOI:10.15774/PPKE.ITK.2020.006

for further validation of the algorithm performance and of the conclusions of the comparison of methods, which explains their presentation in this chapter instead of being in Chapter 5 only. Chapter 5 discusses the same clinical study but with a focus being on its qualitative results and practical outcomes for the specific application field. In contrast, the present chapter focuses on the quantitative results only, to validate the theory of the chapter on the more complex and less predictable real-life data following the validation on controlled simulations and phantom experiments.

4.5 Materials and methods

4.5.1 Ultrasound data recordings

In order to investigate the variability of the calibration curve and accuracy of position estimation during scan conversion, both simulations and phantom experiments were performed. In both cases, a series of A-lines were collected by laterally moving the transducer in 10 μm steps. In addition, clinical experiments were performed to investigate the accuracy of the scan conversion method in real tissue.

Simulations

Simulations were performed using the Field II software [111, 112] with the same transducer geometry and response as used in the experiments. To find the transducer response, backscatter from a planar plexiglass element placed at the focus of the real transducer was recorded. A 4–12 MHz brick-wall filter was applied by transforming the signals into the frequency domain and setting coefficients outside the 4–12 MHz frequency band to zero. Then, an f^3 correction was applied to account for the planar shape of the plexiglass reflector [113, 114]. The resulting excitation signal is shown in Fig. 4.4. Prior to analysis, both experimental and simulated radiofrequency (RF) data were again filtered using the same 4–12 MHz brick-wall filter.

DOI:10.15774/PPKE.ITK.2020.006

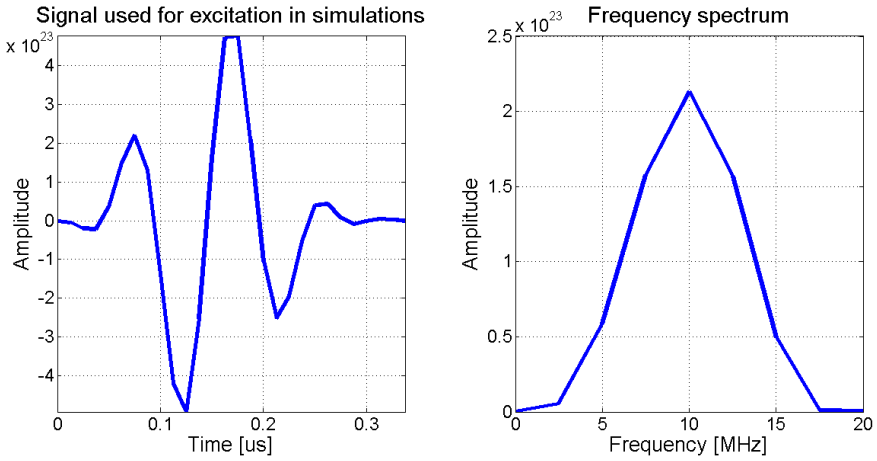

Figure 4.4: Excitation signal used for simulations and its Fourier transform. The signal was obtained from using an Olympus V317 transducer in measurements of backscatter from a planar plexiglass element.

Phantom experiment

The experimental setup consisted of a single element transducer (V317, Olympus, Tokyo, Japan; diameter: 6.3 mm; f#: 3) connected to a pulser-receiver-digitizer (US-KEY, LeCoeur, Chuelles, France) with pulse width setting 5 and transmit voltage 120 V. The pulser-receiver-digitizer was connected to a laptop that stored the received RF data at 80 MHz sampling rate using custom-written software.

It should be mentioned that the central frequency of the Olympus V317 transducer is 20 MHz; however, due to the lower frequency response of the US-KEY device, the overall response of the system in the 4–12 MHz range was around 11 times larger than around 20 MHz. Therefore, to have a signal centered around one frequency and with an acceptable SNR, the filter described above was used – both for simulations and experiments. Since the main conclusions here are independent of the frequencies used, the demonstrated method can be similarly applied for high frequency imaging which was one of the motivations of this work.

Transducer motion was achieved using a precision mechanical motion system (MTS50/M-Z8, Thorlabs, Newton, NJ). Measurements were carried out in a deionized water bath for acoustic coupling (Fig. 4.5).

DOI:10.15774/PPKE.ITK.2020.006

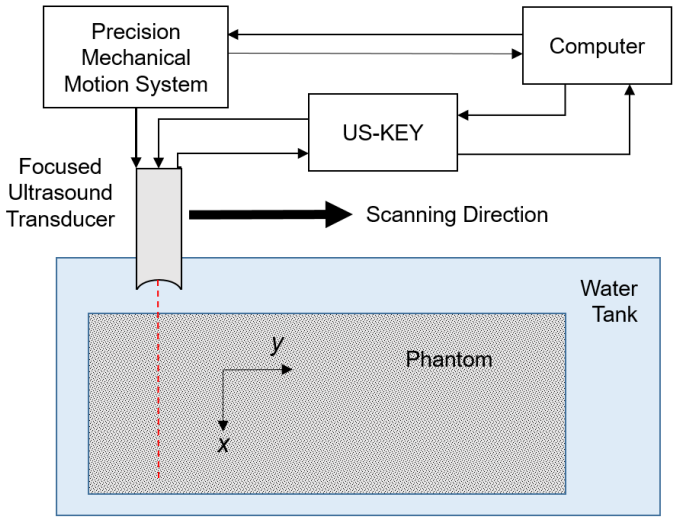

Figure 4.5: Schematic of the experimental setup of phantom experiments. The homogeneous agar-graphite phantom was placed in a deionized water bath and was scanned by the single-element focused ultrasound transducer moved in the lateral direction by the precision mechanical motion system. Pulses for transmission were generated and recorded data were pre-processed and digitized by the "US-KEY" pulser-receiver-digitizer. Further processing and controlling of both the motion system and the pulser were performed using a personal computer.

For the phantom experiment, a homogeneous agar-graphite phantom was prepared. Deionized water was heated to above 80 °Cin a microwave, slowly adding 3% w/w agar, and then 4% w/w graphite to the water while gently stirring, then pouring the mixture into a plexiglass cast and allowing to cool. Upon cooling and removal from the cast, a 25 mm (axial) × 66 mm (lateral) × 45 mm (elevational) phantom was obtained.

Preliminary in vivo human skin experiment

In vivo human skin experiments were performed at the Department of Dermatology, Venereology and Dermatooncology, Semmelweis University. The transducer and pulser-receiver digitizer described in the previous subsection was placed inside a plastic housing and manually scanned over the surface of the skin [5]. The received

DOI:10.15774/PPKE.ITK.2020.006

A-lines were then recorded on a laptop. B-mode images of the same skin lesion were also recorded using a reference commercial ultrasound imager (EUP-L75 connected to Hitachi Preirus, Hitachi, Tokyo, Japan). To ensure accurate comparison, the maximal lateral extent of the lesion was sought to be imaged using both systems. The experiments were carried out as part of an ethically approved study. Hereinafter, the analysis of N=20 lesions is presented.

Prior to lateral scan conversion (based on data-based position estimation), the same 4–12 MHz brick-wall filter was applied on clinical data as in simulations and phantom experiments. To compensate for undesired axial motion during manual scanning, the cross-correlation peak between adjacent lines was used to axially shift each incoming A-line (as described in Section 4.2.6).

4.5.2 Calibration curve

A number of real and simulated ultrasound images were generated, from which calibration curves were obtained in the following manner. First, for each (depth) index, the cross-correlation of each RF line (acting as reference) was calculated in the lateral direction using adjacent RF lines within a lateral range of 600 μm. The mean of these cross-correlation curves was then calculated across all depths and across all reference RF lines.

Calibration curves were simulated to seek answers to the following questions (described in the subsections below).

Scatterer density

To answer the question of how the violation of the FDS assumption affects the calibration curve (Section 4.3), a number of homogeneous phantoms were simulated with different scatterer densities. The scatterer densities were calculated in terms of the resolution cell [115].

DOI:10.15774/PPKE.ITK.2020.006

Signal to noise ratio

In order to investigate the noise-dependence of the calibration curve estimate – and by extension, the robustness of the rt-DABAS algorithm to additive noise – the same Gaussian random noise was added to the RF image data producing various signal-to-noise ratios. To answer the question of whether the addition of noise preserves the shape of the calibration curve (Section 4.2.2), the curve was normalized to have a maximum value of 1 and compared with the noiseless calibration curve.

Calibration curve estimation from point scatterers

If the imager response were depth-invariant, then it would be expected from the Van Cittert-Zernike theorem that the calibration curve obtained from a single scatterer would correspond to that obtained from FDS [116]. However, due to depth-dependence, it is postulated that the placement of several scatterers at depths far enough to avoid interference will approximate the calibration curve of the FDS case (Section 4.2.2). Therefore, images have been simulated from a number of scatterers and compared to see how closely the corresponding calibration curve could approximate the true calibration curve (obtained from FDS).

Comparison of simulation with experiment

To test how well simulations reflect experiments, including the ability to predict the experimental calibration curve, the calibration curve from the simulated FDS image was compared with the calibration curve obtained from the experimental homogeneous phantom.

4.5.3 Scan conversion algorithm and its performance

Algorithm implementation

The rt-DABAS algorithm described in Section 4.2.3 was applied to the simulated and experimental homogeneous phantoms using a comparison window length $J = 1$ and a range of image grid spacings $\Delta y = 10, 20, ..., 600\mu$m. Each grid spacing corresponded to a value of cross-correlation (from the calibration curve) that was

DOI:10.15774/PPKE.ITK.2020.006

used to decide whether the current RF line should be loaded into the image grid. The bias and ripple errors were calculated for each Δy to search for an optimum Δy. The error levels were compared between simulations and experiment.

Comparison with adaptive calibration curve calculation

The accuracy of position estimation with a fixed calibration curve was compared with that of an adaptive calibration curve estimation method from literature [26]. The adaptive algorithm relaxes the FDS assumption by assuming that scatterer coherency is isotropic so that the local lateral coherency can be estimated from the axial autocorrelation, allowing adaptive modification of the calibration curve. The method had been developed and tested for 2-D to 3-D scan conversion and was adapted to the current case of 1-D to 2-D scan conversion in the following manner.

For each incoming A-line, comparison of the current axial autocorrelation with a reference mean axial autocorrelation of the FDS simulation phantom (10 scatterers/resolution cell) yields an estimate of the local scatterer coherency. This estimate is then used to adapt the estimated calibration curve according to the procedure described in [26]. For estimating coherency, axial autocorrelation was calculated for the envelope of data frames. Correlation of coherence was considered four times wider laterally than axially since the resolution cell was approximately four times wider in the lateral direction than in the axial.

It should be noted that apart from the use of an adaptive calibration curve, all other aspects of the implementation followed the proposed rt-DABAS algorithm, rather than the description in [26]. In particular, no angular correction was employed by using several image patches; no median filter was applied; and data frames were accepted into the image columns according to Eq. (4.4).

When performing comparison of the two methods, focus has been put on a range of step sizes where errors were minimal for both algorithms, due to maximal slope of the calibration curve [117, 118]. The aim was to investigate whether the fixed calibration curve could yield comparable accuracies while ensuring a real-time operation.

DOI:10.15774/PPKE.ITK.2020.006

Evaluation of clinical data

Following collection and preprocessing of clinical data (described in the last subsection of Section 4.5.1), lateral scan conversion was performed on the preprocessed set of A-lines. An image grid step size of 305 μm was used, corresponding to a correlation value of 0.5 in the calibration curve. The value was evaluated from the calibration curve of the homogeneous phantom experiment, since it was assumed that the same noise level needed to be corrected for in both cases (Section 4.5.2).

For clinical data of real tissue acquired via freehand manual scanning, the exact positions of A-lines were not known *a priori*, and position errors could therefore not be estimated directly. However, using images made of the same skin lesion by the reference device, spatial dimensions of the lesions (measured manually on the images) could be used as a basis of comparison. It was expected that lesion length errors (calculated in the lateral dimension) would primarily express the inaccuracy of scan conversion, while lesion thickness errors (calculated in the axial direction) could serve as a measure of baseline error (such as arising from inaccuracies in imaging the same maximal diameter 2-D slice of the lesion volume, or the inaccuracy of manual measurements).

DOI:10.15774/PPKE.ITK.2020.006

4.6 Results and discussion

Following the structure of Section 4.5, results are presented in terms of the ultrasound images, the calibration curves, and scan conversion algorithm performance results obtained.

4.6.1 Ultrasound image recordings

Fig. 4.6 shows simulated images of homogeneous phantoms with different scatterer densities of 0.2, 1, 5 and 10 scatterers/resolution cell, with the last case (10 scatterers/resolution cell) considered as FDS [110]). The depth of field can be qualitatively observed as a vertical band of relatively higher intensity speckle. The asymptotic behaviour towards FDS can also be qualitatively observed.

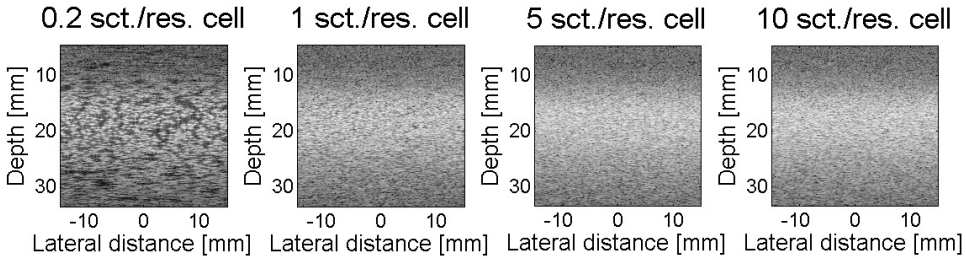

Figure 4.6: Simulated B-mode images (with 60 dB dynamic range) of homogeneous phantoms of 0.2, 1, 5 and 10 scatterers/resolution cell densities, respectively. The simulated imaging system was a single element Olympus V317 transducer moved along the lateral dimension, collecting A-lines with an equal 10 μm spacing.

DOI:10.15774/PPKE.ITK.2020.006

Simulated B-mode images of 1, 11 and 31 scatterers can be observed in Fig. 4.7. These were used to generate calibration curves that potentially approximate the FDS case. The case of 11 scatterers approximately covers the −6 dB depth of field of the transducer. In Fig. 4.8, an image of the experimental agar-graphite phantom can be observed.

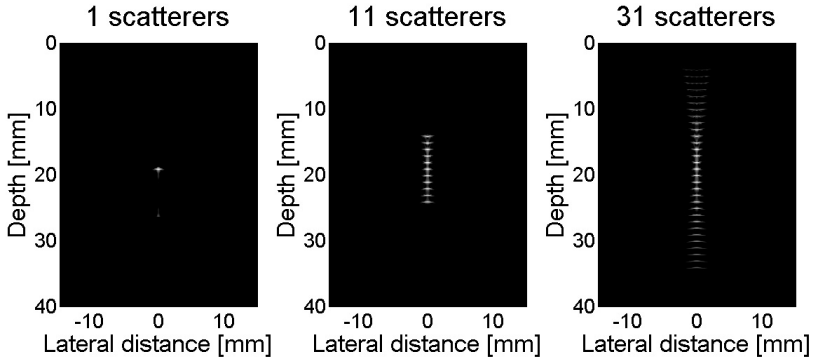

Figure 4.7: Simulated B-mode images (40 dB dynamic range) of 1, 11 and 31 scatterers respectively placed around transducer focus with a uniform axial spacing of 1 mm. The imaging system simulated was the same as for Fig. 4.6.

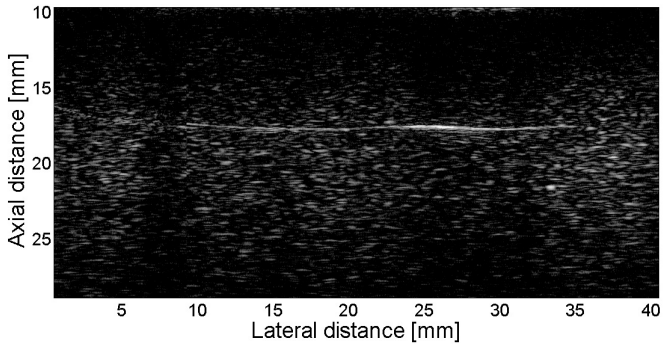

Figure 4.8: B-mode ultrasound image made of a 3% agar – 4% graphite homogeneous phantom by mechanically scanning an Olympus V317 single element transducer (with 19 mm focus). The image consists of 4000 A-lines with 10 µm spacing. The depth range shown here is the range used for later analysis (calculation of the calibration curve and position estimation).

DOI:10.15774/PPKE.ITK.2020.006

4.6.2 Calibration curve

Scatterer density

Calibration curves were calculated for a number of homogeneous phantoms simulated with different scatterer densities.

In order to define scatterer densities in terms of a number of scatterers in the resolution cell, the latter was established by simulating a point scatterer at the focus of the transducer, taking the envelope of the image thus produced, and calculating the area above or equal to 0.5 (or -6 dB) of the peak amplitude. Using this measure, the appropriate number of point scatterers was randomly placed on a 30 mm (axial) $\times$ 35 mm (lateral) 2-D region using a 2-D uniform distribution. Phantoms with different scatterer densities of 0.2, 1, 5 and 10 scatterers/resolution cell were generated, with the last case considered as FDS [110]. The running time of the simulations on a laptop (Intel Core i5 processor, 8 GB RAM) was 10–450 minutes, depending on scatterer density.

Calibration curves calculated for different scatterer densities (0.2, 1, 5, 10 scatterers / resolution cell) were found to be almost identical (Fig. 4.9), with a mean absolute error of 8.3×10^{-3} (in average, for all pairs of the four curves presented).

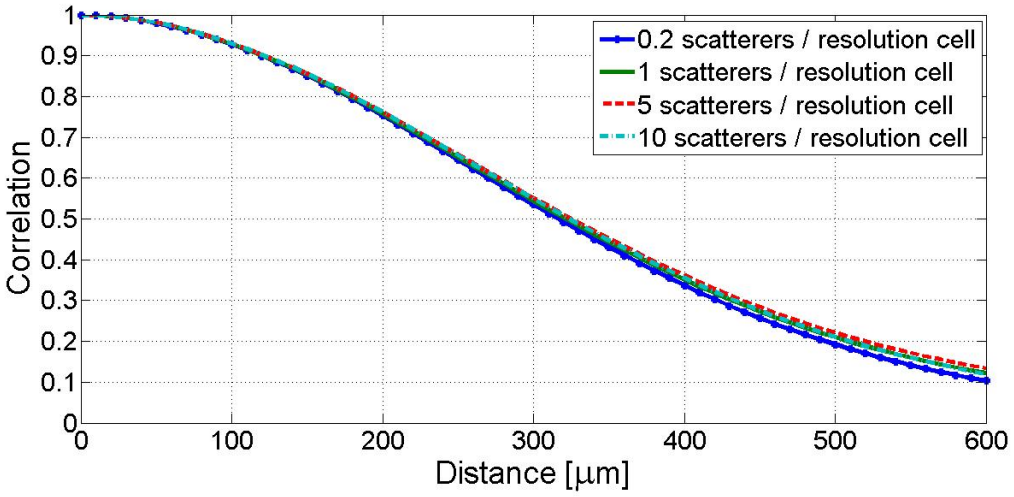

Figure 4.9: Calibration curves calculated from simulated data of homogeneous phantoms with 0.2, 1, 5 and 10 scatterers / resolution cell densities.

DOI:10.15774/PPKE.ITK.2020.006

The results suggest that the rt-DABAS algorithm can use the FDS calibration curve for a wide variety of homogeneous scatterer densities.

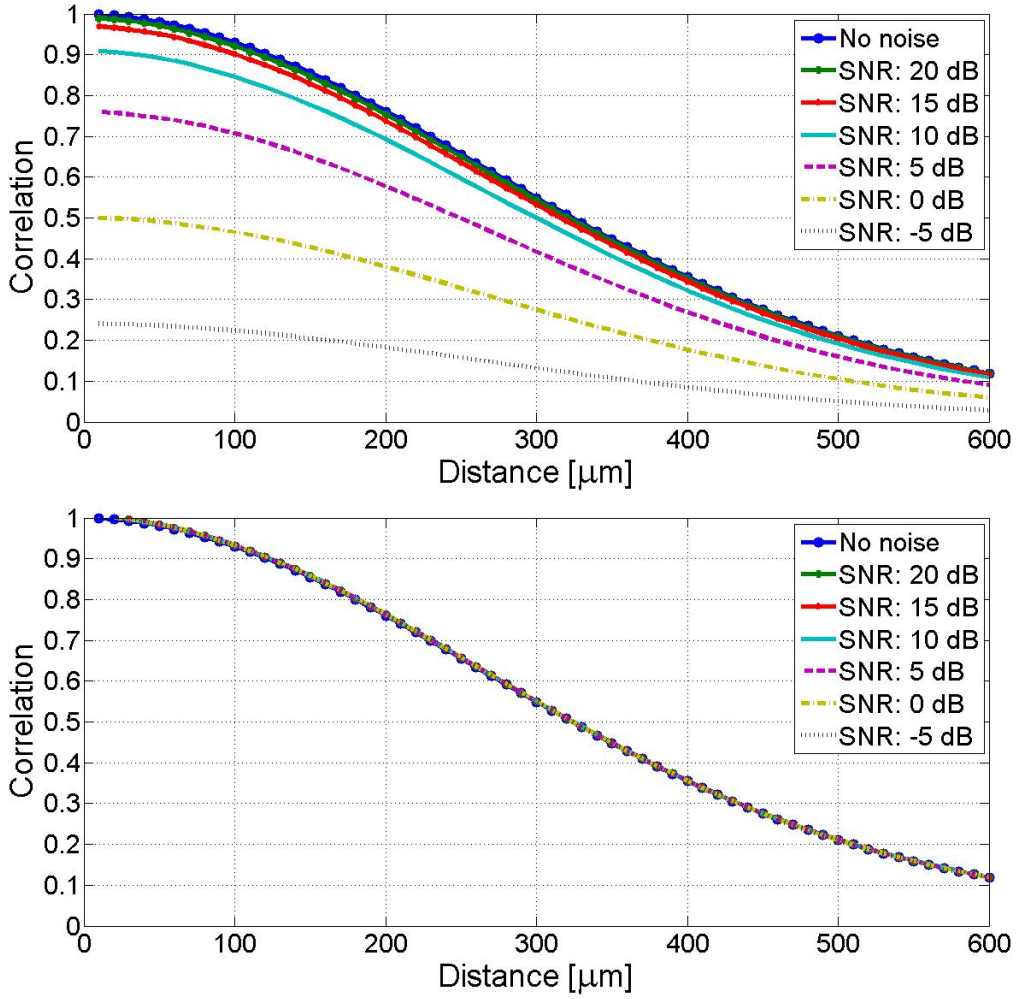

Figure 4.10: Calibration curves calculated from simulated image data of homogeneous phantom (with 10 scatterers / resolution cell density) without noise and with additional (Gaussian random distribution) noise according to 20 dB, 15 dB, 10 dB, 5 dB, 0 dB and −5 dB SNR. ***Top:*** *Calibration curves are presented as calculated (containing also noise level information in initial decay).* ***Bottom:*** *Normalized calibration curves in order to make a visual comparison of the decay rate similarity for the curves.*

DOI:10.15774/PPKE.ITK.2020.006

Signal to noise ratio

Calibration curves calculated from the same image with different levels of additive noise (20, 15, 10, 5, 0 and -5 dB) are presented in the top of Fig. 4.10. The results are shown for 10 scatterers/resolution cell but are representative for other scatterer concentrations as well. The peak correlation values are in agreement with the values expected from Eq. (4.3). Upon normalization to a peak value of 1 (bottom of Fig. 4.10), the correlation curve follows the shape of the noiseless case (with 1.0×10^{-3} mean absolute error between the noiseless-case curve and the normalized curve calculated for the -5 dB SNR case). This suggests that only a minor modification of the noiseless-case calibration curve is needed when running the rt-DABAS algorithm in the presence of noise.

Calibration curve estimation from point scatterers

As introduced in Section 4.5.2, calibration curve approximation from the imaging response for a combination of point scatterers was investigated.

Since the observed amplitude in the image will decrease as the depth of the scatterer moves away from the focus, the question arises as to what depth range the scatterers need to cover to approximate the FDS calibration curve. To this end, 1, 3, ..., 31 scatterers were placed in an axial line around the transducer focus, with 1 mm spacing between them (to avoid interference).

In Fig. 4.11, calibration curves calculated from images of 1, 11 and 31 scatterers (placed as described above and shown in Fig. 4.7) are presented and compared to the one calculated from a (30 mm deep) homogeneous phantom with 10 scatterers/resolution cell concentration, considered to exhibit FDS. As the number of scatterers – and thereby axial range – increases, the calibration curve approaches the FDS calibration curve, with 6.9×10^{-3} mean absolute error between the curves calculated for the 31 scatterers and for the FDS phantom. The results show that the FDS calibration curve can be approximated accurately by placing a relatively small number of scatterers along the transducer axis.

In related work (where 2-D images are extended to 3-D images), the images of

DOI:10.15774/PPKE.ITK.2020.006

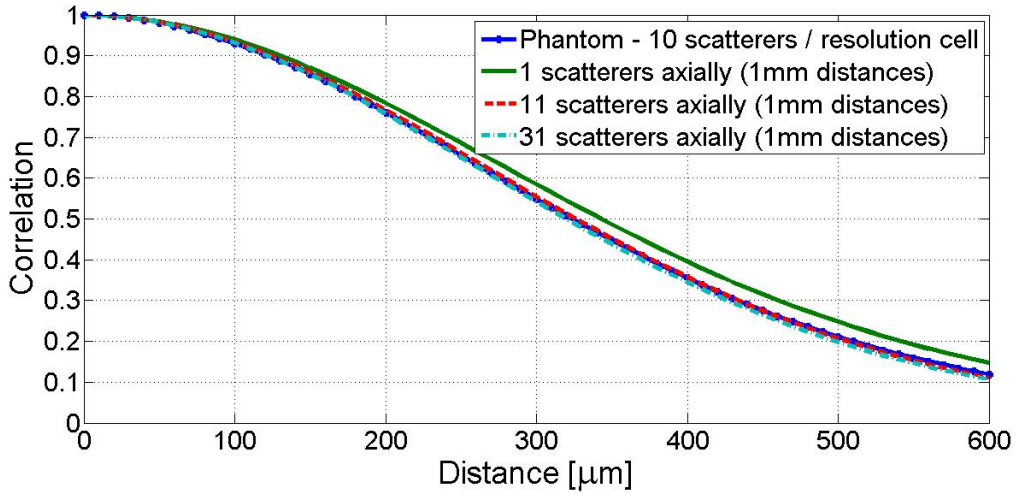

Figure 4.11: Calibration curves calculated from simulated image data of 1, 11 and 31 scatterers placed axially around transducer focus with a uniform 1 mm distance are compared with calibration curve calculated from simulated image of a FDS homogeneous phantom (10 scatterers / resolution cell density) as a reference.

simulated or real phantoms are divided into patches, and the curves are calculated separately for each patch [26, 104, 119]. The patch dimensions are chosen such that there is minimal variation of the calibration curve within the patch. In contrast, the current work shows how an overall FDS calibration curve may be derived for the entire region from a relatively few number of scatterers.

The result of approximating the calibration curve obtained from FDS so closely with the curve obtained from the simple setup of the small number of axially aligned scatterers provides a simplified calibration curve estimation method with two important advantages. On the one hand, a significant improvement of calculation time is offered when estimating the calibration curve from simulations. Calculation time of an ultrasound image is roughly proportional to the number of scatterers simulated in the simulation software Field II. Calculating the FDS image shown on the right in Fig. 4.6, representing 154 740 scatterers took ∼7.5 hours while calculation of the image on the right in Fig. 4.11 with 31 scatterers (using the same imaging system parameters) taking only ∼10 seconds on a PC (HP ProBook 450 G1) with Intel Core i5 processor, 8 GB RAM. On the other hand, for estimating the calibration

DOI:10.15774/PPKE.ITK.2020.006

curve from real measurements with phantoms, the result widens the field of feasible phantom manufacturing techniques. Thus, for example, wire phantoms and 3-D printed phantoms become applicable [120].

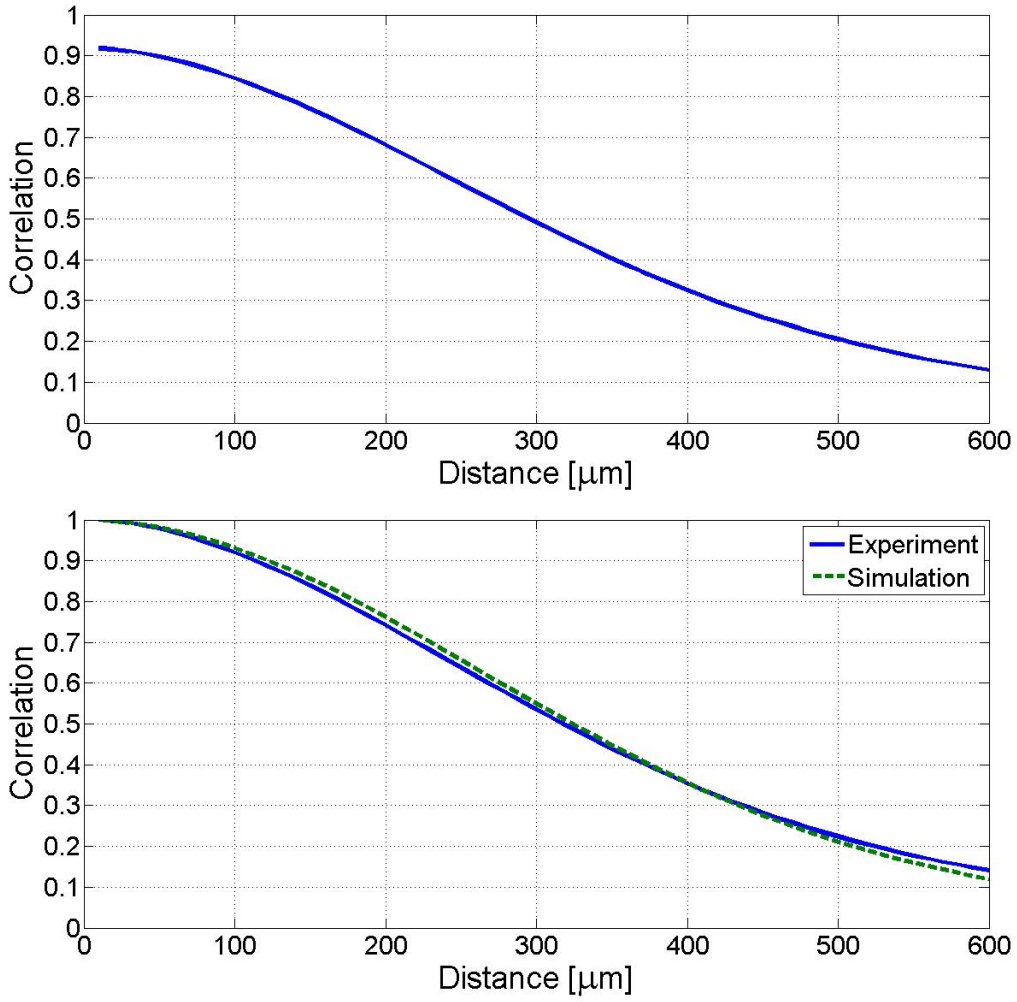

Figure 4.12: Calibration curve from experimental image data. ***Top:*** *Calibration curve calculated from experimental image data (containing noise level information in its initial decay).* ***Bottom:*** *Normalized calibration curve from experimental data compared to calibration curve from simulated data (homogeneous phantom with 10 scatterers / resolution cell density).*

DOI:10.15774/PPKE.ITK.2020.006

Comparison of simulation with experiment

The calibration curve calculated from experimental data is presented in the top of Fig. 4.12. From Eq. (4.3), the SNR is estimated as 10.5 dB. The bottom of Fig. 4.12 shows a comparison of the normalized experimental calibration curve with the FDS calibration curve from simulations. The two curves show strong similarity, with 1.19×10^{-2} mean absolute error, suggesting the potential of accurate calibration curve estimation from knowledge of the transducer geometry and response.

4.6.3 Scan conversion algorithm performance

For the scan conversion on the simulated and phantom data, the calibration curve obtained from the FDS simulation was used; however, in the latter case, the curve was scaled according to Eq. (4.3) to account for the noise level being present.

Fig. 4.13 shows the position estimation errors from using a fixed calibration curve in comparison to the adaptive calibration curve, on the homogeneous phantom with 10 scatterers/resolution cell. The results are representative of other scatterer densities. Using image grid step sizes that correspond to correlation values close to 1 or 0 cause relatively large errors. This result is consistent with previous work [117, 118] and is to be expected because at these values, small changes in correlation values cause large changes in the estimated distance. Interestingly, the bias error is higher for too small image grid steps, whereas the ripple error is higher for too large image grid steps. Overall, a fairly wide range of image grid step sizes (150–350 μm) can be used to obtain relatively low errors for both bias and ripple, in the cases of both algorithms. The ranges of absolute errors in this range of image grid step sizes are shown in Table 4.1. As mentioned in Section 4.5.3, the comparison was focused to this range since the aim was only to show that the proposed real-time method has an acceptable performance in a reasonable application range (of step sizes) as compared to the current literature. As Table 4.1 shows, the errors are considered acceptable for scan conversion.

Fig. 4.14 shows corresponding results for experimental data, with Table 4.2 presenting the extrema of absolute errors in the aforementioned 150–350 μm range

DOI:10.15774/PPKE.ITK.2020.006

of image grid step sizes. These errors are around an order of magnitude higher than those in simulations. Since noise in the image creates noise in the correlation values, this is expected to degrade position accuracy, which could be improved in future work by using a larger comparison window size J (Eq. (4.4)), which would incorporate more correlation values in the algorithm.

Overall, the scan conversion algorithms performed well in the 150–350 μm step size region both for simulations and experiments, with accuracy progressively degrading outside of this region. As mentioned earlier, this is to be expected since accuracy is improved where the corresponding calibration curve has a high slope. However, it is not clear why – for both algorithms – the ripple error in the experimental data shows a strong peak at lower (50–100 μm) step sizes (Fig. 4.14). Further work using simulations could potentially uncover responsible mechanisms, including the role of local inhomogeneities. Nevertheless, since the phantom experiment confirms that within the high-slope region of the calibration curve, acceptable errors are obtained, the next validation using clinical data uses a step size from this region.

Summarizing the comparison of scan conversion algorithm performances, position estimation errors were similar for the two methods, with 92.94% overlap of error ranges in average for bias and ripple errors in simulations, and 42.83% overlap of error ranges in experiments (as an average of 62.28% overlap for ripple errors and 23.39% overlap for absolute bias errors). As it can be seen in Tables 4.1 and 4.2, the use of a fixed calibration curve was leading to slightly higher absolute bias but lower ripple errors. Nevertheless, the main improvement of the former is in its running time. Use of a fixed calibration curve gave a 350 times improvement in running time compared to using an adaptive calibration curve, with the former generating an image from 1000 A-lines in 345$\pm$132 ms (using MATLAB on a computer with Intel Core i5 processor, 8 GB RAM).

DOI:10.15774/PPKE.ITK.2020.006

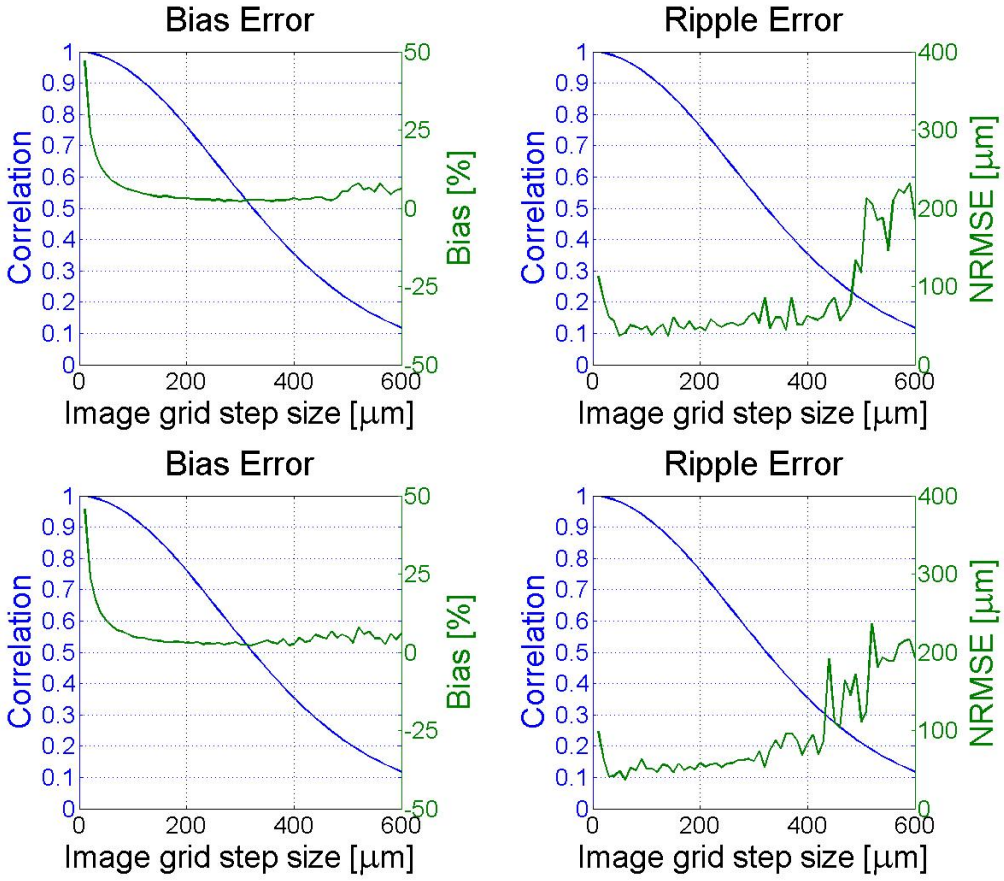

Figure 4.13: Position estimation errors (in green) for simulated data of a homogeneous phantom with FDS (10 scatterers/resolution cell) using fixed ***(top)*** *and adaptive* ***(bottom)*** *calibration curves. Cumulative errors (bias)* ***(left)*** *and ripple errors* ***(right)*** *are presented for different step sizes (distances) of position estimation. The corresponding correlation values of the fixed calibration curve (obtained from the same phantom) are shown in blue.*

DOI:10.15774/PPKE.ITK.2020.006

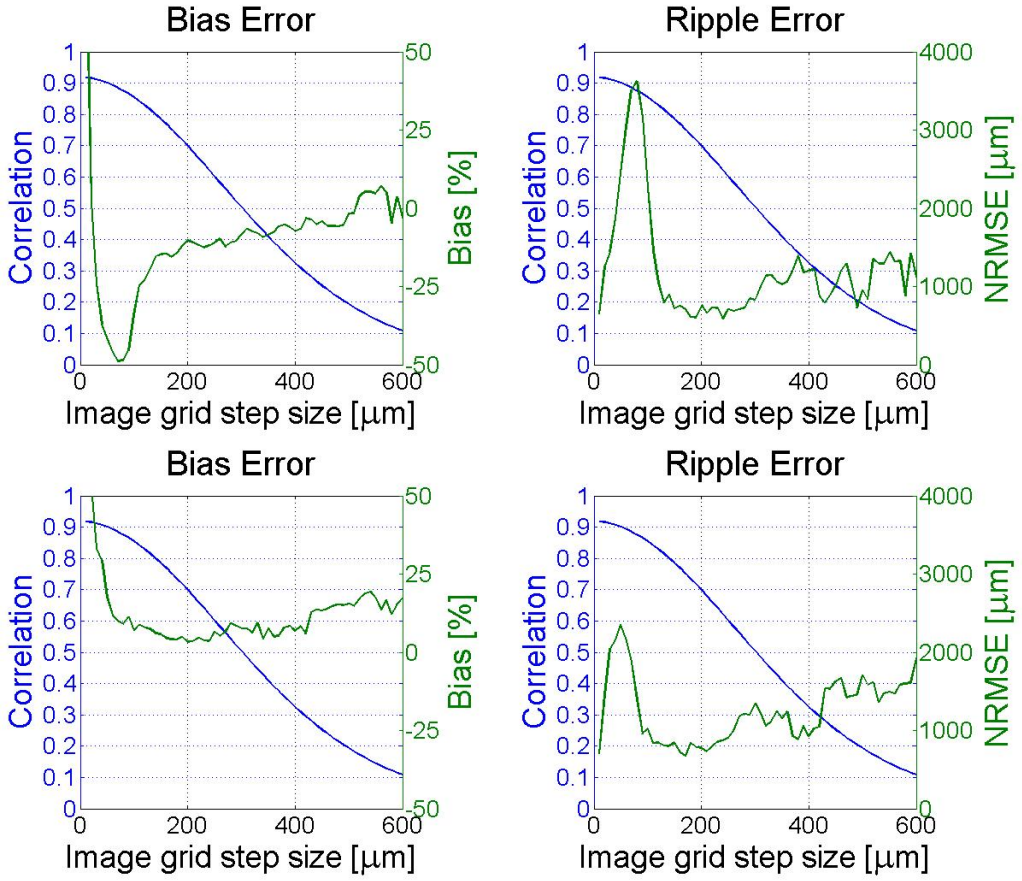

Figure 4.14: Position estimation errors (in green) for experimental data of a homogeneous agar-graphite phantom using fixed ***(top)*** *and adaptive* ***(bottom)*** *calibration curves. Cumulative errors (bias)* ***(left)*** *and ripple errors* ***(right)*** *are presented for different step sizes (distances) of position estimation. The corresponding correlation values of the fixed calibration curve (a version of the simulated phantom calibration curve, corrected for noise – see Section 4.5.2) are shown in blue.*

DOI:10.15774/PPKE.ITK.2020.006

Position Estimation Errors for the Fixed and Adaptive Calibration Curves – Simulations		
Type of Error	Absolute Bias Error [%]	Ripple Error [μm]
Fixed Calibration Curve	2.1 – 3.9	43.8 – 85.5
Adaptive Calibration Curve	2.1 – 3.8	46.0 – 87.0

Table 4.1: Ranges of position estimation errors within the 150–350 μm range of image grid step sizes for a simulated FDS phantom using fixed and adaptive calibration curves. A plot of the errors as a function of image grid step size is shown in Fig. 4.13.

Position Estimation Errors for the Fixed and Adaptive Calibration Curves – Experiments		
Type of Error	Absolute Bias Error [%]	Ripple Error [μm]
Fixed Calibration Curve	6.5 – 15.7	589.5 – 1143.0
Adaptive Calibration Curve	3.3 – 9.4	674.3 – 1342.1

Table 4.2: Ranges of position estimation errors within the 150–350 μm range of image grid step sizes for the agar-graphite phantom experiment using fixed and adaptive calibration curves. A plot of the errors as a function of image grid step size is shown in Fig. 4.14.

DOI:10.15774/PPKE.ITK.2020.006

4.6.4 Preliminary in vivo human skin experiment

The 20 recorded lesions had 0.7–5.5 mm thickness and 3.1–14.6 mm length. Fig. 4.15 shows a representative comparison of a human skin lesion image taken with the reference commercial ultrasound imager, and the image obtained with moving a single element transducer by free hand using the proposed scan conversion algorithm. As shown on the right image (which depicts the selection of A-lines from the incoming stream of A-lines) the algorithm could handle a range of scanning speeds. Qualitatively, both sets of images appeared to show the same morphology, as can be seen by a representative set of images in Fig. 4.15. For a quantitative judgment of the performance, Table 4.3 shows a summary of length and thickness errors, regarding measured lesion dimensions for all 20 cases, with measurements from the reference device images used as reference. The proposed scan conversion algorithm using a fixed calibration curve performed no worse than the adaptive calibration curve implementation, and its accuracy was close to the thickness measurement errors. The mean error obtained in these non-homogeneous tissues was similar to the bias error obtained in the phantom image. The results suggest that using the FDS calibration curve on the proposed algorithm generates clinically interpretable images with reasonable position accuracy.

Human Skin Lesion Dimension Measurements		
Type of Error	Mean Error [%]	Standard Deviation [%]
Lesion Length (Fixed Calibration Curve)	10.8	8.6
Lesion Length (Adaptive Calibration Curve)	13.2	8.8
Lesion Thickness	8.6	6.7

Table 4.3: Scan conversion algorithm performance for in vivo *(human skin tissue) data based on 20 lesion dimensions with reference dimensions obtained from images obtained using the reference commercial ultrasound device.*

DOI:10.15774/PPKE.ITK.2020.006

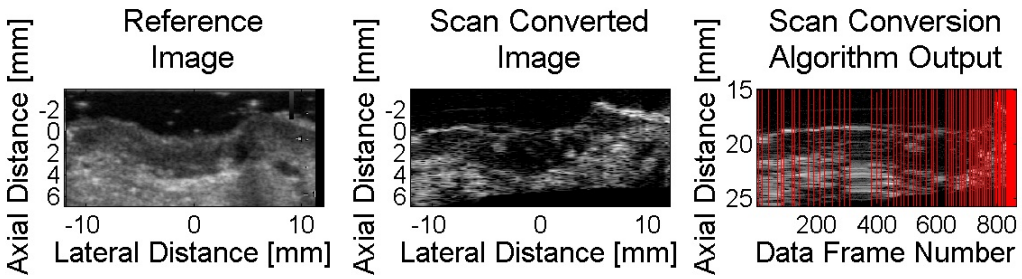

Figure 4.15: In vivo *ultrasound images of a melanoma on a human sole.* ***Left:*** *Ultrasound image obtained with a commercial imaging device using a linear array transducer (Section 4.5.1) as reference.* ***Middle:*** *Ultrasound image of the same lesion obtained with a single element transducer using the proposed scan conversion algorithm.* ***Right:*** *Set of A-lines (scanned by the single element transducer) after axial shift correction but prior to (lateral) scan conversion. Red lines depict A-lines that were selected for scan conversion (see image in the middle).*

4.6.5 Remarks on the feasibility of the proposed rt-DABAS method

The results were presented for a specific case, however they can be easily generalized for transducers with different frequencies and pulse parameters. For the specific case presented here, axial image resolution was 135 μm and lateral resolution was 550 μm in the focal region of the transducer. As concluded from Section 4.6.3, optimal performance of the proposed scan conversion algorithm can be achieved by using an image grid step size being close to this value.

The speed limit of the transducer movement – as seen in Section 4.2.5 – can be derived from the image grid step size and from the PRF. For the US-KEY, the effective PRF taking into account data transfer rate was 67 Hz. In the case of the clinical experiments presented in this work, the speed of lateral scanning was 2.27 ± 0.57 mm/s. This means that on average, an oversampling of $n = 8.85$ (Eq. (4.7)) was achieved.

When talking about the feasibility of a freehand imaging method, another issue to consider beside spatial and temporal resolution (and, in connection, transducer

DOI:10.15774/PPKE.ITK.2020.006

movement speed requirements) is transducer movement requirements in terms of stability of orientation. Instabilities in transducer orientation during freehand scanning can be divided into two groups: axial vibrations and tilting vibrations.

A simple, real-time, correlation-based method has been developed to compensate for axial vibrations during freehand frame acquisition (see Section 4.2.6). This compensation was successfully applied on clinical data where axial correction was performed on raw data prior to application of the lateral scan conversion algorithm. The RMSE of the corrected axial movements was 1.32 mm in average for the 20 recorded lesion cases presented (see Fig. 4.16).

Tilting vibrations (or angle distortions) were not investigated in particular, however, it was found that – for the clinical experiments presented in Section 4.6.4 which may have included some tilting motion – results do not suggest its extent to

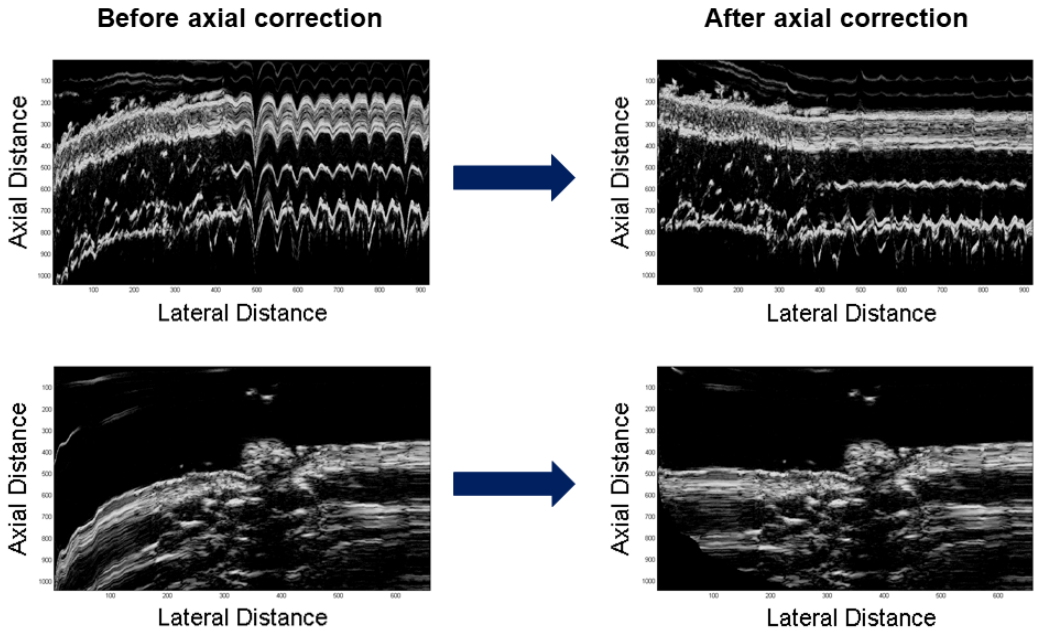

Figure 4.16: Examples showing the performance of the preprocessing method developed for automated axial correction of data frame sequences (Section 4.2.6). Ultrasound image frame sequences of human skin – obtained by the device described in Section 4.5.1 and in Chapter 5 – are shown before ***(left)*** *and after* ***(right)*** *the axial correction being applied.*

DOI:10.15774/PPKE.ITK.2020.006

be significant. This is partially due to the design of the imaging hardware which was shaped in a way to minimize tilting vibrations during movement of the transducer.

4.7 Conclusions

A novel real-time algorithm was presented in this article for data-based scan conversion of A-lines obtained from a laterally scanned ultrasound transducer. The algorithm depends on the calculation of a calibration curve that describes the level of decorrelation between data as the transducer moves away from its original position. Simulations showed that there is negligible difference in the calibration curve for different scatterer concentrations (0.2–10 scatterers/resolution cell). Additive Gaussian noise (−5–20 dB SNR) lowered the peak correlation value as expected, however on normalization, the calibration curve retained the noiseless shape. The placement of a relatively few (31) scatterers on a 30 mm axial line around the transducer focus also estimated the curve with high accuracy. Furthermore, good agreement was found between the calibration curves obtained from simulated and experimental data.

When running the scan conversion algorithm (Section 4.2.3) using the calibration curves with a window size of 1, reasonable performance was achieved for simulations, with bias and ripple errors not exceeding 3.9% or 85.5 μm, respectively for a wide range of image step sizes (150–350 μm, where the calibration curve had a high slope). Worse performance was obtained with experimental data ($< 15.4\%$ absolute bias and < 1143.0 μm ripple over the same range of image step sizes), suggesting the need for investigating the use of larger ($J > 1$) comparison window sizes in the algorithm.

Clinical data of *in vivo* human skin lesions showed the feasibility of the proposed scan conversion algorithm for real, non-homogeneous tissue.

Using a fixed calibration curve compared to an adaptive calibration curve estimation gave similar errors for all investigated cases (simulations, phantom experiments and clinical data), while the former method ran about 350 times faster than the latter.

DOI:10.15774/PPKE.ITK.2020.006

Although simulations and the phantom experiment did not include tilting motion, freehand scanning of tissue may have included some tilting motion; however, results did not suggest its extent to be significant.

Another issue to consider is the acquisition frame-rate necessary for adequate lateral sampling. For dermatological applications, scan times as long as 1 s are routine [103]. Manually scanning a 20 mm wide lesion over such a duration is deemed feasible; using a step size $\Delta y = 305$ μm and $n = 10$ oversampling requires a PRF of 667 Hz according to Eq. (4.7), which is an acceptable value for the ultrasound electronics. In the present case, a PRF of 67 Hz was available, which could still be used with a relatively slower scanning speed of around 2 mm/s, providing an oversampling of $n = 8.85$ (see Section 4.6.5).

Overall, the current work has demonstrated the feasibility of using a real-time scan conversion algorithm for generating 2-D diagnostic images using a laterally scanned single-element ultrasound transducer. The method proposed here can be useful in ultrasound imaging applications in which cost-effectiveness is an important aspect such as high frequency applications where array transducer fabrication is particularly expensive; and where, additionally, linear scanning is preferred to angular scanning. An example of such an application is point-of-care skin imaging. The current results show that the presented methods can be used reliably in such an application.

DOI:10.15774/PPKE.ITK.2020.006

Chapter 5

Clinical Application of the rt-DABAS Method

5.1 Introduction

It was concluded from Section 1.5 that skin tumors present one of the most common cancers in the developed world. It was also concluded that early differential diagnosis of certain types of skin cancer is critical, and that ultrasound images are able to offer valuable additional information to standard dermatoscopic images about the type of skin lesion, non-invasively.

It was shown in Section 4.6.4 that the scanning method proposed in Chapter 4 is applicable for ultrasonic examination of the skin and is able to reduce the cost of this type of examination significantly – given that skin examination requires high-frequency ultrasound ($\sim 10^7$ Hz) transducer which are relatively expensive, thus reducing the number of transducer elements used is of significant financial advantage.

There are several fields in which the rt-DABAS method proposed in this thesis can be applied. In this chapter, a specific application of clinical skin examination is presented in more detail. The demand and vision for a portable cost-effective ultrasound scanner for skin imaging is presented briefly. In response, the clinical investigational prototype device – already mentioned in Section 4.5.1 – is described here in more detail, as well as the outcomes of the clinical investigation performed with ethical grant for the examination of skin lesions.

DOI:10.15774/PPKE.ITK.2020.006

5.2 Background – demand and vision

5.2.1 Challenges in skin cancer care

The high incidence of skin cancer cases (see Section 1.5.2) is a burden on cancer care, but most importantly on the screening continuity. Early diagnosis and following treatment is crucial for people with malignant skin lesions, as emphasized in Section 1.5. It was also noted in Section 1.5.5 that ultrasound examination provides a significantly more accurate diagnosis for skin lesions than conventional optical examination using dermatoscopy (Section 1.5.4). Using appropriate transducer and pulse parameters (such as $\sim 10^7$ Hz high frequency) provides suitable resolution and sufficient penetration depth for skin examination, overcoming the limitations and disadvantages of alternative imaging techniques collecting information in all three spatial dimensions of the skin (Section 1.5.4).

In practice, however, high-frequency US devices used for the observation of skin lesions are currently expensive and their images are difficult to interpret for non-radiologist users. As a result, such a device is usually used by a dedicated radiologist in a larger dermatological center. It is beneficial for skin cancer patients to be referred directly to a dermatological center, however, these institutes are typically overloaded. In many cases (of the patients visiting these institutes), the diagnosis of the skin lesion turns out not to be severe. On the other hand, unfortunately, some with an urgent need do not get to the proper clinic in consequence of the overload.

To overcome this issue, a portable, cost-effective device dedicated to skin examination with easy-to-interpret ultrasound images would be a useful, beneficial tool in wide-spread pre-screening of skin lesions being suspicious for some type of cancer. (Cost-effectiveness and portability could enable its wide-spread use, with easy-to-interpret image rendering diminishing or eliminating the need for a dedicated radiologist.) Wide-spread pre-screening of skin lesions – with the additional information that ultrasound can provide for their classification – would enhance the accuracy and continuity of skin cancer screening meanwhile taking overload off from clinics and would forward patients with severe cases to the competent clinics, at the same time.

DOI:10.15774/PPKE.ITK.2020.006

Another important field of application for such a portable skin-scanner device would be treatment planning. Three relevant challenges are identified and addressed in this field.

In the current practice, the surgical removal of melanomas is done with a well-defined margin for safety [121]. The cases of basaliomas (BCC) are different, however. As introduced in Section 1.5.3, these lesions are very common and tend to appear in aesthetically sensitive locations of the body (such as the face, nose or ears). Basaliomas are well demarcated in the skin and rarely metastasize or recrudesce after surgical removal. Therefore, planning of their excision with a device that is being able to provide in-depth images of the skin and of the lesion, would facilitate treating as much and only as much as is necessary (i.e. preventing recrudescence and minimizing the aesthetic impact of the treatment, at the same time).

Another benefit arises in the practice of biopsy. Incisional biopsy samples are ideally acquired from a region in which the lesion has its largest thickness [122, 123]. The spot for biopsy is currently usually located via palpation. The proposed cost-effective, portable ultrasound device would be useful in locating the proper spot more accurately and reliably (based on the quantitative thickness information of parts of lesions on the images).

A third challenge which can be addressed by the proposed device is treatment planning in general – or treatment designation. The primary treatment of cancerous skin lesions is surgical excision currently (as mentioned in Section 1.5.2). Alternatives – such as cryotherapy [124], electrocautery [125] or photodynamic (laser) therapies [122] – exist, however, the choice between these therapies or that of surgical removal can depend on the thickness of the lesion to be treated. Therefore, the proposed device has the potential of assisting the designation of the type of treatment, as a third area of use in addition to the above two challenges.

5.2.2 Substantiation of clinical relevancy

The Department of Dermatology, Venereology and Dermatooncology, of Semmelweis University and the Faculty of Information Technology and Bionics, of Pázmány Péter Catholic University have been working together for several years on the role

DOI:10.15774/PPKE.ITK.2020.006

of US dermatology and histological findings. Results showed that there is a significant relationship between histology and ultrasound imaging [126] and that certain morphologies observed on ultrasound images of skin lesions are strongly correlated with malignancy [127]. However, in order to make extensive use of these results, it is necessary to use a cost-effective, portable device such as the one applying the rt-DABAS method proposed in this thesis for imaging, which is described in more detail hereinafter.

5.3 Materials and methods

5.3.1 Hardware implementation

A single-element, portable ultrasound research prototype device has been developed for the specific use of skin imaging at the Pázmány Péter Catholic University, Faculty of Information Technology and Bionics (Budapest, Hungary), as already mentioned in Section 4.5.1. The device was built of commercially available components with a custom-designed plastic case cover, which has been designed to realize manual scanning without damaging the skin and with minimal usage of gel.

Components of the device are shown in Fig. 5.1. A single-element, spherically focused ultrasound transducer (V317, Olympus, Tokyo, Japan; diameter: 6.3 mm; f#: 3) was used with 20 MHz central frequency and a fixed 19 mm focus (Section 4.5.1). The transducer was connected to an ultrasound pulser-receiver and digitizer (US-KEY, LeCoeur, Chuelles, France) via SMA–BNC and BNC–UHF adapters. This setup was put inside a custom 3-D printed case made of PLA (polylactic acid, a plastic that is harmless to the skin), with properly designed vents (to prevent the circuit from overheating). The waterproof enclosure surrounding the transducer was designed with a removable cap around the transducer head to facilitate cleaning and disinfection. The cap included a pair of rounded plastic rails to facilitate straight linear and non-injurious movement of the device on the skin surface (during manual scanning) and a cavity for holding gel for acoustic coupling (required for ultrasound imaging) between the transducer and the skin surface. The cap was designed also for maintaining a fixed distance (the focal distance) between the examined surface and

DOI:10.15774/PPKE.ITK.2020.006

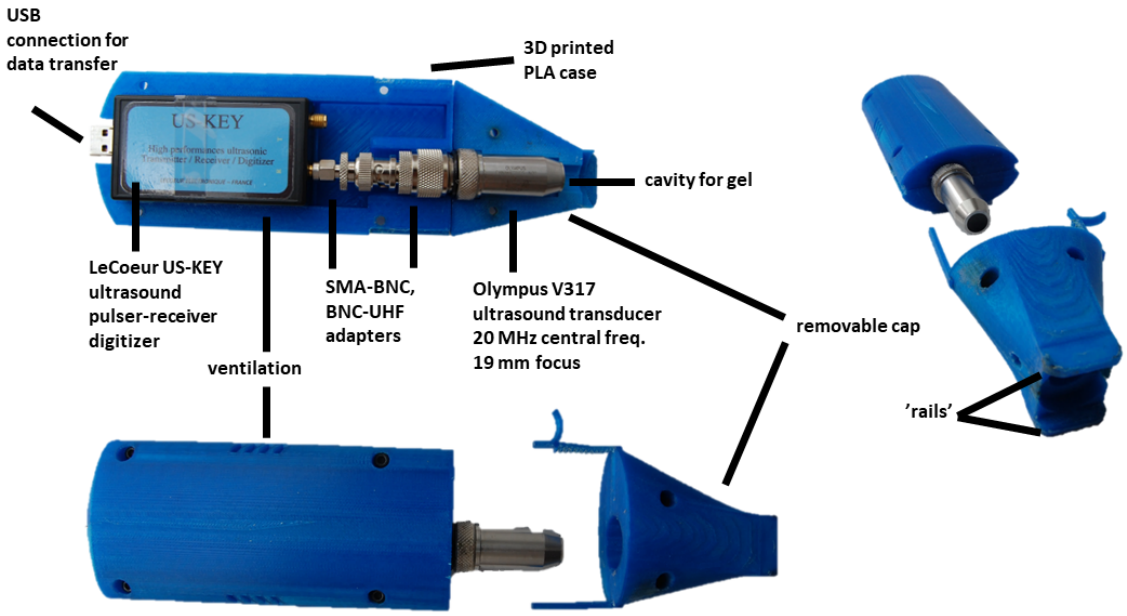

Figure 5.1: Components of the portable, cost-effective skin imaging ultrasound device prototype.

the transducer head, and to minimize possible tilting vibrations during movement of the transducer.

The pulser-receiver of the portable device was connected to a PC (laptop) via USB cable. A custom software running on the laptop made it possible to set ultrasound imaging parameters, to start and stop recording, to display acquired data in real time and to store the recorded data (optionally).

As for imaging parameters settings (likewise in Section 4.5.1), A-lines were collected using pulses with 120 V transmit voltage and 500 Hz PRF. The received A-lines were digitized using 80 MHz sampling rate and a gain of 60 dB. Digitized RF data frames (raw A-lines) were forwarded sequentially to the PC (via the USB cable) and were used as input for the rt-DABAS data-based scan conversion algorithm.

Preliminary measurements have shown that both the mechanical and thermal effects (Section 1.3) of ultrasonic waves in the above-described assembly were significantly lower than the limits specified by the relevant regulations. (Worst-case

DOI:10.15774/PPKE.ITK.2020.006

estimates – based on hydrophone measurements – were 0.87 and 0.45 for MI and TI respectively, in the focus of the transducer, being well below the corresponding limits of 1.9 and 6 [128].)

5.3.2 Reference ultrasound imaging (USI) device

When investigating the performance of the portable skin imaging device, a commercial ultrasound imaging device, EUP-L75 linear array transducer of 18 MHz central frequency connected to a Hitachi Preirus USI device (Hitachi, Tokyo, Japan) was used as a reference.

5.3.3 Participating patients of the clinical study

Clinical study investigating the performance of the proposed skin imaging device and associated rt-DABAS algorithm was conducted at the Department of Dermatology, Venereology and Dermatooncology, at Semmelweis University (Budapest, Hungary). Lesions of outpatients (who volunteered to participate in the study) waiting for surgery were examined. Skin lesions to undergo surgical treatment and – in some cases – other benign skin lesions not to be removed were examined by both the proposed and the reference US imaging devices. The excised lesions were also further examined histopathologically. With an an ethical approval (OGYÉI/16798/2017) for a maximum number of 200 lesions, 184 lesions were examined as belonging to 144 patients.

5.3.4 Examination process of the clinical study

The position of the lesion and its location on the body were documented by close-up photographs (making sure that identity of the patient was as less recognizable as possible).

A dedicated radiologist with specialized experience in dermatological ultrasound examination examined the lesion using the reference USI device, and saved the relevant B-mode images.

DOI:10.15774/PPKE.ITK.2020.006

The lesion was also scanned by the proposed portable skin imaging device, making an attempt to scan in the same plane as that of the reference image scanning, for the sake of comparability. During the recordings, all incoming data frames were saved without using the rt-DABAS algorithm for position estimation. The algorithm was applied to the recorded data in the data processing phase (in order to keep the performance investigation under control). Typically, 2 to 6 images were taken per lesion.

In both ultrasound examinations, a commercially available ultrasound gel provided the appropriate acoustic coupling between the ultrasound device and the skin surface. Following the examination of each patient, gel was cleaned out from the removable cap and the transducer and cap were disinfected.

Following histopathological examination (of the excised lesions), image of the histological slice (photographed through an optical microscope) were acquired as well as the final (histopathological) diagnosis of the lesion.

5.3.5 Data processing

Data frames acquisitioned by the portable skin USI device were converted to 2-D images as follows. For each recording, relevant section of the data set that contained the image of the lesion and some surrounding skin was selected in a custom-written application. 2-D images were created from the selected sets of data by applying the rt-DABAS algorithm on data frames already aligned after the preprocessing step of applying automatic axial correction (see Section 4.2.6 and Fig. 4.16). For applying the rt-DABAS algorithm, calibration curve was determined for the transducer beam characteristics by calculating the average decorrelation curve over pairs of data frames with known distances, collected by scanning an agar phantom containing homogeneously distributed graphite grains (of 4% w/w concentration), as described in Section 4.5. In correspondence with the conclusions from simulations and phantom experiment results presented in Section 4.6.3, grid distance of 305 μm (corresponding to a correlation coefficient of 0.5 on the calibration curve) was used for rt-DABAS imaging.

The US images obtained were compared with those of the reference device, and

DOI:10.15774/PPKE.ITK.2020.006

also with the photograph of the histological slice and with the photograph of the lesion surface.

The images were compared regarding the morphology and the spatial dimensions of the lesions as seen on the images. The aim of this investigation was to test the diagnostic capability of the portable ultrasound device, including testing of the rt-DABAS imaging method applied. In this way, validation of the rt-DABAS algorithm on living tissue was part of the investigation – as presented and discussed in Section 4.6.4. On the other hand, regarding the content of the images (such as morphology and echogenicity of the lesions), the device (and algorithm) was investigated for the capability of providing the clinically relevant information of skin lesions as compared to the reference device capabilities.

5.4 Results

As already mentioned (Section 5.3.3), 184 skin lesions were examined (as described in Section 5.3.4). The lesions were distributed in the classes of melanoma (15%), basalioma (41%), spinalioma (19%), nevus (8%), and other lesions (keratosis solaris, keratoacanthoma, dermatofibroma, surgical scar).

Fig. 5.2 shows an example of corresponding image pairs of a basal cell carcinoma as well as a visualization of the (rt-DABAS) scan conversion algorithm output.

Distortion-compensation of images acquired via freehand manual scanning plays the crucial role in the acceptability of the proposed imaging device. Acceptable performance of the portable scanner and rt-DABAS algorithm was qualitatively observed when comparing the morphological appearance of lesions and other structures on the corresponding images. Quantification of this observation was also performed, based on measurements of (axial and lateral) spatial dimensions of the manually marked borders of the lesions – as described in Subsection *Evaluation of clinical data* of Section 4.5.3. As presented and discussed in Section 4.6.4, for lesions with (axial) thicknesses ranging from 0.7 to 5.5 mm and (lateral) widths from 3.1 to 14.6 mm, the discrepancies – in terms of mean absolute difference and of its standard deviation – of measured dimensions on the manually scanned image as compared

DOI:10.15774/PPKE.ITK.2020.006

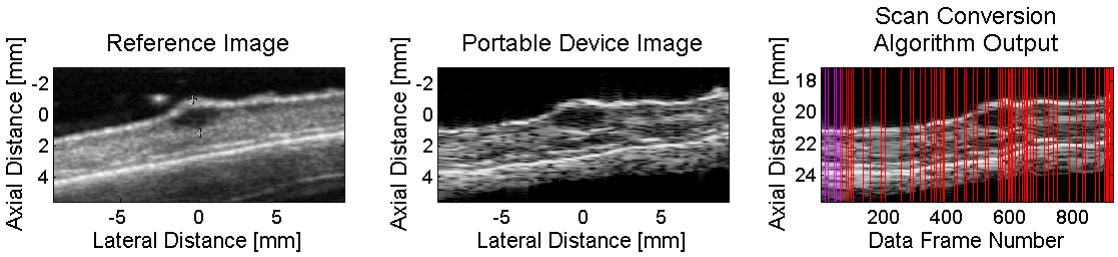

Figure 5.2: Comparison of ultrasound images of a basal cell carcinoma generated by a commercially available reference device (Hitachi Preirus with EUP-L75, left) and by the portable device designed for skin examination (middle). The image on the right visualizes performance of the scan conversion algorithm. Red lines represent data frames accepted to the image grid (with a grid distance of 305 μm corresponding to a correlation coefficient of 0.5). (Purple lines are frames also accepted by the algorithm but not shown on the image in the middle.)

to those measured on corresponding reference images were 10.8 ± 8.6% in width and 8.6 ± 6.7% in thickness (Table 4.3). As noted in Section 4.5.3, discrepancies of thickness values indicate the inaccuracy of the measurement itself. The two main reasons of the inaccuracy are as follows. On the one hand, despite the attempts for making the recording planes (of the portable and reference device images) as close to each other as possible, the planes could not be perfectly identical in practice. On the other hand, manual marking of lesion borders (in the two orthogonal dimensions) introduced some further inaccuracies into the measurements. Since the width error values did not significantly exceed the thickness error values that characterize the accuracy of the measurement, it was concluded that the quantitative results confirmed the qualitative observations, i.e. that the image distortions on the portable device images tend to be negligibly small, therefore, the cost-effective portable device may be used reliably for skin examination applications.

It was observed that the rt-DABAS method performed well even on some data obtained with significant variations of scanning velocity (this was not quantified but was qualitatively detectable – see Fig. 4.15 or Fig. 5.2).

The results suggested that the presented portable device is able to perform im-

DOI:10.15774/PPKE.ITK.2020.006

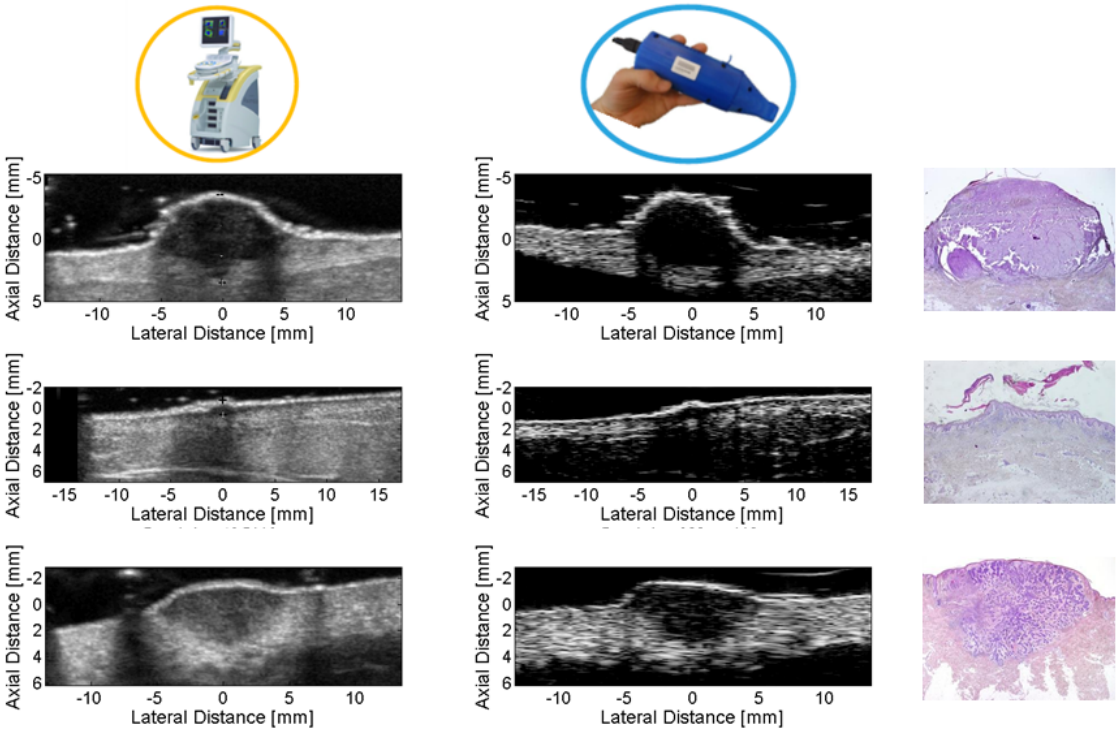

Figure 5.3: Comparison of corresponding ultrasound images obtained with a commercial reference device (Hitachi Preirus with EUP-L75) ***(left)*** *and those obtained with the proposed portable skin imaging device* ***(middle)*** *and of photographs taken of the slices used in histological examination* ***(right)*** *of certain lesions: melanoma* ***(top)****, keratosis seborrhoica* ***(middle)*** *and basalioma* ***(bottom)****.*

ages of human skin lesions presenting the same morphological information as that for the reference device. The two devices provided images with similar spatial resolution. Images of the portable device showed slightly stronger contrast, with the settings used. A result of this was a more pronounced appearance of thinner lesions on these images. On the other hand, however, some of the hue subtleties (referring to echogenicity) were less visible on the higher contrast images. A definite weakening of signals coming from the subcutaneous layer was also observed, but this did not appear to be disturbing for most of the lesions of interest being located within the epidermis and the dermis. The reasons behind the signal-weakening in deeper layers were the lack of TGC (time-gain compensation) on portable device images (while the reference device images did have TGC) and the strong focus of the ultrasound

DOI:10.15774/PPKE.ITK.2020.006

beam of the portable device. (For the reason of lesions of interest typically appearing above the subcutaneous layer of the skin, there was no need for overcoming this issue by using TGC or ultrasound beam with a wider focal range.)

In summary, it was shown that the proposed portable skin imaging device – utilizing the rt-DABAS method – was capable of providing clinically relevant information of the structures of human skin layers and of various skin lesions, with appropriate resolution B-mode ultrasound images. Examples of such images are shown in Fig. 5.3 of different types of lesions, together with both the corresponding reference ultrasound and histological images. It is important to note for the quantification of 'cost-effectiveness' that the USI system used here as a reference costed ∼50k USD as by 2017 while the portable USI device was built for a total cost of 5k USD, which could be significantly reduced by mass-manufacturing and by using a custom electrical circuit as the pulser-receiver-digitizer.

5.5 Conclusions

A portable, cost-effective ultrasound imaging device was designed and developed for skin examination, using a freehand scanning method with data-based scan reconstruction. The device appeared to provide valuable images of human skin and skin lesions in a clinical trial, suggesting the opportunity to enhance the accuracy and reliability of non-invasive skin cancer diagnostics and also to assist treatment planning for skin lesions as based on their depth extent and morphology. On the one hand, images of various types of skin lesions showed the capability of providing the clinically relevant information of shape, morphology and echogenicity which together may assist the differential diagnosis of skin lesions providing additional information to dermoscopy examination in a cost-effective and non-invasive way. On the other hand, the capability of showing intracutaneous location and thickness of the lesions could play a crucial role in the choice of their treatment and, where appropriate, in the design of the surgical procedure.

The proposed portable system lacks some of the diagnostically important modalities – such as velocimetry and elastography – of commercially available high-frequency

DOI:10.15774/PPKE.ITK.2020.006

ultrasound imaging systems used as reference, however, it was shown that it can provide B-mode images with the above-detailed information at a fraction of the cost of the latter, rather bulky and expensive devices.

Future work includes the development of easy-to-interpret presentation of images for non-radiologist users (dermatologists, general practitioners), elaboration of computer-aided classification algorithms for lesion type differentiation being fitted to the images and development of a more user-friendly, wireless device. With those improvements, the proposed system would become a truly valuable tool applying the real-time rt-DABAS method in real life.

DOI:10.15774/PPKE.ITK.2020.006

Chapter 6

Summary

6.1 New scientific results

Thesis I: *Use of a generalized two-port network model of ultrasound transducers is proposed for estimating the acoustic power output of transducers from electrical impedance measurements with the transducer placed in 3 different materials. As compared with reference acoustic measurements performed using a hydrophone system, the proposed method gave a consistent overestimation (within 34%) of acoustic power output for HIFU (high intensity focused ultrasound) transducers, showing that it can serve as a practical tool for ensuring transducer safety.*

Corresponding publication: [1].

The theory behind this thesis point uses a relatively simple equivalent circuit model of ultrasound transducers, by treating the 'backing' part of the 'transmission line' from the commonly accepted 'KLM model' as part of the 'black box' having two ports only (one for the electrical voltage and another for the 'front load' of the transducer, represented by an equivalent electrical voltage). By measuring the electrical impedance changes of the transducer when placed in 3 different propagation media, parameters of the two-port network model can be estimated, yielding an estimate of the acoustic power output (and accordingly, of the electrical power consumption of the transducer).

The method was tested for high-intensity focused ultrasound (HIFU) transducers (with 1.06, 3.19, 0.50, 1.70 MHz center frequencies) and compared with

DOI:10.15774/PPKE.ITK.2020.006

acoustic measurements performed by using a hydrophone system, as reference. The impedance-based method consistently overestimated the measured output, with errors of 17.0, 4.5, 21.8, 7.8% (for transducers with the above center frequencies, respectively).

Electrical impedance measurements of the transducer in 3 propagation media is a relatively simple and quick method requiring standard laboratory equipment only. Therefore, with the results of consistent overestimation, the proposed method can be used as a simple, quick and potentially wide-spread means of ensuring transducer acoustic output falling within specified safety limits.

Thesis II: *A method is proposed for quantitatively characterizing and visualizing the dynamic behavior of temporal changes in biological tissue by pixelwise decorrelation analysis of an ultrasound image sequence, regardless of the rate of the changes (applying a PRF greater than the rate of changes to be observed). The method was tested on post-mortem tissue effects, characterizing and mapping changes observed in time frames ranging from 100 to 5000 seconds at the level of small ($\sim 800\ \mu m^2$) spatial areas.*

Corresponding publication: [2].

The proposed method is based on simple calculations of time constants for the exponential part of decorrelation functions calculated for raw ultrasound signal amplitude changes at a given spatial location (i.e. image pixel). The method was successfully tested on investigating post-mortem tissue dynamics of mice (taking advantage of the lack of artifactual voluntary movements in these experiments and also making use of data from mice who did not survive experiments of a separate investigation). Quantitative results of dynamics characterization were in accordance with qualitative observations (on the ultrasound image sequences) both in short- and long-term, in the ranges of 100 and 5000 seconds, respectively.

Quantitative characterization and map-like visualization of dynamic changes can be useful in several application fields, including the monitoring of long-term biological phenomena such as response to therapy or slow blood perfusion in the capillaries or even in understanding the post-mortem redistribution of various drugs. Industrial

DOI:10.15774/PPKE.ITK.2020.006

applications such as the detection of signs of material fatigue (in materials being transparent to ultrasound) are also possible.

Thesis III: *A real-time spatial data-correlation-based freehand scan conversion algorithm has been developed, using a fixed calibration curve for which robustness and simplified estimation process have been proven and from which an optimal range of input parameter 'step size' can be derived for the algorithm in the case of a specific imaging system.*

Corresponding publications: [3] and [4].

Thesis III.a: *A real-time freehand scan conversion algorithm has been developed for 2-D scan conversion using a single-element ultrasound transducer, being based on spatial correlation of data recorded.*

Corresponding publications: [3] and [4].

Sensorless freehand scanning has several advantages in ultrasound imaging such as cost-effectiveness and reduced complexity of the system. To compensate for distortions of the freehand movement, a data-based scan conversion method was introduced and generalized (for 1-D to 2-D scan conversion), estimating spatial distances based on a measure of correlation. The real-time algorithm uses a predefined image grid with a uniform inter-line distance. The defined distance corresponds to a certain correlation coefficient due to the calibration curve. Each incoming data frame is accepted into the image grid if it has the expected correlation coefficient with the last accepted data frame, otherwise it is rejected.

The algorithm was tested for being able to generate an image from 1000 A-line frames in 345±132 ms (using MATLAB on a computer with Intel Core i5 processor, 8 GB RAM). For a dedicated architecture, with a 10-fold oversampling and a PRF $\geq$ 667 Hz, a scanning speed of $\geq$ 20 mm/s is estimated.

The method can be applied in sensorless freehand scanning, with special usage of applications in which cost-effectiveness, complexity, the need for eliminating mechanical motion elements or acoustic coupling is a major constraint while dimension incrementation (of images) is needed. Specific applications are in skin imaging and

DOI:10.15774/PPKE.ITK.2020.006

in high-frequency non-destructive testing. Moreover, the method can also be applied for annular array transducers (providing high-quality and smooth focus at the cost of dimension incrementation).

Thesis III.b: *I showed that the calibration curve (reflecting spatial decorrelation) for data-based scan conversion is primarily a function of transducer characteristics (being less dependent on the examined media). The calibration curve was found to be robust enough for different scatterer densities (*8.3×10^{-3} *mean absolute error) and signal-to-noise ratios (*1.0×10^{-3} *mean absolute error for -5 dB SNR) for simulations presented in this thesis. This result allows the use of the scan conversion algorithm on a wide variety of imaged media with a single transducer calibration.*

Corresponding publication: [3].

The data-based scanning method of *Thesis III.a* relies on the one-to-one correspondence of the distance between two parallel data frames and their "similarity" measured by the Pearson correlation coefficient (for distances within transducer beamwidth and ideally in homogeneous FDS (fully developed speckle) case, due to the literature). This distance-correlation correspondence is defined by the calibration curve (representing correlation as a function of distance).

As stated above, calibration curve was tested for different scatterer densities and signal-to-noise ratios and found to be robust enough, with mean absolute errors on the scale of 10^{-3} for both. Higher but still acceptable differences were found when comparing calibration curves obtained from simulated and experimental data: 1.19×10^{-2} mean absolute error. It was also presented that use of a fixed calibration curve compared to an adaptive calibration curve gave similar accuracies, with an average overlap of the accuracy ranges of 92.94% for simulations and 42.83% for experiments, for the data presented, while the proposed method using a fixed calibration curve had the great advantage of a 350-fold faster computation time.

Statement of this thesis confirms the robustness of the proposed method, eliminating the necessity for performing calibration on a wide variety of circumstances (at least of scatterer densities and noise levels).

DOI:10.15774/PPKE.ITK.2020.006

Thesis III.c: *I found that for estimating the calibration curve, a few (31 in 1 mm distances for ∼8 MHz transducer) scatterers placed along the axis of ultrasound pulse-echo propagation and covering the axial region of interest are sufficient. This result allows for calibration curve estimation calculations with the following advantages: a significant fastening of calibration curve calculation in simulations and a widening of possibilities for calibration curve calculations based on phantom measurements.*

Corresponding publication: [3].

A series of scatterers were placed with 1 mm distances (for ∼8 MHz transducer) covering the range of interest (for imaging) through an axial line. The mean absolute difference between the calibration curve (relating correlation and distance) obtained from this set of scatterers and the one obtained from FDS was found to be insignificant, being only 6.9×10^{-3} in the case of the simulations presented.

Application of this result can be a simplified process of calibration curve estimation for single-element transducers. Using such simplified phantoms significantly reduces calculation time in simulations (simulated ultrasound image calculation took ∼10 seconds for 31 scatterers while taking ∼7.5 hours for FDS phantom with 154 740 scatterers on a PC with Intel Core i5 processor, 8 GB RAM) and widens the field of feasible phantom manufacturing techniques for experimental calibration curve estimation (such that wire phantoms and 3-D printed phantoms become applicable).

Thesis III.d: *I showed that there exists a range for image grid step sizes, within which the proposed scan conversion algorithm has optimal performance, and that the optimal step size can be determined from the calibration curve.*

Corresponding publication: [3].

When analyzing the proposed scan conversion algorithm in terms of position estimation errors, it was found that a range of image grid step sizes (being an input of the algorithm) exists in which both the bias and ripple errors are minimal. This led to the recognition that, for a specific transducer and calibration curve, a range of image grid step sizes can be determined using which optimal performance of the scan conversion algorithm can be attained. The region is in correspondence with

DOI:10.15774/PPKE.ITK.2020.006

the slope of the calibration curve. The higher the slope (absolute derivative) is, the more likely optimal performance of position estimation will be achieved. In the cases of the experiments presented, bias and ripple errors were not exceeding 3.9% or 85.5 μm, respectively for a wide range of image step sizes: 150–350 μm. Worse performance was obtained with experimental data ($<$ 15.4% absolute bias and $<$ 1143.0 μm ripple, but still being optimal on the same range.

Direct application of this result is the deduction of image grid step sizes to be used for a scanning system with a certain calibration curve.

DOI:10.15774/PPKE.ITK.2020.006

Bibliography

[1] G. Csány, M. D. Gray, and M. Gyöngy, "Estimation of acoustic power output from electrical impedance measurements," in *Acoustics*, vol. 2, no. 1. Multidisciplinary Digital Publishing Institute, 2020, pp. 37–50.

[2] G. Csány, L. Balogh, and M. Gyöngy, "Investigation of post-mortem tissue effects using long-time decorrelation ultrasound," *Physics Procedia*, vol. 70, pp. 1195–1199, 2015.

[3] G. Csány, K. Szalai, and M. Gyöngy, "A real-time data-based scan conversion method for single element ultrasound transducers," *Ultrasonics*, vol. 93, pp. 26–36, 2019.

[4] M. Gyöngy and G. Csány, "Method for generating ultrasound image and computer readable medium," Patent, Dec. 29, 2016, WO Patent Application 2016/ 207 673.

[5] G. Csány, K. Szalai, K. Füzesi, and M. Gyöngy, "A low-cost portable ultrasound system for skin diagnosis," in *Proceedings of Meetings on Acoustics 6ICU*, vol. 32, no. 1. ASA, 2017, p. 020002.

[6] G. Harvey, A. Gachagan, and T. Mutasa, "Review of high-power ultrasound-industrial applications and measurement methods," *IEEE transactions on ultrasonics, ferroelectrics, and frequency control*, vol. 61, no. 3, pp. 481–495, 2014.

[7] C. R. Hill, J. C. Bamber, and G. R. ter Haar, "Physical principles of medical ultrasonics," 2004.

[8] V. J. Robertson and K. G. Baker, "A review of therapeutic ultrasound: effectiveness studies," *Physical therapy*, vol. 81, no. 7, pp. 1339–1350, 2001.

[9] T. L. Szabo, *Diagnostic ultrasound imaging: inside out.* Academic Press, 2004.

DOI:10.15774/PPKE.ITK.2020.006

[10] A. Taruttis and V. Ntziachristos, "Advances in real-time multispectral optoacoustic imaging and its applications," *Nature photonics*, vol. 9, no. 4, pp. 219–227, 2015.

[11] E. Demirors, G. Alba, G. E. Santagati, and T. Melodia, "High data rate ultrasonic communications for wireless intra-body networks," in *2016 IEEE International Symposium on Local and Metropolitan Area Networks (LANMAN)*. IEEE, 2016, pp. 1–6.

[12] X. Jiang, Y. Lu, H.-Y. Tang, J. M. Tsai, E. J. Ng, M. J. Daneman, B. E. Boser, and D. A. Horsley, "Monolithic ultrasound fingerprint sensor," *Microsystems & nanoengineering*, vol. 3, no. 1, pp. 1–8, 2017.

[13] B. Nelson and A. Sanghvi, "Out of hospital point of care ultrasound: current use models and future directions," *European Journal of Trauma and Emergency Surgery*, vol. 42, no. 2, pp. 139–150, 2016.

[14] Y. J. Choi, J. H. Baek, H. S. Park, W. H. Shim, T. Y. Kim, Y. K. Shong, and J. H. Lee, "A computer-aided diagnosis system using artificial intelligence for the diagnosis and characterization of thyroid nodules on ultrasound: initial clinical assessment," *Thyroid*, vol. 27, no. 4, pp. 546–552, 2017.

[15] K. K. Shung and G. A. Thieme, *Ultrasonic scattering in biological tissues*. CRC Press, 1992.

[16] P. N. Burns, "Introduction to the physical principles of ultrasound imaging and doppler," *Fundamentals in Medical Biophysics*, 2005.

[17] R. S. Cobbold, *Foundations of biomedical ultrasound*. Oxford University Press, 2006.

[18] O. Panametrics, "Ultrasonic transducers technical notes," Online: https://ctac.mbi.ufl.edu/files/2017/02/ultrasound-basics.pdf, 2006.

[19] A. Fenster, D. B. Downey, and H. N. Cardinal, "Three-dimensional ultrasound imaging," *Physics in Medicine & Biology*, vol. 46, no. 5, p. R67, 2001.

[20] R. Krimholtz, D. A. Leedom, and G. L. Matthaei, "New equivalent circuits for elementary piezoelectric transducers," *Electronics Letters*, vol. 6, no. 13, pp. 398–399, 1970.

DOI:10.15774/PPKE.ITK.2020.006

[21] S. Van Kervel and J. Thijssen, "A calculation scheme for the optimum design of ultrasonic transducers," *Ultrasonics*, vol. 21, no. 3, pp. 134–140, 1983.

[22] M. Castillo, P. Acevedo, and E. Moreno, "Klm model for lossy piezoelectric transducers," *Ultrasonics*, vol. 41, no. 8, pp. 671–679, 2003.

[23] N. Afsham, M. Najafi, P. Abolmaesumi, and R. Rohling, "Out-of-plane motion estimation based on a Rician-Inverse Gaussian model of RF ultrasound signals: speckle tracking without fully developed speckle," in *Medical Imaging 2012: Ultrasonic Imaging, Tomography, and Therapy*, vol. 8320. International Society for Optics and Photonics, 2012, p. 832017.

[24] P. Hassenpflug, R. W. Prager, G. M. Treece, and A. H. Gee, "Speckle classification for sensorless freehand 3-d ultrasound," *Ultrasound in Medicine & Biology*, vol. 31, no. 11, pp. 1499–1508, 2005.

[25] F. Dong, D. Zhang, Y. Yang, Y. Yang, and Q. Qin, "Distance estimation in ultrasound images using specific decorrelation curves," *Wuhan University Journal of Natural Sciences*, vol. 18, no. 6, pp. 517–522, 2013.

[26] A. H. Gee, R. J. Housden, P. Hassenpflug, G. M. Treece, and R. W. Prager, "Sensorless freehand 3D ultrasound in real tissue: speckle decorrelation without fully developed speckle," *Medical Image Analysis*, vol. 10, no. 2, pp. 137–149, 2006.

[27] C. Laporte and T. Arbel, "Measurement selection in untracked freehand 3D ultrasound," in *International Conference on Medical Image Computing and Computer-Assisted Intervention*. Springer, 2010, pp. 127–134.

[28] A. Shaw and K. Martin, "The acoustic output of diagnostic ultrasound scanners," *The safe use of ultrasound in medical diagnosis. 3rd ed. London: The British Institute of Radiology*, pp. 18–45, 2012.

[29] C. C. Coussios and R. A. Roy, "Applications of acoustics and cavitation to noninvasive therapy and drug delivery," *Annual Review of Fluid Mechanics*, vol. 40, pp. 395–420, 2008.

[30] S. Kárpáti, L. Kemény, and E. Remenyik, *Börgyógyászat és venerológia*, S. Kárpáti, Ed. Medicina Könyvkiadó, 2013.

DOI:10.15774/PPKE.ITK.2020.006

[31] G. P. Guy Jr, C. C. Thomas, T. Thompson, M. Watson, G. M. Massetti, and L. C. Richardson, "Vital signs: melanoma incidence and mortality trends and projections — United States, 1982–2030," *MMWR. Morbidity and Mortality Weekly Report*, vol. 64, no. 21, p. 591, 2015.

[32] A. Tompa, "A daganatos betegségek elöfordulása, a hazai és a nemzetközi helyzet ismertetése," *Magyar Tudomány*, 2011, http://www.matud.iif.hu/2011/11/06.htm.

[33] Cancer Council Australia, "Skin cancer," http://www.cancer.org.au/about-cancer/types-of-cancer/skin-cancer.html, Accessed: 2017 Dec.

[34] J. K. Robinson, "Sun exposure, sun protection, and vitamin D," *Journal of the American Medical Association*, vol. 294, no. 12, pp. 1541–1543, 2005.

[35] D. S. Rigel, J. Russak, and R. Friedman, "The evolution of melanoma diagnosis: 25 years beyond the ABCDs," *CA: A Cancer Journal for Clinicians*, vol. 60, no. 5, pp. 301–316, 2010.

[36] American Cancer Society, "Survival rates for melanoma skin cancer, by stage," https://www.cancer.org/cancer/melanoma-skin-cancer/detection-diagnosis-staging/survival-rates-for-melanoma-skin-cancer-by-stage.html, Accessed: 2017 Dec.

[37] K. Berman, "Basal cell skin cancer," MedlinePlus, https://medlineplus.gov/ency/article/000824.htm, 2015.

[38] American Cancer Society, "Key statistics for melanoma skin cancer," https://www.cancer.org/cancer/melanoma-skin-cancer/about/key-statistics.html, Accessed: 2017 Dec.

[39] P. Röhlich, *Szövettan II.* Semmelweis Orvostudományi Egyetem (Budapest), 1999.

[40] S. Parker, *The Human Body.* DK Children, 1999.

[41] E. B. Hawryluk and D. E. Fisher, "Melanoma epidemiology, risk factors, and clinical phenotypes," in *Advances in Malignant Melanoma-Clinical and Research Perspectives.* InTech, 2011.

[42] A. I. Baba and C. Câtoi, *Comparative oncology.* Publishing House of the Romanian Academy Bucharest, 2007.

DOI:10.15774/PPKE.ITK.2020.006

[43] J. Beer, L. Xu, P. Tschandl, and H. Kittler, "Growth rate of melanoma in vivo and correlation with dermatoscopic and dermatopathologic findings," *Dermatology Practical & Conceptual*, vol. 1, no. 1, p. 59, 2011.

[44] R. J. Friedman, D. S. Rigel, and A. W. Kopf, "Early detection of malignant melanoma: the role of physician examination and self-examination of the skin," *CA: A Cancer Journal for Clinicians*, vol. 35, no. 3, pp. 130–151, 1985.

[45] R. Bränström, M.-A. Hedblad, I. Krakau, and H. Ullén, "Laypersons' perceptual discrimination of pigmented skin lesions," *Journal of the American Academy of Dermatology*, vol. 46, no. 5, pp. 667–673, 2002.

[46] L. Thomas, P. Tranchand, F. Berard, T. Secchi, C. Colin, and G. Moulin, "Semiological value of ABCDE criteria in the diagnosis of cutaneous pigmented tumors," *Dermatology*, vol. 197, no. 1, pp. 11–17, 1998.

[47] R. L. Barnhill, G. C. Roush, M. S. Ernstoff, and J. M. Kirkwood, "Interclinician agreement on the recognition of selected gross morphologic features of pigmented lesions: studies of melanocytic nevi V." *Journal of the American Academy of Dermatology*, vol. 26, no. 2, pp. 185–190, 1992.

[48] N. R. Abbasi, H. M. Shaw, D. S. Rigel, R. J. Friedman, W. H. McCarthy, I. Osman, A. W. Kopf, and D. Polsky, "Early diagnosis of cutaneous melanoma: revisiting the ABCD criteria," *Journal of the American Medical Association*, vol. 292, no. 22, pp. 2771–2776, 2004.

[49] R. M. MacKie, "Clinical recognition of early invasive malignant melanoma." *BMJ: British Medical Journal*, vol. 301, no. 6759, p. 1005, 1990.

[50] J. E. Gershenwald, W. Thompson, P. F. Mansfield, J. E. Lee, M. I. Colome, C.-h. Tseng, J. J. Lee, C. M. Balch, D. S. Reintgen, and M. I. Ross, "Multi-institutional melanoma lymphatic mapping experience: the prognostic value of sentinel lymph node status in 612 stage I or II melanoma patients," *Journal of Clinical Oncology*, vol. 17, no. 3, pp. 976–976, 1999.

[51] W. Abramovits and L. C. Stevenson, "Changing paradigms in dermatology: new ways to examine the skin using noninvasive imaging methods," *Clinics in Dermatology*, vol. 21, no. 5, pp. 353–358, 2003.

DOI:10.15774/PPKE.ITK.2020.006

[52] A. A. Marghoob, L. D. Swindle, C. Z. Moricz, F. A. S. Negron, B. Slue, A. C. Halpern, and A. W. Kopf, "Instruments and new technologies for the in vivo diagnosis of melanoma," *Journal of the American Academy of Dermatology*, vol. 49, no. 5, pp. 777–797, 2003.

[53] Y. Pan, D. S. Gareau, A. Scope, M. Rajadhyaksha, N. A. Mullani, and A. A. Marghoob, "Polarized and nonpolarized dermoscopy: the explanation for the observed differences," *Archives of Dermatology*, vol. 144, no. 6, pp. 828–829, 2008.

[54] C. Wassef and B. K. Rao, "Uses of non-invasive imaging in the diagnosis of skin cancer: an overview of the currently available modalities," *International Journal of Dermatology*, vol. 52, no. 12, pp. 1481–1489, 2013.

[55] J. March, M. Hand, A. Truong, and D. Grossman, "Practical application of new technologies for melanoma diagnosis: Part II. Molecular approaches," *Journal of the American Academy of Dermatology*, vol. 72, no. 6, pp. 943–958, 2015.

[56] M. Vestergaard, P. Macaskill, P. Holt, and S. Menzies, "Dermoscopy compared with naked eye examination for the diagnosis of primary melanoma: a meta-analysis of studies performed in a clinical setting," *British Journal of Dermatology*, vol. 159, no. 3, pp. 669–676, 2008.

[57] D. Piccolo, A. Ferrari, K. Peris, R. Daidone, B. Ruggeri, and S. Chimenti, "Dermoscopic diagnosis by a trained clinician vs. a clinician with minimal dermoscopy training vs. computer-aided diagnosis of 341 pigmented skin lesions: a comparative study," *British Journal of Dermatology*, vol. 147, no. 3, pp. 481–486, 2002.

[58] M. J. Koehler, S. Lange-Asschenfeldt, and M. Kaatz, "Non-invasive imaging techniques in the diagnosis of skin diseases," *Expert Opinion on Medical Diagnostics*, vol. 5, no. 5, pp. 425–440, 2011.

[59] M. J. Budak, J. R. Weir-McCall, P. M. Yeap, R. D. White, S. A. Waugh, T. A. Sudarshan, and I. A. Zealley, "High-resolution microscopy-coil MR imaging of skin tumors: techniques and novel clinical applications," *RadioGraphics*, vol. 35, no. 4, pp. 1077–1090, 2015.

[60] J. Hatvani, "Use of annular arrays in ultrasound imaging," Master's thesis, Pázmány Péter Catholic University, Faculty of Information Technology and Bionics, 2016.

DOI:10.15774/PPKE.ITK.2020.006

[61] X. Wortsman and J. Wortsman, "Clinical usefulness of variable-frequency ultrasound in localized lesions of the skin," *Journal of the American Academy of Dermatology*, vol. 62, no. 2, pp. 247–256, 2010.

[62] H. Uhara, K. Hayashi, H. Koga, and T. Saida, "Multiple hypersonographic spots in basal cell carcinoma," *Dermatologic Surgery*, vol. 33, no. 10, pp. 1215–1219, 2007.

[63] C. Harland, S. Kale, P. Jackson, P. Mortimer, and J. Bamber, "Differentiation of common benign pigmented skin lesions from melanoma by high-resolution ultrasound," *British Journal of Dermatology*, vol. 143, no. 2, pp. 281–289, 2000.

[64] N. Lassau, S. Mercier, S. Koscielny, M. Avril, A. Margulis, G. Mamelle, P. Duvillard, and J. Leclere, "Prognostic value of high-frequency sonography and color Doppler sonography for the preoperative assessment of melanomas." *AJR. American Journal of Roentgenology*, vol. 172, no. 2, pp. 457–461, 1999.

[65] A. Srivastava, L. Hughes, J. Woodcock, and P. Laidler, "Vascularity in cutaneous melanoma detected by Doppler sonography and histology: correlation with tumour behaviour," *British Journal of Cancer*, vol. 59, no. 1, p. 89, 1989.

[66] L. Chami, N. Lassau, M. Chebil, and C. Robert, "Imaging of melanoma: usefulness of ultrasonography before and after contrast injection for diagnosis and early evaluation of treatment," *Clinical, Cosmetic and Investigational Dermatology*, vol. 4, p. 1, 2011.

[67] D. Ogata, T. Uematsu, S. Yoshikawa, and Y. Kiyohara, "Accuracy of real-time ultrasound elastography in the differential diagnosis of lymph nodes in cutaneous malignant melanoma (CMM): a pilot study," *International Journal of Clinical Oncology*, vol. 19, no. 4, pp. 716–721, 2014.

[68] J. Civale, I. Rivens, A. Shaw, and G. ter Haar, "Focused ultrasound transducer spatial peak intensity estimation: a comparison of methods," *Physics in Medicine & Biology*, vol. 63, no. 5, p. 055015, 2018.

[69] R. C. Preston, *Output measurements for medical ultrasound*. Springer Science & Business Media, 2012.

[70] T. F. Johansen and T. Rommetveit, "Characterization of ultrasound transducers," in *Proc. of the 33rd Scandinavian Symposium on Physical Acoustics*, 2010.

DOI:10.15774/PPKE.ITK.2020.006

[71] J. L. San Emeterio and A. Ramos, "Models for piezoelectric transducers used in broadband ultrasonic applications," in *Piezoelectric Transducers and Applications*. Springer, 2009, pp. 97–116.

[72] V. G. M. Annamdas and C. K. Soh, "Application of electromechanical impedance technique for engineering structures: review and future issues," *Journal of Intelligent Material Systems and Structures*, vol. 21, no. 1, pp. 41–59, 2010.

[73] V. T. Rathod, "A review of electric impedance matching techniques for piezoelectric sensors, actuators and transducers," *Electronics*, vol. 8, no. 2, p. 169, 2019.

[74] E. B. Ndiaye, H. Duflo, P. Maréchal, and P. Pareige, "Thermal aging characterization of composite plates and honeycomb sandwiches by electromechanical measurement," *The Journal of the Acoustical Society of America*, vol. 142, no. 6, pp. 3691–3702, 2017.

[75] W. H. Hayt, J. E. Kemmerly, and S. M. Durbin, *Engineering circuit analysis*. McGraw-Hill New York, 2002.

[76] A. S. Sedra and K. C. Smith, *Microelectronic circuits*. New York: Oxford University Press, 1998.

[77] W. Y. Yang and S. C. Lee, *Circuit Systems with MATLAB and PSpice*. John Wiley & Sons, 2008.

[78] A. R. Selfridge, "Approximate material properties in isotropic materials," *IEEE Transactions on Sonics and Ultrasonics*, vol. 32, no. 3, pp. 381–394, 1985.

[79] W. Marczak, "Water as a standard in the measurements of speed of sound in liquids," *the Journal of the Acoustical Society of America*, vol. 102, no. 5, pp. 2776–2779, 1997.

[80] C. K. Abbey, M. Kim, and M. F. Insana, "Perfusion signal processing for optimal detection performance," in *Ultrasonics Symposium (IUS), 2014 IEEE International*. IEEE, 2014, pp. 2253–2256.

[81] T. R. Fosnight, F. M. Hooi, R. D. Keil, S. Subramanian, P. G. Barthe, Y. Wang, X. Ren, S. Ahmad, M. B. Rao, and T. D. Mast, "Motion-corrected echo decorrelation imaging of in vivo focused and bulk ultrasound ablation in a rabbit liver cancer

DOI:10.15774/PPKE.ITK.2020.006

model," in *2014 IEEE International Ultrasonics Symposium (IUS)*. IEEE, 2014, pp. 2161–2164.

[82] S. Subramanian, S. M. Rudich, A. Alqadah, C. P. Karunakaran, M. B. Rao, and T. D. Mast, "In vivo thermal ablation monitoring using ultrasound echo decorrelation imaging," *Ultrasound in Medicine & Biology*, vol. 40, no. 1, pp. 102–114, 2014.

[83] A.-L. Pélissier-Alicot, J.-M. Gaulier, P. Champsaur, and P. Marquet, "Mechanisms underlying postmortem redistribution of drugs: a review," *Journal of Analytical Toxicology*, vol. 27, no. 8, pp. 533–544, 2003.

[84] J. E. Hall and A. C. Guyton, *Guyton and Hall textbook of medical physiology*. Elsevier Health Sciences, 2011.

[85] T. R. Fosnight, F. M. Hooi, R. D. Keil, A. P. Ross, S. Subramanian, T. G. Akinyi, J. K. Killin, P. G. Barthe, S. M. Rudich, S. A. Ahmad *et al.*, "Echo decorrelation imaging of rabbit liver and vx2 tumor during in vivo ultrasound ablation," *Ultrasound in medicine & biology*, vol. 43, no. 1, pp. 176–186, 2017.

[86] C. L. Moore and J. A. Copel, "Point-of-care ultrasonography," *New England Journal of Medicine*, vol. 364, no. 8, pp. 749–757, 2011.

[87] N. J. Soni, R. Arntfield, and P. Kory, *Point of Care Ultrasound E-book*. Elsevier Health Sciences, 2014.

[88] J. Chaniot, B. Sciolla, P. Delachartre, T. Dambry, and B. Guibert, "Vessel segmentation in high-frequency 2D/3D ultrasound images," in *2016 IEEE International Ultrasonics Symposium (IUS)*. IEEE, 2016, pp. 1–4.

[89] M. R. Sobhani, H. Ozum, G. Yaralioglu, A. Ergun, and A. Bozkurt, "Portable low cost ultrasound imaging system," in *2016 IEEE International Ultrasonics Symposium (IUS)*. IEEE, 2016, pp. 1–4.

[90] C. Liu, F. T. Djuth, Q. Zhou, and K. K. Shung, "Micromachining techniques in developing high-frequency piezoelectric composite ultrasonic array transducers," *IEEE Transactions on Ultrasonics, Ferroelectrics, and Frequency Control*, vol. 60, no. 12, pp. 2615–2625, 2013.

DOI:10.15774/PPKE.ITK.2020.006

[91] K. A. Snook, C.-H. Hu, T. R. Shrout, and K. K. Shung, "High-frequency ultrasound annular-array imaging. Part I: Array design and fabrication," *IEEE Transactions on Ultrasonics, Ferroelectrics, and Frequency Control*, vol. 53, no. 2, pp. 300–308, 2006.

[92] A. J. Medlin and A. J. P. Niemiec, "Scan line display apparatus and method," Apr. 28 2011, US Patent App. 12/674,007.

[93] K. E. Thiele and S. H.-H. Chang, "Transducer with spatial sensor," Patent, Feb. 11, 2003, US Patent 6,517,491.

[94] A. Dunbar and E. Sobrino, "System for ultrasound image guided procedure," Patent, Sep. 11, 2014, US Patent App. 13/785,951.

[95] J. W. Sliwa Jr and S. T. Baba, "Method and apparatus for two dimensional ultrasonic imaging," Patent, Nov. 25, 1997, US Patent 5,690,113.

[96] Z. Banjanin and C. J. Sanders, "Patient-probe-operator tracking method and apparatus for ultrasound imaging systems," Patent, Oct. 25, 2016, US Patent 9,474,505.

[97] P. E. Eggers, S. P. Huntley, E. A. Eggers, and B. A. Robinson, "Method, apparatus and system for complete examination of tissue with hand-held imaging devices," US Patent 13/854,800, Aug. 29, 2013, US patent App. 13/854,800.

[98] G. Costa, A. J. Medlin, and A. J. P. Niemiec, "Improved scan display," Patent, Dec. 17, 2009, WO Patent 2009/ 149 499.

[99] S. G. Bartlett and P. J. Hirschausen, "Apparatus and method for medical scanning," Patent, Dec. 2, 2010, US Patent App. 12/675,473.

[100] A. J. Medlin, J. Brydon, and M. McCarthy, "Medical scanning apparatus and method," Patent, Oct. 14, 2010, US Patent App. 12/740,127.

[101] M.-H. Bae, "Hand-held ultrasonic probe," Patent, Jul. 7, 1999, EP Patent 0 927 539.

[102] M. A. Bahramabadi, "Sensorless out-of-plane displacement estimation for freehand 3D ultrasound applications," Master's thesis, Carleton University Ottawa, 2014.

DOI:10.15774/PPKE.ITK.2020.006

[103] D. Jasaitiene, S. Valiukeviciene, G. Linkeviciute, R. Raisutis, E. Jasiuniene, and R. Kazys, "Principles of high-frequency ultrasonography for investigation of skin pathology," *Journal of the European Academy of Dermatology and Venereology*, vol. 25, no. 4, pp. 375–382, 2011.

[104] N. Afsham, M. Najafi, P. Abolmaesumi, and R. Rohling, "A generalized correlation-based model for out-of-plane motion estimation in freehand ultrasound," *IEEE Transactions on Medical Imaging*, vol. 33, no. 1, pp. 186–199, 2014.

[105] J. Conrath and C. Laporte, "Towards improving the accuracy of sensorless freehand 3D ultrasound by learning," in *International Workshop on Machine Learning in Medical Imaging*. Springer, 2012, pp. 78–85.

[106] M. Li, "System and method for 3-D medical imaging using 2-D scan data," Patent, Dec. 10, 1996, US Patent 5,582,173.

[107] N. C. Kim, H. J. So, S. H. Kim, and J. H. Lee, "Three-dimensional ultrasound imaging method and apparatus using lateral distance correlation function," Patent, Jan. 24, 2006, US Patent 6,988,991.

[108] L. Y. Mo, W. T. Hatfield, and S. C. Miller, "Method and apparatus for tracking scan plane motion in free-hand three-dimensional ultrasound scanning using adaptive speckle correlation," Patent, Jan. 11, 2000, US Patent 6,012,458.

[109] C. Laporte, *Statistical methods for out-of-plane ultrasound transducer motion estimation*. McGill University, 2009.

[110] J. M. Thijssen, "Ultrasonic speckle formation, analysis and processing applied to tissue characterization," *Pattern Recognition Letters*, vol. 24, no. 4-5, pp. 659–675, 2003.

[111] J. A. Jensen, "Field: A program for simulating ultrasound systems," in *10th Nordicbaltic Conference on Biomedical Imaging, vol. 4, supplement 1, part 1: 351–353*. Citeseer, 1996.

[112] J. A. Jensen and N. B. Svendsen, "Calculation of pressure fields from arbitrarily shaped, apodized, and excited ultrasound transducers," *IEEE Transactions on Ultrasonics, Ferroelectrics, and Frequency Control*, vol. 39, no. 2, pp. 262–267, 1992.

DOI:10.15774/PPKE.ITK.2020.006

[113] J. P. Kemmerer, M. L. Oelze, and M. Gyöngy, "Scattering by single physically large and weak scatterers in the beam of a single-element transducer," *The Journal of the Acoustical Society of America*, vol. 137, no. 3, pp. 1153–1163, 2015.

[114] M. F. Insana, R. F. Wagner, D. G. Brown, and T. J. Hall, "Describing small-scale structure in random media using pulse-echo ultrasound," *The Journal of the Acoustical Society of America*, vol. 87, no. 1, pp. 179–192, 1990.

[115] R. F. Wagner, "Statistics of speckle in ultrasound B-scans," *IEEE Transactions on Sonics and Ultrasonics*, vol. 30, no. 3, pp. 156–163, 1983.

[116] R. Mallart and M. Fink, "The van Cittert–Zernike theorem in pulse echo measurements," *The Journal of the Acoustical Society of America*, vol. 90, no. 5, pp. 2718–2727, 1991.

[117] P. Hassenpflug, R. Prager, G. Treece, and A. Gee, "Distance measurement for sensorless 3D US," in *International Conference on Medical Image Computing and Computer-Assisted Intervention*. Springer, 2004, pp. 1087–1088.

[118] W. Smith and A. Fenster, "Statistical analysis of decorrelation-based transducer tracking for three-dimensional ultrasound," *Medical Physics*, vol. 30, no. 7, pp. 1580–1591, 2003.

[119] H. Rivaz, H. J. Kang, P. J. Stolka, R. Zellars, F. Wacker, G. Hager, and E. Boctor, "Novel reconstruction and feature exploitation techniques for sensorless freehand 3D ultrasound," in *Medical Imaging 2010: Ultrasonic Imaging, Tomography, and Therapy*, vol. 7629. International Society for Optics and Photonics, 2010, p. 76291D.

[120] K. Füzesi, "Tissue characterization and custom manufactured phantoms for modelling of medical ultrasound images," Ph.D. dissertation, Pázmany Peter Catholic University, Roska Tamás Doctoral School of Sciences and Technology, 2019.

[121] J. M. Thomas, J. Newton-Bishop, R. A'Hern, G. Coombes, M. Timmons, J. Evans, M. Cook, J. Theaker, M. Fallowfield, T. O'Neill *et al.*, "Excision margins in high-risk malignant melanoma," *New England Journal of Medicine*, vol. 350, no. 8, pp. 757–766, 2004.

[122] E. Christensen, P. Mjønes, O. A. Foss, O. M. Rørdam, and E. Skogvoll, "Pre-treatment evaluation of basal cell carcinoma for photodynamic therapy: comparative

DOI:10.15774/PPKE.ITK.2020.006

measurement of tumour thickness in punch biopsy and excision specimens," *Acta Dermato-Venereologica*, vol. 91, no. 6, pp. 651–655, 2011.

[123] V. Lees and J. Briggs, "Effect of initial biopsy procedure on prognosis in stage 1 invasive cutaneous malignant melanoma: review of 1086 patients," *British Journal of Surgery*, vol. 78, no. 9, pp. 1108–1110, 1991.

[124] P. Holt, "Cryotherapy for skin cancer: results over a 5-year period using liquid nitrogen spray cryosurgery," *British Journal of Dermatology*, vol. 119, no. 2, pp. 231–240, 1988.

[125] J. A. Langtry and A. Carruthers, "True electrocautery in the treatment of syringomas and other benign cutaneous lesions," *Journal of Cutaneous Medicine and Surgery*, vol. 2, no. 1, pp. 60–63, 1997.

[126] M. Gyöngy, L. Balogh, K. Szalai, and I. Kalló, "Histology-based simulations of ultrasound imaging: Methodology," *Ultrasound in Medicine & Biology*, vol. 39, no. 10, pp. 1925–1929, 2013.

[127] D. Csabai, K. Szalai, and M. Gyöngy, "Automated classification of common skin lesions using bioinspired features," in *2016 IEEE International Ultrasonics Symposium (IUS)*. IEEE, 2016, pp. 1–4.

[128] U.S. Department of Health and Human Services, Food and Drug Administration (FDA), Center for Devices and Radiological Health, "Marketing clearance of diagnostic ultrasound systems and transducers," Jun. 2019, https://www.fda.gov/media/71100/download.

DOI:10.15774/PPKE.ITK.2020.006

Acknowledgements

Despite having an extraordinary interest in dolphins and playing music seriously and enthusiastically since a very young age, I never thought of the field of ultrasound before as a potential field of my research and studies. Never before I met Dr. Miklós Gyöngy. Starting from an 'innocent' conversation about PhD experiences, we ended up talking about the research topics he was currently working on, in the field of ultrasonics and about his definite, gripping and attractive research plans for the near future. It was so convincing and I never regretted choosing him as my supervisor and mentor. I truly have learnt so many things from him during the years of my PhD studies. Consistency, predictability, effective and realistic planning of work were facilitating our work together and are skills that I tried to learn from him and that I am very grateful for, in addition to his assertive communication, understanding and natural humility. I have also gained knowledge and skills in thinking as an engineer, in researching attitude, in industrial utilization of results and in the ins and outs of scientific publication, at his side. I am so grateful to him for his leading by example and for all of his guidance making this work possible.

I thank my collaborators, with special thanks to Dr. Klára Szalai, chief radiologist at the Department of Dermatology, Venereology and Dermatooncology of Semmelweis University (Budapest, Hungary). She played an essential role in our professional relationship with the (dermatology) clinic. I have gained knowledge in ultrasonic skin cancer examination as well as experience in clinical study conductance and in the everyday life of a dermatooncology clinic. I am grateful for her ideas, collaboration, helpfulness, patience and her time spent during the months of the clinical study. I thank Dr. Enikö Kuroli for her kind helpfulness in collecting output data of the histopathological examinations and thank Rita Mátrahegyi for a similar help in collecting the professional macroscopic photographs of the skin lesions examined in the clinical study. I also thank Prof. Dr. Tamás Roska (founder of the

DOI:10.15774/PPKE.ITK.2020.006

Faculty of Information Technology and Bionics, Pázmány Péter Catholic University, Budapest, Hungary) and Prof. Dr. Sarolta Kárpáti (former director of the Department of Dermatology, Venereology and Dermatooncology of Semmelweis University) for initiating the collaboration of the two institutes. I thank Prof. Dr. Miklós Sárdy (present director of the aforementioned clinical department) for his cooperation and aid that made the clinical study possible.

I thank my collaborator, Dr. Michael Gray, an excellent engineer from the BUBBL lab of the Institute of Biomedical Engineering, Department of Engineering, University of Oxford (Oxford, UK). His collaboration during the research presented in Chapter 2 was truly exemplary. I am grateful for his availability, helpfulness, exactitude and straight communication. I have also learnt a lot from him.

I thank the generosity of Dr. Lajos Balogh for providing experimental animals from his veterinary clinic in the research presented in Chapter 3 and the generosity of Prof. Dr. Constantin-C. Coussios (my 'grand-supervisor') for use of the laboratory equipment of BUBBL lab.

Here I thank several further collaborators. Regarding the work presented in Chapter 2, I thank Dr. Jeffrey Ketterling and Dan Gross (from Lizzi Center for Biomedical Engineering, New York, NY, USA) for their help with measurements and theory, I thank my former labmate Balázs Bajnok for his preliminary work related to this research topic and Prof. Dr. Árpád I. Csurgay for exciting and encouraging discussions on relevant electrical theory. Regarding the work presented in Chapters 4–5, I thank my former labmate Máté Kiss for his helping developing the axial shift correction method applied in the preprocessing of clinical data, and also thank Dr. Krisztián Füzesi, my labmate and fellow PhD student, for designing and producing the casing of the setup used for the clinical data acquisition.

I am grateful to all of my teachers who guided me through my studies in high school (Budai Ciszterci Szent Imre Gimnázium, Budapest, Hungary) and at the university (PPKE-ITK – Faculty of Information Technology and Bionics, Pázmány Péter Catholic University, Budapest, Hungary), with special thanks to Prof. Dr. Árpád I. Csurgay and Prof. Dr. Tamás Roska. I am grateful to the directorate and administrative assistants of the Roska Tamás Doctoral School of Sciences and

DOI:10.15774/PPKE.ITK.2020.006

Technology for all of their helpfulness and support needed for this research and for enabling presentation of my results in prestigious international congresses. I thank in particular Prof. Dr. Péter Szolgay, Dr. Kristóf Iván, Tivadarné Vida and Lívia Adorján.

I thank Dr. Miklós Gyöngy again, for creating the environment and atmosphere of the SOUND (Superresolution in Optical, Ultrasound and Nanomagnetic Diagnosis) Laboratory at PPKE-ITK and I thank my longer term labmates, Janka Hatvani, Dr. Krisztián Füzesi, Ákos Makra, Péter Marosán, Domonkos Csabai and Ádám Simon for working together and for their impulses and helpfulness through the years.

I thank my fellow PhD students, with special thanks to Domokos Meszéna, Bertalan Kovács, Sándor Földi and Márton Hartdégen, my best friends, for sharing this journey and for the many memorable discussions, inspiration and encouragement.

I am extremely grateful to my family, with special thanks to my lovely wife, Mária Csány and parents, László Miklós Csány and Dr. Ragyiánó Rita Csányné and also to my sister and brothers. First of all, I am grateful to my Creator for hiding things to be discovered through science and for giving us the *spirit* to go after them, to discover them and to create new devices by invention.

The presented research formed part of the research programs supported by Pázmány Péter Catholic University (PPKE) under grants KAP14–17. The work was also supported by several grants and scholarships, namely the János Bolyai scholarship of the Hungarian Academy of Sciences; the grant PD 121105 of the Hungarian National Research, Development and Innovation Office (NKFIH); the Hungarian state funding EFOP-3.6.2-16-2017-00013, 3.6.3-VEKOP-16-2017-00002; and the GINOP-2.1.7-15-2016-02201.

I thank the National Institute of Pharmacy and Nutrition (OGYÉI, Budapest, Hungary) for authorizing the clinical study presented in Chapters 4–5 with the ethical grant OGYÉI/16798/2017. I thank the Elsevier's journal Ultrasonics for the 'R. W. B. Stephens Prize' I was awarded for my presentation at the 2017 International Congress on Ultrasonics (ICU2017); the Hungarian Dermatological Society (MDT, Budapest, Hungary) for 'The Best Poster' award of the 90th Congress of MDT (2017); PPKE for the 'PhD Excellence Scholarship' (2015).